

Ultrafast spectroscopy of nanomaterials

Zou, Xingquan

2012

Zou, X. (2012). Ultrafast spectroscopy of nanomaterials. Doctoral thesis, Nanyang Technological University, Singapore.

<https://hdl.handle.net/10356/50943>

<https://doi.org/10.32657/10356/50943>



Ultrafast Spectroscopy of Nanomaterials

Xingquan ZOU

Division of Physics and Applied Physics
School of Physical and Mathematical Sciences

A Dissertation Submitted to Nanyang Technological
University in Fulfillment of the Requirement for the
Degree of Doctor of Philosophy

Jun 2012

Acknowledgements

This research project would not have been possible without the guidance of my supervisor, help from our group members and support from my family.

First and foremost, I would like to express my utmost gratitude to my supervisor, Assistant Professor Chia Ee Min Elbert, for his excellent guidance, encouragement, caring and trust all these years. His broad knowledge and enthusiasm of physics has had a very rewarding and lasting effect on me. I have learned not only the extensive specialized knowledge but also the excellent research ethic and attitude which will remain with me throughout my career.

Next I would thank all the past and present members of our group — Dongwook, Saritha, Hemi, Chan, Chisin, Huanxin, Chengliang and Sabrina, for their unselfish help and useful discussions with them about the experiments and data analysis.

I would also like to thank my parents and relatives for teaching me the value of hard working, supporting me and encouraging me with their best wishes.

Finally, I would like to thank my wife, Huangchen. She was always there encouraging me and cheering me up over these years. This dissertation is dedicated to my two-year old son, Zou Bowen, the new love of my life.

Abstract

Ultrafast spectroscopy is a very useful technique to study the electronic and vibrational properties of many solid-state systems. In this dissertation, ultrafast optical-pump optical-probe (OPOP) and terahertz time-domain spectroscopy (THz-TDS) have been used to study low dimensional nanomaterials and bulk oxides which are often used substrates for nanomaterials, thin films and functional materials.

The photoexcited electrons in bilayer graphene (BLG) exhibit two relaxation processes — the fast relaxation time is less than 200 fs while the slow one is around a few ps. After the BLG has been intercalated with FeCl_3 , the sample became hole-doped. Also, there are many horizontal bands in the electronic band structure. The presence of these additional bands has caused three effects in the pump-probe results: (a) pump probe signal changes sign; (b) the signal rise time is much longer than that of BLG; (c) the fast relaxation process disappears leaving only the slow one.

The conductivity spectrum of Bernal BLG depends on the impurity concentration, chemical potential, temperature and bias voltage, but is nonetheless almost Drude-like at the lowest frequencies. In twisted BLG, van-Hove singularities develop near the Fermi energy, which results in an enhanced density of states (DOS). Strongly coupled stacking order BLG is investigated by THz-TDS at different temperatures. In the frequency dependence of the real conductivity, superposed on top of a Drude-like response, we observed a strong and narrow peak centered at ~ 2.7 THz. The overall Drude shape was analyzed using a disorder dependent model, while the conductivity peak at 2.7 THz was attributed to an enhanced DOS at that energy, which is caused by the presence of

low-energy van-Hove singularities arising from a commensurate twisting of the top graphene layer relative to the bottom layer.

The accurate substrate complex refractive index is a precondition for the THz study for the materials grown on the substrate. Z-cut quartz (CrysTec GmbH) is a very good transparent substrate for THz radiation, as it has a temperature-independent and almost frequency-independent refractive index $n = 2.10 + 0.002i$. The refractive index $n(\omega)$ of LaAlO_3 (LAO, CrysTec GmbH) is temperature-dependent and increases monotonically with frequency. The values of $k(\omega)$ are very small, and no obvious absorption peaks appeared frequency range 0.2—3 THz. After the LAO has been annealed, $n(\omega)$ shows sudden changes at certain frequencies where the absorption peaks appear in $k(\omega)$. Also, the crystal orientation can affect the complex refractive index.

SnO_2 nanowires are investigated by THz-TDS as a function of temperature. Results show that SnO_2 nanowires are not only transparent in the visible range, but also in the terahertz range 0.5 THz to 2.4 THz. The carrier density increases and scattering time decreases with increasing temperature. The reduction in carrier mobility compared with bulk material indicates the presence of carrier backscattering and localization in the nanowires.

Table of Contents

Contents

Acknowledgements	I
Abstract	II
Table of Contents	IV
Chapter 1. Introduction	1
1.1 Motivation	1
1.2 Outline of the thesis	3
References	5
Chapter 2. Experimental techniques	6
2.1 Optical pump – optical probe (OPOP)	6
2.1.1 Temporal evolution of carrier dynamics	10
2.1.2 State filling effect and pump induced absorption	12
2.2 Terahertz time-domain spectroscopy (THz-TDS)	13
2.2.1 Generation and detection of THz electromagnetic waves	15
2.2.2 Bulk sample and thin film sample on substrate	22
2.2.3 Difference in thicknesses between the sample and reference substrate thickness, ΔL	27
2.2.4 Effective medium approximation	28
2.2.5 Dielectric fitting models	30
2.2.6 Conductivity fitting model	31
2.3 Conclusion	34
References	35
Chapter 3. Effect of annealing on the temperature-dependent dielectric properties of LaAlO ₃ at terahertz frequencies	37
3.1 Introduction	37
3.2 Experiment and data analysis	38
3.3 Results and discussion	40
3.3.1 LAO as grown and after annealing process in 0 ° orientation	40
3.3.2 LAO as grown and after annealing process in 90 ° orientation	46
3.4 Conclusion	48
References	49
Chapter 4. Carrier dynamics of graphene probed by optical pump-probe technique	50
4.1 Introduction	50
4.2 Sample preparation and Raman characterization	56
4.3 Pump-probe results of FeCl ₃ -G and BLG samples	58
4.4 Electronic band structure calculation and discussions	61
4.5 Pump fluence effect on the relaxation times of FeCl ₃ -G and BLG samples	64
4.6 Conclusion	66
References	67
Chapter 5. Terahertz Time-Domain spectroscopy studies of bilayer graphene	69
5.1 Introduction	69

5.2 Experimental section.....	72
5.3 Data analysis	73
5.4 Theoretical modeling and discussion.....	76
5.4.1 Chemical potential and charged impurity concentration of BLG by Raman spectroscopy.....	76
5.4.2 Impurity scattering model.....	77
5.4.3 Impurity scattering model fitting	79
5.4.4 Van-Hove singularities in twisted BLG	83
5.5 THz-TDS study of monolayer graphene.....	84
5.6 Conclusion	85
References.....	86
Chapter 6. Terahertz conductivity study of tin oxide nanowire film	88
6.1 Introduction.....	88
6.2 Sample preparation and THz-TDS experiment.....	91
6.3 Results and discussions.....	95
6.3.1 Dielectric properties of SnO ₂ nanowires using simple EMA	95
6.3.2 Complex conductivity fitting and discussion.....	98
6.3.3 Carrier mobility of SnO ₂ nanowires.....	103
6.4 Conclusion	103
References.....	104
Chapter 7. Conclusions and future work.....	106
7.1 Z-cut quartz and LAO single crystal: THz-TDS.....	106
7.2 BLG and FeCl ₃ -G: Optical pump-probe technique	107
7.3 Twisted BLG: THz-TDS study	108
7.4 SnO ₂ nanowires: THz-TDS.....	109
7.5 Future work.....	109
References.....	112

Chapter 1. Introduction

In the introduction, I present the motivation of my thesis. The organization and contents of this thesis are given at the end of this chapter.

1.1 Motivation

Many of recent technologies, whether in InfoTech (IT), Communications Technology or Micro Electronics, utilize the fast response of microelectronic devices. There has been great interest in exploring the limitation of microelectronics by the investigation of fundamental fast processes that occur on a picosecond (ps) or even femtosecond (fs) time scale [1]. These fundamental processes include carrier-carrier scattering, carrier-phonon scattering, electron-spin scattering, charge transfer, carrier diffusion, intervalley and intravalley scattering, etc. Higher speed and smaller size are two desirable features in the semiconductor microelectronics device industry. Transistors, which form the backbone of modern technology, have effective lengths of a few tens of nanometers (nm), with electron transport timescales of the order of ps or faster. This means fabricating smaller devices that allow for a faster device response which, together with functionality and lower cost, are the goals of the semiconductor industry. The development of such high speed devices, especially in semiconductors, requires a clear understanding of the dynamics of the different degrees of freedom in the material, such as electrons and holes (carriers), phonons, spins, etc, as well as the coupling among these degrees of freedom, all on an ultrashort time scale. Also, the carrier relaxation rates in many materials are governed by the phonon-phonon interaction, which determines how

fast the nonequilibrium phonons relax during carrier equilibration.

Ultrafast spectroscopy is a very useful technique to study the electronic and vibrational properties of many solid-state systems [2]. The power of ultrafast spectroscopy is that it has the ability to detect and distinguish the competing degrees of freedom at the fundamental timescales, such as atomic and electronic motion [3]. The basic requirement of any ultrafast spectroscopic equipment is that it can deliver ultrashort pulses with desired wavelengths [4]. In the early days, it was a challenge to produce short-enough (10s of fs) laser pulses, and detect them with high-enough temporal resolution. Short pulses are needed to probe fast processes in a material. By the early 1980s, with the advent of Ti:sapphire lasers, sub-picosecond laser pulses can be routinely and reliably produced. However, measurements of such ultrashort timescales were still a problem, due to the response time of electronic instruments being orders of magnitude slower than the pulse duration. Nowadays, precise optical and electrical techniques have been developed, so that in pump-probe experiments, the experiment resolution is limited only by the laser pulse itself. Today's Ti:sapphire mode-locked lasers reliably produces 1.5 eV (~ 800 nm) pulses of sub-100 fs pulse duration, with pulse energies spanning over six orders of magnitude, ranging from a few nJ (at 80 MHz repetition rate in a laser oscillator) to over 1 mJ (at 1 kHz repetition rate in a regenerative amplified laser). [5]. Frequency-conversion technology allows the generation of laser pulses spanning the x-ray, near-ultraviolet (UV), visible, near- (NIR) and mid-infrared (MIR), all the way to the far-infrared (FIR) or terahertz (THz) regions [6]. This wide range of available wavelengths allows researchers to study ultrafast processes as a function of many parameters, such as wavelength (i.e. photon energy), laser fluence (i.e. photoinduced

carrier density) and temperature (i.e. phonon temperature) in nanomaterials and other strongly-correlated electron systems.

1.2 Outline of the thesis

The purpose of this thesis is to investigate the carrier dynamics in nanomaterials by means of optical-pump optical-probe (OPOP), as well as terahertz time-domain spectroscopy (THz-TDS). The contents of this thesis are organized as follows:

- In chapter 2, the experimental techniques OPOP and THz-TDS are introduced, and their experimental setups, basic principles, data analysis and the theoretical fitting models are explained.
- In chapter 3, the dielectric properties of LaAlO_3 (LAO) substrate are investigated by THz-TDS as a function of temperature. Both annealing effect and crystal orientation can have great impact on its dielectric properties.
- In chapter 4, the carrier dynamics of bilayer graphene (BLG) and BLG intercalated with FeCl_3 are studied by optical pump-probe. By comparing the relaxation processes of photoexcited electrons, we found that FeCl_3 intercalation can greatly modify the electronic band structure and electron relaxation behavior.
- In chapter 5, far-infrared dielectric response of BLG is studied by THz-TDS. On top of a Drude-like response, a peak at 2.7 THz was observed in the real part of the optical conductivity. We relate this peak to the van-Hove singularity introduced by a small rotation between the stacked graphene layers.
- In chapter 6, the complex conductivity of SnO_2 nanowires is measured at different temperatures. Effective medium approximation combined with the Drude-Smith

model allows us to extract the carrier density N , and scattering time τ . The temperature evolution of these parameters is discussed.

- Finally, the conclusions of this thesis are presented in chapter 7, with future work suggested.

References

- [1] A. Othonos, J. Appl. Phys. **83**, 1789 (1998).
- [2] J. Shah, *Ultrafast spectroscopy of semiconductors and semiconductor nanostructures* (Springer Verlag, 1999).
- [3] R. D. Averitt, and A. J. Taylor, J. Phys. Condens. Matter **14**, R1357 (2002).
- [4] C. Rullière, *Femtosecond Laser Pulses : Principles and Experiments* (Springer 2005).
- [5] J.-C. Diels, and W. Rudolph, *Ultrashort laser pulse phenomena : fundamentals, techniques, and applications on a femtosecond time scale* (Elsevier, 2006).
- [6] Y. Z. Ma, T. Hertel, Z. V. Vardeny, G. R. Fleming, and L. Valkunas, in *Carbon Nanotubes* (Springer Berlin, 2008), pp. 321.

Chapter 2. Experimental techniques

In this chapter, I introduce the experimental methods used in my study, and their basic principles. Various theoretical models are presented for describing the dielectric response of metals and semiconductors.

2.1 Optical pump – optical probe (OPOP)

In the optical pump – probe technique as shown in Figure 2.1, an ultrashort pulse is split, by means of a beamsplitter, into two pulses — the pump and the probe. Using the delay stage, the pump and probe pulses arrive at the sample position at different times, which in our setup, can be made as close as 10 fs, and as far as 1 nanosecond (ns). Using lenses and XYZ positioners, the two ultrashort pulses can be made to spatially overlap on the sample. Typically, the intensity of the probe beam is much weaker than the pump, and the probe diameter is considerably smaller than pump, so the probe can measure a region with uniform photogenerated carrier density. The intense pump pulse excites the sample and causes a rise in the electronic temperature. The hot electrons then relax by transferring energy to phonons and spins, and a weaker probe pulse monitors the change in the electronic temperature (via the relaxation of the hot electrons) with time delay (Δt) between the pump and probe pulses. The pump and probe pulses can have the same wavelength (degenerate pump-probe) or different wavelength (non-degenerate pump-probe), both of which probe different dynamical processes/transitions in the sample. The data measured is usually presented in the form of photoinduced change in reflectivity (or normalized differential reflection $\Delta R/R$) or photoinduced change in

transmissivity (or differential transmission $\Delta T / T$), given by

$$\frac{\Delta R}{R} = \frac{R_E - R_0}{R_0}; \quad \frac{\Delta T}{T} = \frac{T_E - T_0}{T_0} \quad (2.1)$$

respectively, where $R_E(T_E)$ is the probe reflection (transmission) after pump excitation and $R_0(T_0)$ is the probe reflection (transmission) before pump excitation. Lock-in detection is used to enhance the experimental resolution to 10^{-6} . The acoustic-optical modulator (AOM) is used to modulate the pump beam and connected to the lock-in amplifier. The pump-probe signal is detected by an avalanche photodetector (APD) with the assistance of lock-in amplifier, as shown in Figure 2.1(a). The actual experimental setup in our lab is shown in Figure 2.1(b). The time-averaged intensities of the probe beam are monitored before and after pump excitation and the differential reflection ($\Delta R / R$) can be measured and recorded in the computer.

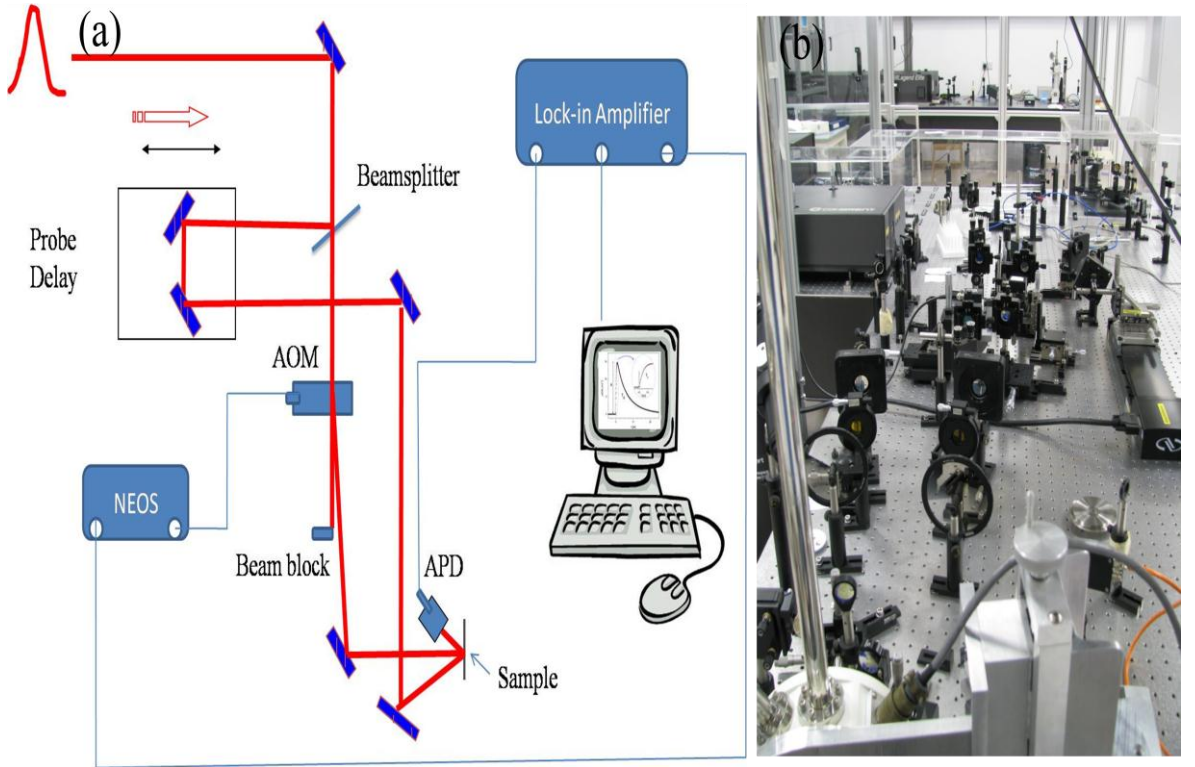


Figure 2.1 A typical pump – probe experiment setup.

The temporal width of the pulses can be determined by measuring the cross-correlation of the pump and probe pulses at the sample position [1]. Group velocity dispersion (GVD) of the pulses when going through the optics results in the temporal spreading of the pulse. Ultrashort pulses will be broadened as the shorter wavelength components travel slower than the longer wavelength components. A pair of prisms can be arranged to produce net negative dispersion, that compensates the positive dispersion going through the optics [2, 3]. In high-power laser amplifier systems, diffraction gratings are often used to produce dispersive effects but with high power loss. Recently, chirped mirrors have been used as an alternative to prisms and gratings. These dielectric mirrors have multiple coatings, so that different wavelengths have different penetration lengths, and achieving a net negative dispersion [4, 5].

A pulse compressor used to compensate this positive group velocity of dispersion is shown in Figure 2.2. The prism compressor typically contains 4 arranged prisms or 2 arranged prisms and a fold mirror. The apex angle of each prism is made to be equal to the Brewster angle for the center frequency, and the prisms are properly arranged so that the beam enters and exits each prism under Brewster angle. This ensures that the reflection losses are minimized for the P-polarized laser beams. The prism compressor shortens the pulse duration by giving different wavelength components different time delays [3]. The shorter wavelength components will lag behind when travelling in the optics. So, by manipulating the position of the prism, we can direct the longer wavelength components to go through more glass and balance the positive chirping by optics [2].

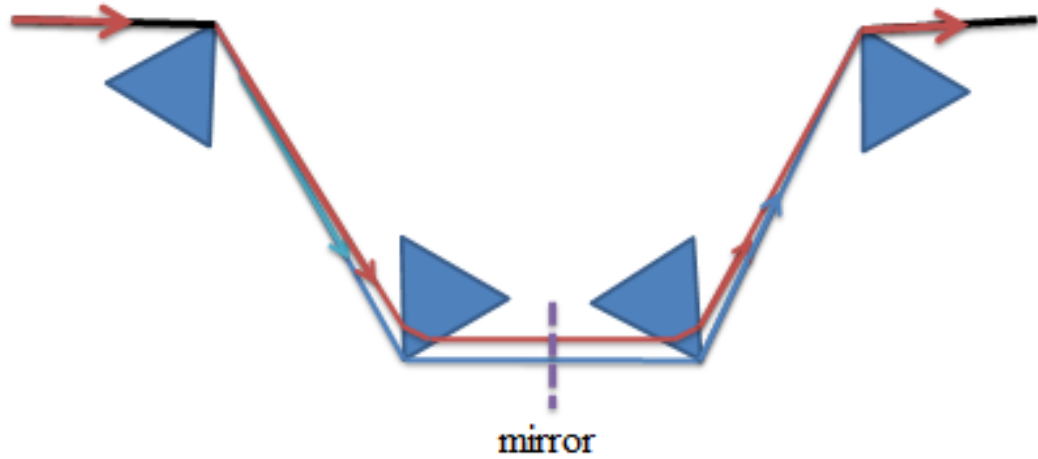


Figure 2.2 Geometry of a prism compressor.

The pump–probe signal is proportional to the integral over the carrier joint density of states at the probe photon energy, which enables the technique to disentangle the electron and hole dynamics. Contrast this to time – resolved photoluminescence (TRPL), whose signal is proportional to the product of electron and hole distributions and thus cannot disentangle of electron and hole dynamics [6]. For example, ultrafast pump–probe technique has been used to study the electron and hole dynamics in germanium nanowires by choosing different probe photon energies [7].

The simplest pump–probe implementation, as described earlier, is to split the ultrashort pulse from a Ti:sapphire oscillator into pump and probe beams. The combination of a high repetition-rate oscillator (80 MHz), fast modulation of the pump beam (~ 100 kHz – 1 MHz), and a sensitive avalanche photodiode, enable the setup to detect very small signals ($\sim \mu\text{V}$), very fast processes (~ 10 fs), using very small pump fluence ($\sim 0.1 \mu\text{J}/\text{cm}^2$) [8]. For some physical systems, however, high excitation intensity and tunable wavelength for the pump and probe beams are needed. Amplified Ti:sapphire

laser systems are used (whether regenerative or multi-pass) to generate high-fluence (μJ – mJ) pulses with repetition rate of $\sim 1\text{-}300$ kHz. These high energy pulses undergo nonlinear optical processes such as optical parametric amplification (OPA) to achieve the generation of pulse wavelengths over a broad frequency range, from ultra violet (UV) to mid-infrared (MIR).

2.1.1 Temporal evolution of carrier dynamics

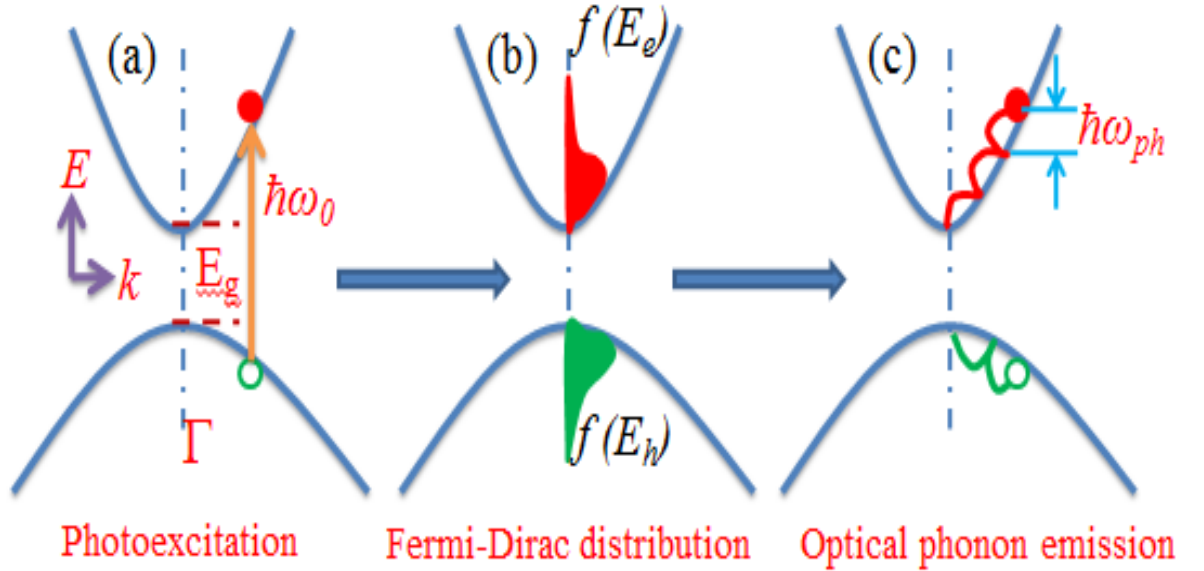


Figure 2.3 Schematic diagrams illustrate the carrier relaxation processes in a semiconductor after ultrashort pulse excitation. (a) Electrons and holes are created by the photoexcitation. (b) Non-equilibrium carrier thermalized into Fermi-Dirac distribution through carrier-carrier scattering. (c) Hot carrier loss their energy by emitting optical phonons.

The carrier dynamics can be described by the changes in the complex dielectric function ($\epsilon_1 + i\epsilon_2$) of the investigating material. In many ultrafast pump-probe

experiments on metals, the photoinduced change in reflectivity R or transmissivity T were expressed in terms of the photoinduced change of the real ($\Delta\varepsilon_1$) and imaginary ($\Delta\varepsilon_2$) parts of the dielectric function, via the expression

$$\frac{\Delta Y}{Y}(t) = \frac{\partial \ln(Y)}{\partial \varepsilon_1} \Delta \varepsilon_1(t) + \frac{\partial \ln(Y)}{\partial \varepsilon_2} \Delta \varepsilon_2(t), \text{ where } Y \text{ can be } R \text{ or } T [9].$$

In order to clearly interpret the results of ultrafast optical experiments, the temporal evolution of the photoexcited carriers after pump excitation should be fully understood. As comprehensive discussions of carrier dynamics are provided in many references, here I only give a general picture of the relaxation of photoexcited carriers [10]. Before the pump beam excitation, free electrons and holes obey Fermi-Dirac statistics, while phonons obey Bose-Einstein statistics. Photoexcitation with photon energy exceeding the band gap creates free electrons in the conduction band, and holes in the valence band. these carriers have narrow distributions in momentum space since the photon momentum is small compared to Brillion zone. (Figure 2.3(a)). At such short times after photoexcitation (~ 10 fs), the electron and hole distributions are *not* Fermi-Dirac like. After a few hundred femtoseconds, electron-electron and hole-hole scattering thermalize the electrons and holes, causing them to obey Fermi-Dirac statistics, resulting in the electronic temperature being higher than the lattice temperature. In semiconductors, sine electrons and holes have (frequently) very different effective masses, the dynamics and distributions of electrons and holes need to be considered separately (Figure 2.3(b)). Similar to metals, the electrons and holes thermalize with each other and reach a common temperature within 1-2 ps. Thereafter, the hot carriers (electrons and holes) relax (i.e. lose their excess energy) to the lattice (phonons) through various scattering mechanisms, typically optical phonon emission (Figure 2.3(c)). The number of

nonequilibrium optical phonons thus increases. These hot optical phonons lose their energy to other lattice modes (both optical and acoustic) through (usually anharmonic) phonon-phonon interaction, on a time scale of a few picoseconds. After these processes, all degrees of freedom (typically carriers and lattice) eventually reach thermal equilibrium with one another.

2.1.2 State filling effect and pump induced absorption

The carrier dynamics of the sample can be studied by measuring the pump-induced change in reflectivity $\Delta R/R$ or transmissivity $\Delta T/T$ of the weak probe beam. Here, we use $\Delta T/T$ to explain the state filling effect and pump induced absorption [1, 11]. As shown in the Figure 2.4, after the pump excitation, the ground state (GS) population of electrons is reduced, while the excited states (ES) are occupied. The occupation of states by photoexcited electrons causes fewer probe photons to be absorbed, hence the transmission of the probe beam increases. The differential reflectivity $\Delta T/T$ is proportional to the pump fluence F , with the relationship $\Delta T / T \propto -\Delta\alpha \times F$, where $\Delta\alpha$ is the change in sample absorbance. Hence, in the state filling scenario, we can get a positive $\Delta T/T$ signal. In some materials which have an abundance of electronic states, the photoexcited electrons can be excited to higher energy states after absorbing the subsequent probe photons, leading to a decrease in the transmission. This increase in absorption caused by the pump excitation will give a negative $\Delta T/T$ signal.

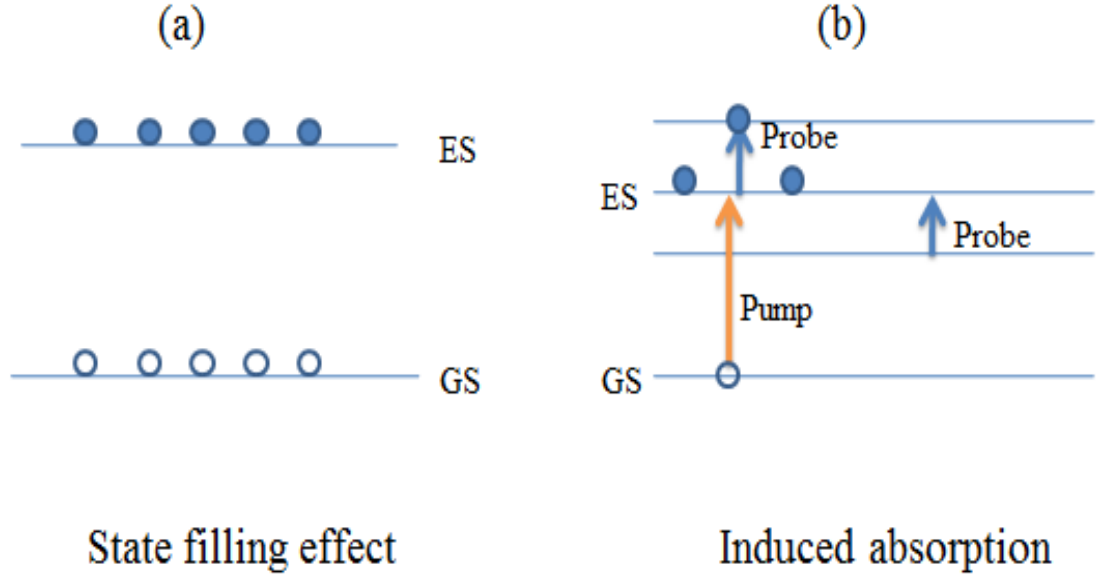


Figure 2.4 Schematic graphs for state filling (a) and pump-induced absorption (b).

2.2 Terahertz time-domain spectroscopy (THz-TDS)

In contrast to other spectroscopic techniques such as Fourier Transform Infrared Spectroscopy (FTIR), THz-TDS spectroscopy has the advantage of directly measuring the *complex* electric field $\tilde{E}(\omega)$, and not simply its amplitude. Both the amplitude *and* phase of the different spectral components of the THz electric field can be obtained [12]. The refractive index $n(\omega)$ and extinction coefficient $k(\omega)$ of the sample can be extracted. Thus the complex-valued permittivity (or equivalently, optical conductivity) of the sample can be obtained without the need for Kramers-Kronig analysis [13]. The majority of the results reported in the literature that use conventional far-IR sources and detectors present only the absorption coefficient which is related to the power absorption in the sample, however, the refractive index is determined by the phase delay of the electromagnetic wave. In this respect, THz-TDS spectroscopy provides a powerful method of determining the material optical properties such as complex refractive index,

conductivity and permittivity.

THz pulses are ideal for probing semiconductors because typical carrier scattering rates of 10^{12} to 10^{14} s^{-1} lie in the THz regime. In different units, one THz can be expressed as:

$$1 \text{ THz} = 300 \text{ } \mu\text{m} = 4.1 \text{ meV} = 33.3 \text{ cm}^{-1} = 47 \text{ K} = 1 \text{ ps}.$$

One THz corresponds to a photon energy of 4.1 meV (33.3 cm^{-1}). The small energies are much less than the semiconductor band gaps which are of the order of an electron volt. In strongly-correlated electron systems and nanomaterials, many basic excitations occur at the lower energies (in the THz range). For example, in transition-metal oxides, the excitation gaps arise from the charge pairing into superconducting condensates and other correlated states [14]. In nanomaterials, band structure quantization can cause infrared and THz transitions such as the intersubband absorption in quantum wells [15, 16]. Also, formation of excitons in turn can lead to low-energy excitations which are similar to inter-level transitions in atoms [17]. This motivates the use of THz wave as a useful tool to study the light-matter interactions in nanomaterials and correlated-electron materials [18]. Device-wise, high speed devices that operate in the THz frequencies [16,18] were developed, such as laser diodes [19], high electron mobility transistors [20], and quantum cascade lasers [21].

Many of the technological difficulties for THz generation and detection have been overcome by using ultrafast optical techniques [18]. The combination of ultrafast optical and electronic techniques has allowed researchers to generate and detect sub-picosecond THz pulses. There are many ways to generate and detect THz radiation using ultrafast optical pulses, but the ones most often used by researchers can be classified in two

categories: resonant (photoconductivity) and non-resonant (electro-optic techniques) [18]. Photoconductive THz generation occurs when optical excitation induces conductivity changes in a semiconductor. This is a resonant interaction and the photons are absorbed through interband transitions. Non-resonant techniques, on the other hand, rely on nonlinear optical techniques for difference frequency generation, nonlinear frequency mixing or optical rectification [22].

2.2.1 Generation and detection of THz electromagnetic waves

Two major mechanisms for THz wave generation and detection will be introduced. One is the photoconductive method using semiconductor antenna, the other is optical rectification method by electro-optic effect.

2.2.1.1 Photoconductive generation and detection of THz pulses

The basic processes of photoconductive THz wave generation are shown in Figure 2.5. Two parallel metal lines are deposited on a semiconductor substrate, which exhibits a high resistivity and high mobility [23]. The two metallic lines are biased by a DC voltage on the order of 10^6 V/m, as shown in Figure 2.5(a). An ultrashort optical pulse with photon energy larger than the semiconductor bandgap excites the semiconductor, creating electrically neutral plasma near the semiconductor surface with a penetration depth of $1/\alpha$ (Figure 2.5(b)). Since the absorption coefficients of semiconductor is large ($\alpha = 10^4 - 10^5 \text{ cm}^{-1}$) for photons with energies larger than the bandgap, the electron-hole pairs are immediately accelerated by the electric field, with the negative electrons accelerate towards the positively biased line while the holes are moving to the negative line, as shown in Figure 2.5(c).

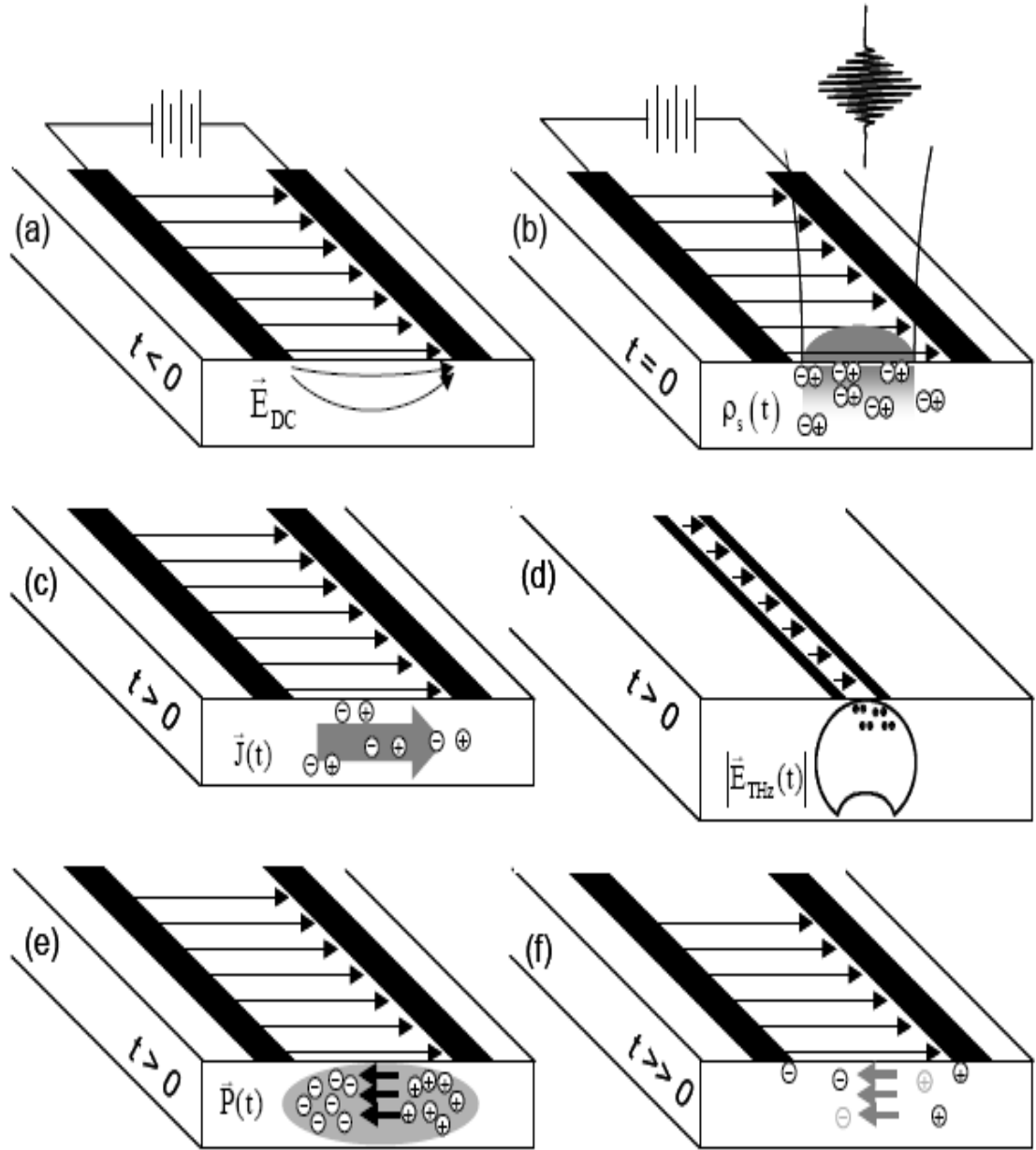


Figure 2.5 Processes of photoconductive THz generation. (a) Two biased metal lines deposited on the semiconductor. (b) Ultrashort pulse excite the substrate. (c) Charge carriers are accelerated by DC field. (d) THz pulses are radiated by the transient current. (e) Polarization is generated by the separating carriers. (f) Return to the initial state. Figure taken from Ref. [23].

As the carriers are accelerating in the electric field, a transient current is developed.

Following the Maxwell's equations:

$$\nabla \times \vec{E}_{THz}(t) = -\mu \frac{\partial \vec{H}_{THz}(t)}{\partial t} \quad (2.2)$$

$$\nabla \times \vec{H}_{THz}(t) = \vec{J}(t) + \frac{\partial}{\partial t}(\varepsilon(t)\vec{E}_{THz}(t)) \quad , \quad (2.3)$$

a THz field is generated by the transient current in Figure 2.5(d). The photo-generated electron and hole carriers travel in opposite directions, and creates a polarization in the semiconductor material, as shown in Figure 2.5(e). Then after a much longer time scale, the carriers recombine and return to the initial unexcited state (Figure 2.5 (f)).

The photoconductive detection of THz pulses using an antenna is shown in Figure 2.6(d). Unlike THz generation, the antenna is not biased, so the electron-hole plasma created by optical pulse will not accelerate in any particular direction, but can cause rapid change in conductivity. The arrival of the optical pulse makes the antenna gap change from insulating to conducting, and the short recombination time of the carriers in the semiconductor makes the gap return to the insulating state on picosecond time scale. The time-averaged current with subpicoamp resolution flowing through the gap will be detected. The current is $I(t) = V(t) / R(t)$, where $V(t) \cong E_{THz}(t) \times h$ is the antenna bias provided by the THz pulse. In Figure 2.6(a), the optical pulse arrives at the antenna before the THz pulse, $t < 0$, so there is no biased pulse, and the current is zero as shown in Figure 2.6(e) point t_A . The time axis is controlled by the delay between optical pulse that generates THz pulse and the pulse that gates the THz antenna. When the positive THz peak arrives at the antenna at the same time instant that the gate pulse arrives, $E_{THz} > 0$, as shown in Figure 2.6(b) point t_B , the current now flows in the same direction with E_{THz} . The measured current is proportional to the THz electric field. As the gate pulse is further delayed, the negative peak of the THz field goes through the antenna with

the gate pulse as shown in Figure 2.6(c). Here a negative current flows through the antenna and is just opposite to that in Figure 2.6(b). Hence a time-resolved trace of the THz pulse can be obtained by changing the time delay between the optical gate pulse and the THz generating pulse.

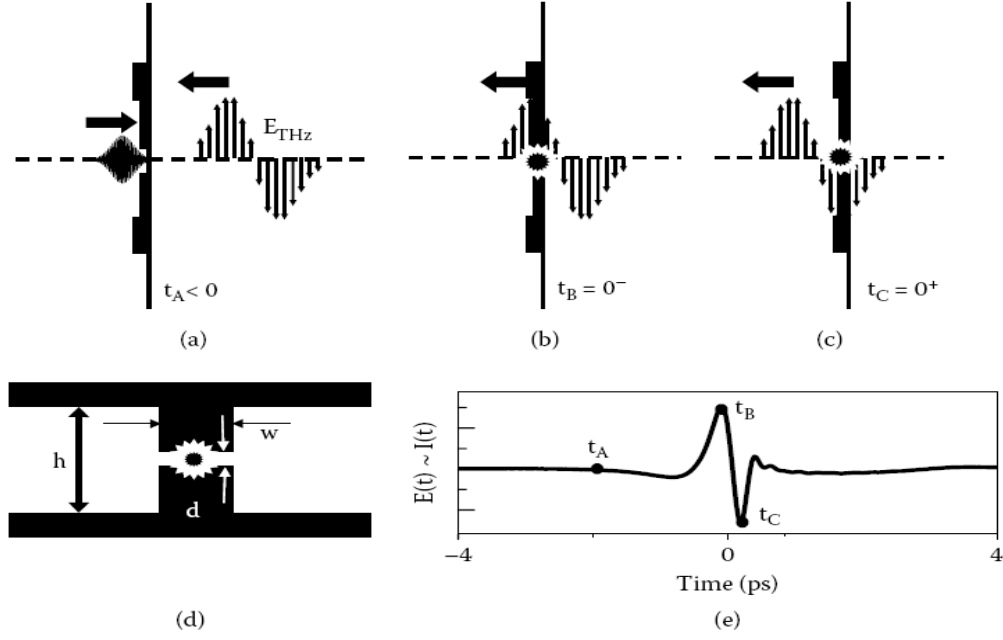


Figure 2.6 Illustration of photoconductive THz detection. The THz antenna of graph (d) is shown in cross section in graphs (a–c). The THz pulse (graph e) is mapped out by delaying arrival of the optical pulse to coincide with the THz pulse as shown in (b) and (c). Figure taken from Ref. [18].

2.2.1.2 Electro-optic generation and detection of THz pulses

THz pulses can also be generated and detected using a nonresonant, nonlinear optical effect without absorbed photons creating mobile charge carriers, as in the photoconductive method. In optical rectification, THz pulse generation depends on the interaction of the optical field with the second order nonlinear optical susceptibility $\chi^{(2)}$ of certain materials. Hence, THz generation by optical rectification occurs throughout the

volume of the nonlinear materials, and is different from the photoconductive method, where the THz radiation is produced only near the surface due to the absorption depth of the optical pulse in the material. High bandwidth THz pulses can be generated by using ultrashort optical pulse — however, to obtain very high THz frequencies, we must use very thin electro-optic (EO) crystal, but at the expense of THz amplitude (since the THz pulse amplitude is proportional to the crystal thickness) [23].

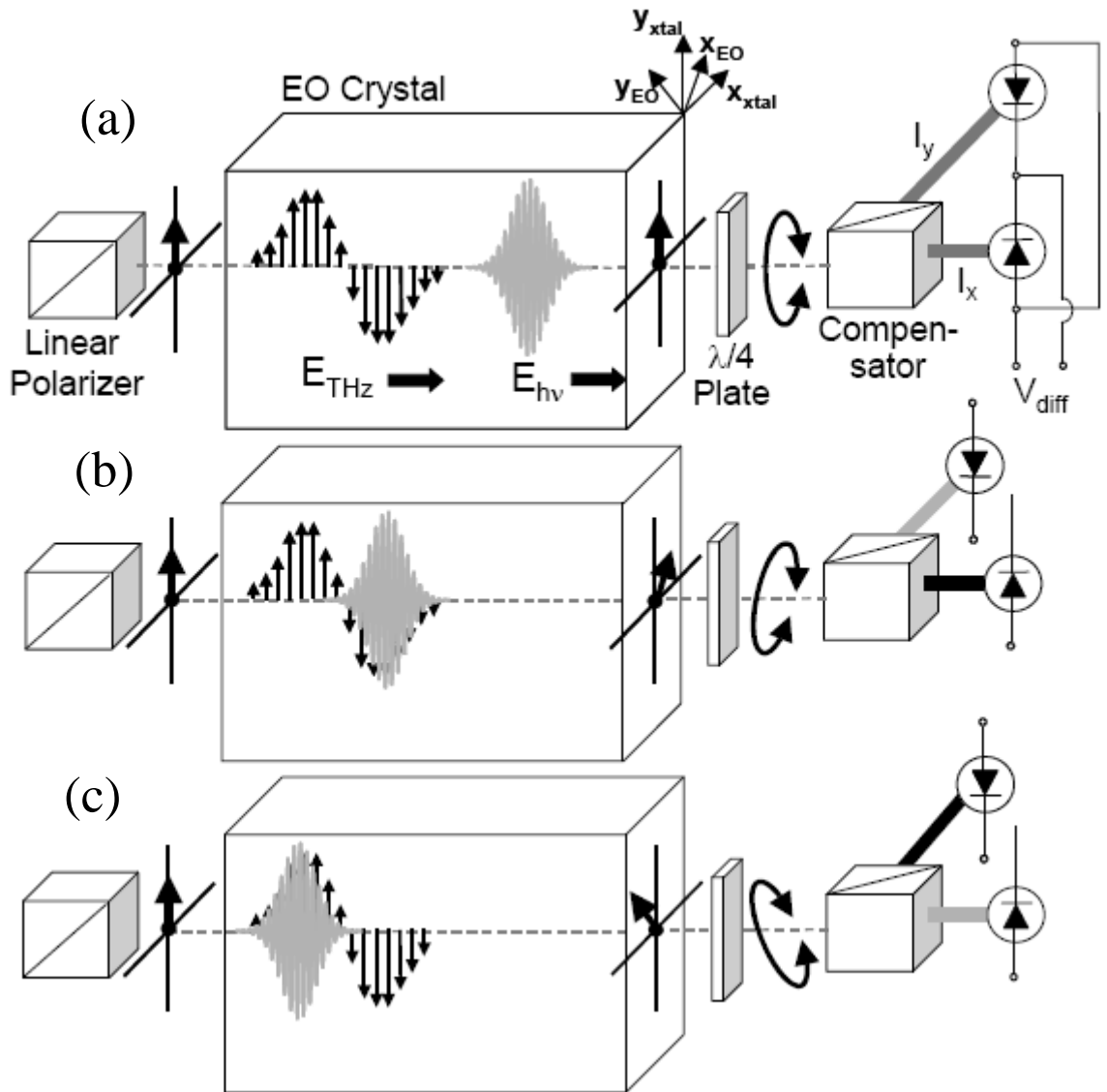


Figure 2.7 THz pulse detection by electro-optic effect. Three relative time delays between the THz and optical pulse are illustrated. Figure taken from Ref. [23].

The detection of the THz pulse uses the Pockel's effect, where the change of refractive index is proportional to the applied electric field [24]. As shown in Figure 2.7, the THz pulse and the optical (gate) pulse are aligned so they are propagating along the same direction. The optical pulse is linearly polarized by placing a polarizer before the EO crystal. The EO crystal is oriented so that the electric field in the y direction will induce birefringence. This electric-field-induced birefringence will cause a polarization rotation of the optical pulse, with the rotation angle proportional to THz electric field amplitude. After the EO crystal, the optical (gate) pulse enters a quarter wave plate, then a Wollaston prism, before entering a balanced photodetector.

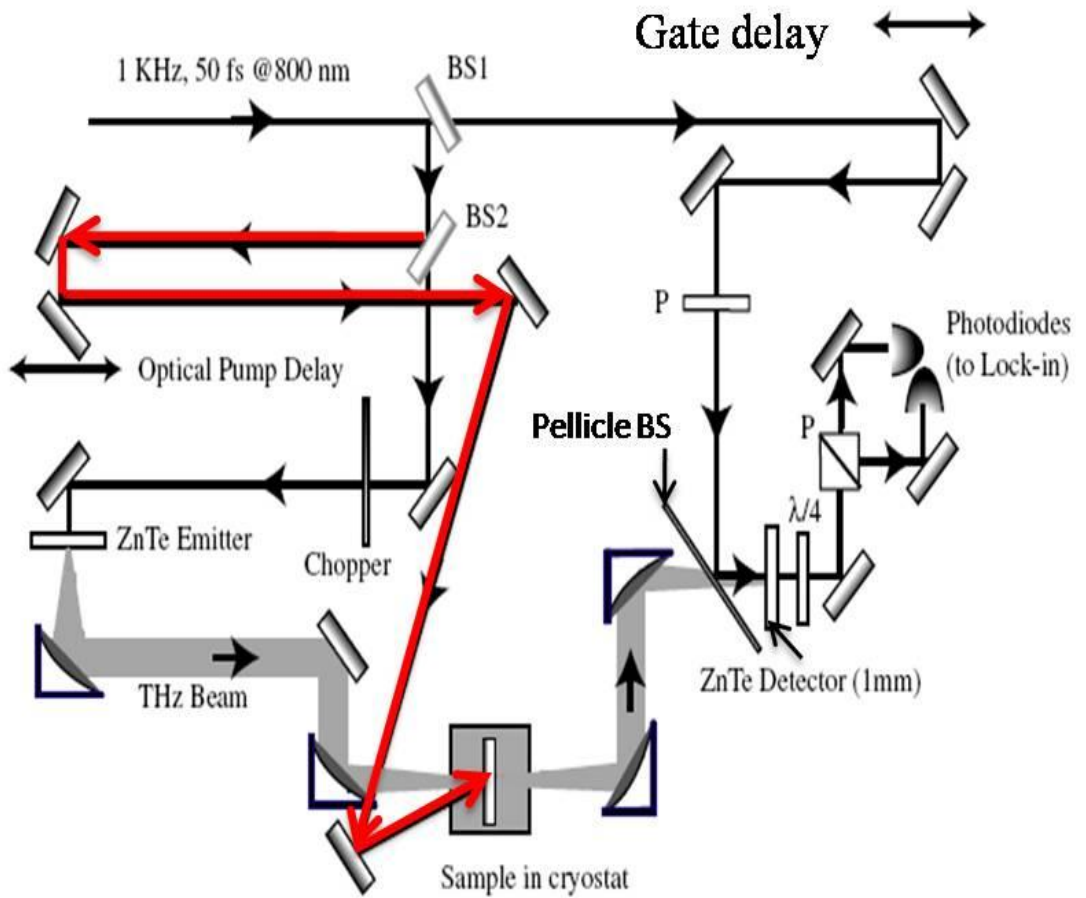


Figure 2.8 The schematic graph of THz-TDS system. Figure taken from Ref. [9].

If the THz and optical pulses are not overlapping in the EO crystal, the THz pulse lags the optical pulse as shown in Figure 2.7(a), and there is no induced birefringence. The polarization of the THz electric field does not change when going through the EO crystal. The linear polarized beam becomes circular polarized after passing through the quarter wave plate. Then, the Wollaston prism (compensator) separates the x and y polarizations of the incoming beam, and sends them to the balanced photodetector which gives a signal proportional to the difference between optical intensities of the x and y polarized components, I_x and I_y . Since there is no birefringence in Figure 2.7(a), circular polarized beam gives equal optical intensity $I_x = I_y$, so the signal is zero.

By changing the delay between the THz and optical (gate) pulses, they are now made to overlap in the $-y$ direction of the THz pulse as shown in Figure 2.7(b). The electric field of the THz pulse induces a birefringence in the EO crystal and causes a change in the polarization of the optical pulse. After the quarter wave plate, the now *elliptically* polarized optical pulse results in the two orthogonal polarized beams having slightly different intensities, and this intensity difference is detected by the balanced photodetector. The phase change of the optical pulse is given by $\Delta\phi = \omega\Delta n d / c$, where ω , d and c are angular frequency, EO crystal thickness and the speed of light, respectively. The change of refractive index is proportional to the electric field:

$\Delta n = \frac{1}{2} r n^3 E$, where r is the Pockel's coefficient. So the relation between phase change

and electric field is expressed as: $\Delta\phi = \frac{1}{2} r n^3 E \omega d / c$. Since typical values of r are very

small, the induced phase change $\Delta\phi \ll \pi$, Hence, polarization change is linearly proportional to the applied THz field, $\Delta\phi \propto E_{THz}$. Figure 2.7(c) shows the case of

optical pulse overlapping with the THz pulse in the $+y$ direction. The polarization rotation is now in the opposite direction and results in an opposite signal compared with the case of Figure 2.7(b). Hence, by changing the relative delay of the optical (gate) and THz pulses, the entire THz pulse can be traced in the time domain [23]. The schematic of the time-domain THz spectroscopy and optical-pump THz-probe setup is illustrated in Figure 2.8. To perform THz-TDS measurements, we only need to block the optical pump beam (the red arrow). The EO crystal used for both THz generation and detection is ZnTe.

2.2.2 Bulk sample and thin film sample on substrate

To study the spectroscopic information of a material, we need a reference material with a well-known complex refractive index in the frequency region under investigation. For bulk materials, we can use vacuum ($\tilde{n} = 1$) as reference. However, to study thin films on a substrate, we need to know the complex refractive index of the substrate. In an experiment, the electric field of the THz pulses passing through the sample $E_s(t)$, then the reference $E_r(t)$, are recorded by moving the sample holder up and down as shown in Figure 2.9(a). After the main pulse, a small etalon pulse appears due to the multiple reflections between the front and back surface of the sample. We can truncate the etalon in the time domain signal since the main pulse and etalon are well separated (Figure 2.9(b)). Fast Fourier transform (FFT) allows us to obtain the frequency spectra information (amplitude and phase) of the sample and reference (Figure 2.9(c)).

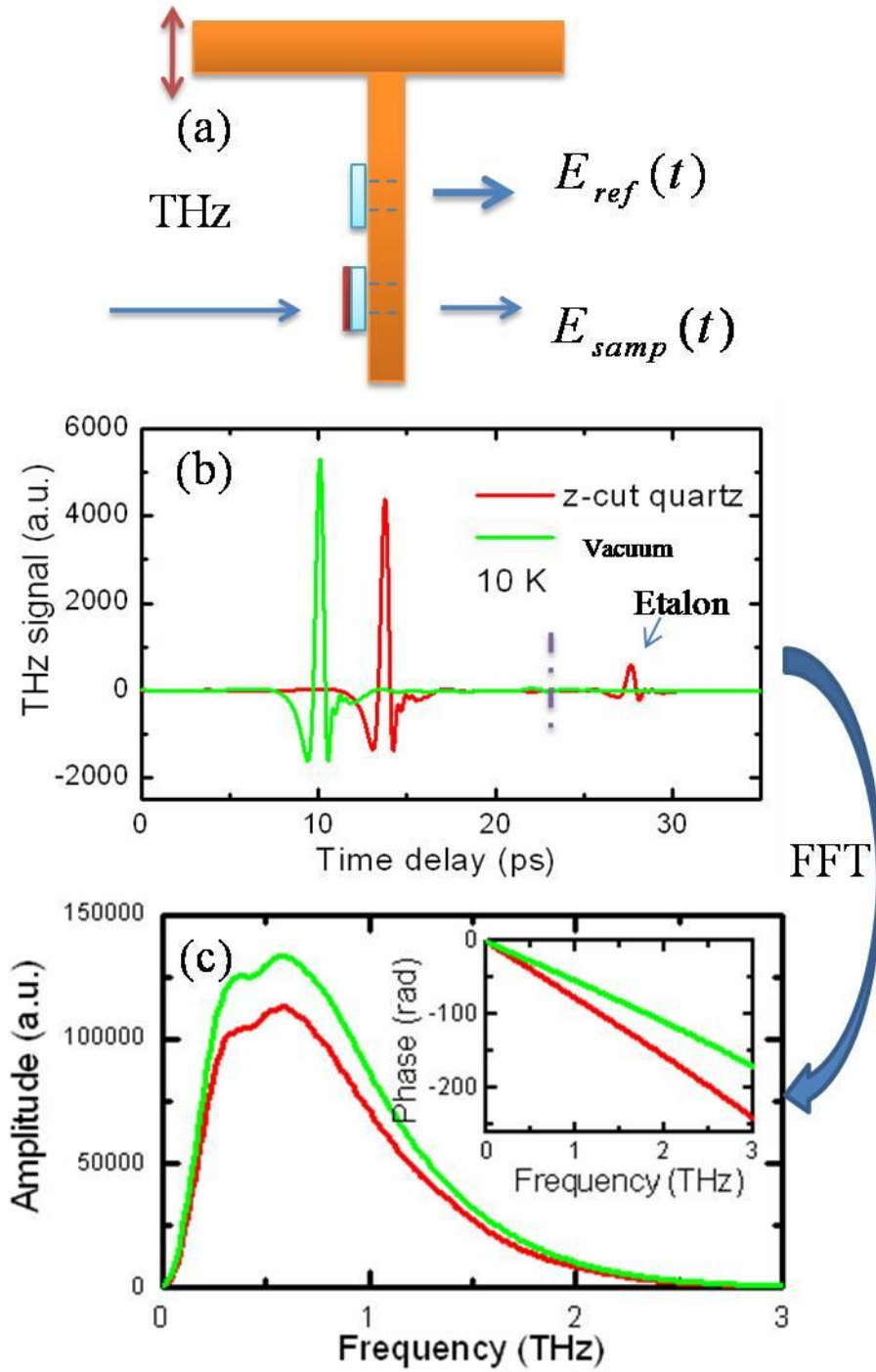


Figure 2.9 (a) THz-TDS sample holder figure. (b) Time domain signal of the THz pulse transmit through 1 mm z-cut quartz and air. (c) Amplitude and phase spectra after FFT of time-domain data in (b).

Without invoking Kramers-Kronig relations, the frequency-dependent complex refractive index $\tilde{n}(\omega)$ can be obtained by solving the equation numerically [25, 26]:

$$\tilde{T}(\omega) = \frac{\tilde{E}_s(\omega)}{\tilde{E}_r(\omega)} = \frac{4\tilde{n}(\omega)}{(1+\tilde{n}(\omega))^2} \exp[i\omega d(\tilde{n}(\omega)-1)/c], \quad (\text{Sample-vacuum}) \quad (2.4)$$

where $\tilde{T}(\omega)$, $\tilde{n}(\omega)$, d are complex transmittance, sample complex refractive index and sample thickness, respectively. After the extraction of $\tilde{n}(\omega)$ from Eq. (2.4), the complex dielectric function can be obtained from the relation $\tilde{\epsilon}(\omega) = (n(\omega) + ik(\omega))^2$.

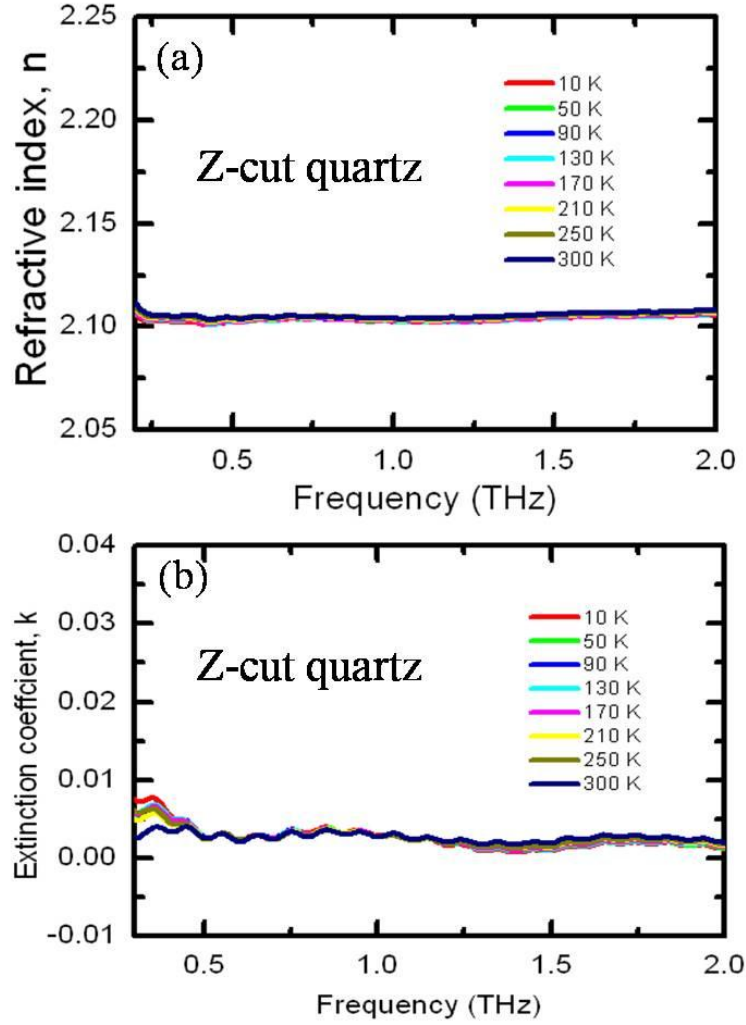


Figure 2.10 The refractive index (a) and extinction coefficient (b) of z-cut quartz at various temperatures.

The n and k of z-cut quartz, a commonly used substrate for THz measurements, at different temperatures are shown in Figure 2.10. The average value of refractive index n

is ~ 2.10 and almost frequency-independent over the whole frequency range (0.2 THz–2 THz). The frequency-independent extinction coefficient k is very small (~ 0.002) showing that z -cut quartz is transparent to THz radiation. The absorption coefficient $\alpha(\omega)$ is related to $k(\omega)$ by: $\alpha(\omega) = 2\omega k(\omega)/c$. The temperature- and frequency-independent properties of n and k have made z -cut quartz as an ideal choice of substrate for THz characterizations.

For thick samples, the main pulse and etalon pulse can be well separated in the time-domain, like in the z -cut quartz in Figure 2.9(b). If the etalon pulse is not removed, then it will cause oscillations in the amplitude of FFT (Figure 2.11) and some oscillations in the following calculation of n and k , as shown in Figure 2.12.

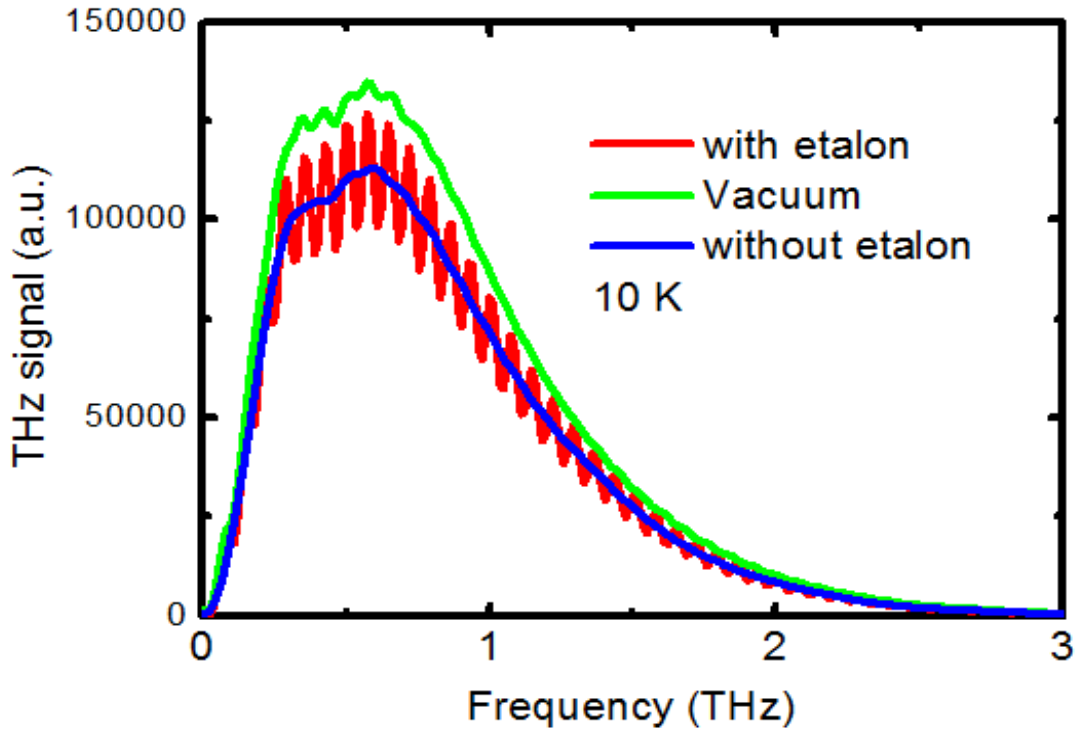


Figure 2.11 Comparison of the FFT amplitude with and without etalon in the time domain signal.

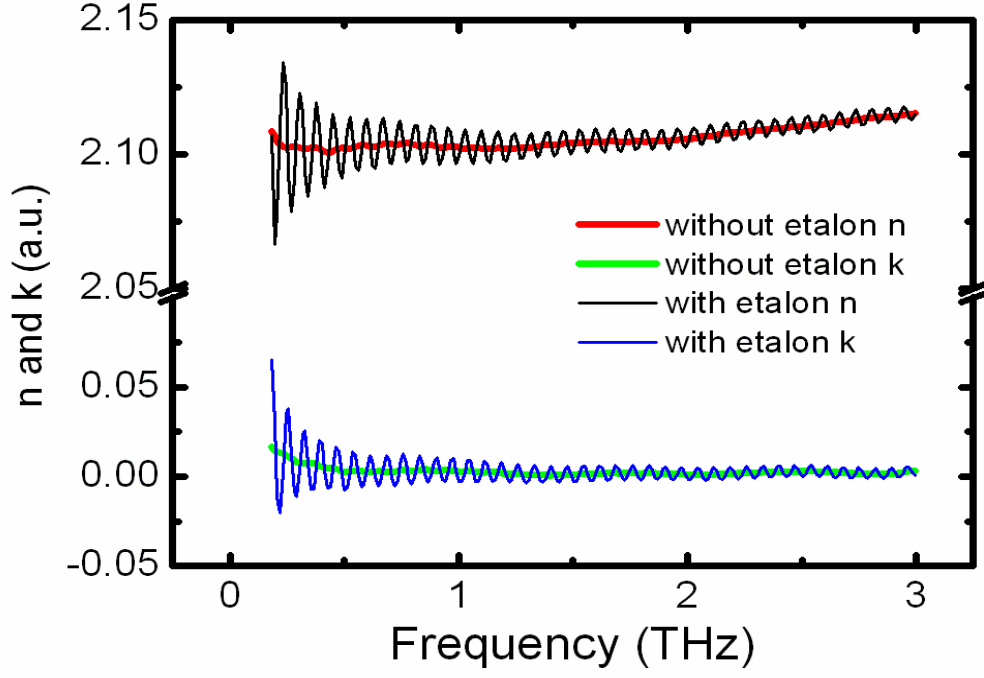


Figure 2.12 Comparison of the extracted n and k with and without etalon in the time-domain signal.

In the case of a thin film sample grown on a substrate, with the reference of a bare substrate, one must take into account (1) multiple reflections in the sample, (2) the difference in the thicknesses of the substrates used for the sample and reference, ΔL , and (3) complex refractive index of the substrate. Equation (2.4) should be modified to include the Fabry-Pérot term ($FP(\omega)$) and ΔL term to be:

$$\tilde{T}(\omega) = \frac{\tilde{E}_s(\omega)}{\tilde{E}_r(\omega)} = \frac{2\tilde{n}(1+\tilde{n}_s)}{(1+\tilde{n})^2(\tilde{n}+\tilde{n}_s)} \exp[i\omega d(\tilde{n}(\omega)-1)/c] * FP(\omega) * \exp[i\omega \Delta L(1-\tilde{n}_s)/c] \quad (\text{Sample-substrate}) \quad (2.5)$$

where \tilde{n}_s is the substrate complex refractive index, and Fabry-Pérot term $FP(\omega)$

which takes into account multiple reflections within the sample can be expressed as:

$$FP(\omega) = \sum_{p=0}^{+\infty} \left\{ \left(\frac{\tilde{n}-1}{\tilde{n}+1} \right) \left(\frac{\tilde{n}-\tilde{n}_s}{\tilde{n}+\tilde{n}_s} \right) \exp[2i\omega \tilde{n}d/c] \right\}^p, \quad (2.6)$$

where p indicates the number of multiple reflections. For no multiple reflection, $p = 0$, so

$FP(\omega) = 1$. For nanometer thin films, we assume infinite multiple reflections inside the film, so $p \rightarrow \infty$, and

$$FP(\omega) = \frac{1}{1 - \left(\frac{\tilde{n} - 1}{\tilde{n} + 1} \right) \left(\frac{\tilde{n} - \tilde{n}_s}{\tilde{n} + \tilde{n}_s} \right) \exp[2i\omega\tilde{n}d / c]} \quad (2.7)$$

2.2.3 Difference in thicknesses between the sample and reference substrate thickness, ΔL

In measuring a thin film sample grown on substrate, since the THz pulse suffers a much smaller phase delay through the thin film than through the much thicker substrate, an accurate determination of the thickness difference between the sample and reference substrate ΔL is crucial for the accurate extraction of the optical constants of the thin film [27]. Before growing the thin film sample, we need to characterize the sample and reference substrates by THz-TDS: from their phase difference we can accurately calculate the ΔL by using the formula [25]:

$$n(\omega) = n_0 - \frac{c}{\omega \Delta L} \Delta \phi \quad (2.8)$$

where $n(\omega)$ and n_0 are refractive index of substrate and vacuum respectively; ω is the frequency and $\Delta \phi$ is phase difference between the two substrates.

The substrate thickness difference ΔL should then be taken into account in the extraction of the optical parameters, and putting Eq. (2.7) into Eq. (2.5), the transmission coefficient $\tilde{T}(\omega)$ now becomes:

$$\tilde{T}(\omega) = \frac{\tilde{E}_s(\omega)}{\tilde{E}_r(\omega)} = \frac{2\tilde{n}(\tilde{n}_s + 1) \exp[i\omega d(\tilde{n} - 1) / c] \exp[i\omega \Delta L(1 - \tilde{n}_s) / c]}{(1 + \tilde{n})(\tilde{n} + \tilde{n}_s) + (\tilde{n} - 1)(\tilde{n}_s - \tilde{n}) \exp[2i\omega d\tilde{n} / c]} \quad (2.9)$$

If the sample substrate is thicker than the reference substrate, then $\Delta L < 0$, and vice versa.

Equation (2.9) is our final working equation for the case of thin film grown on a

substrate.

2.2.4 Effective medium approximation

In some nanostructured materials, the sample is a composite of pure nanowires/nanoparticles and the surrounding matrix, such as air. One has to disentangle the contribution of the matrix from the composite before obtaining the frequency-dependent dielectric properties of the pure material. This is frequently accomplished by using the effective medium approximation (EMA) [28-30]. By approximately taking into account the electromagnetic interactions between the pure material and host matrix, EMA can be used to calculate the dielectric function of a composite material, given the (1) dielectric function and (2) volume fraction, of each of the individual components. Conversely, it can also be used to calculate the dielectric function of one component when the other component and the composite dielectric function are known. A few types of EMAs have been used in literature, namely the Maxwell-Garnett (MG) model, the Bruggeman (BR) model, and the simple effective medium model [30].

In the MG model [31], the nanowires are well separated by the host material. Thus, the interactions between the nanowires are ignored. The MG effective dielectric function can be obtained by the relation

$$\frac{\epsilon_{eff} - \epsilon_h}{\epsilon_{eff} + 2\epsilon_h} = f \frac{\epsilon_m - \epsilon_h}{\epsilon_m + 2\epsilon_h} \quad (\text{MG}) \quad (2.10)$$

where ϵ_{eff} , ϵ_h , and ϵ_m are the dielectric constants of the material-host composite, the host medium, and the pure material, respectively, and f is the filling factor defined by the volume ratio of pure materials to the composites. If there are two materials embedded in the host medium (matrix), with dielectric constants ϵ_{m1} and ϵ_{m2} , and filling factors f_1

and f_2 , respectively, then

$$\frac{\varepsilon_{eff} - \varepsilon_h}{\varepsilon_{eff} + 2\varepsilon_h} = f_1 \frac{\varepsilon_{m1} - \varepsilon_h}{\varepsilon_{m1} + 2\varepsilon_h} + f_2 \frac{\varepsilon_{m2} - \varepsilon_h}{\varepsilon_{m2} + 2\varepsilon_h}. \quad (\mathbf{MG}) \quad (2.11)$$

For the BR approximation [32], interactions are considered between nanowires/nanoparticles. Therefore, the BR model is more applicable in the case of large volume fraction of the nanowires/nanoparticles. In the BR model, the inclusion and host materials are treated equally and self-consistently. The effective dielectric function for a two-phase system can be expressed as:

$$f \left(\frac{\varepsilon_m - \varepsilon_{eff}}{\varepsilon_m + K\varepsilon_{eff}} \right) + (1-f) \left(\frac{\varepsilon_h - \varepsilon_{eff}}{\varepsilon_h + K\varepsilon_{eff}} \right) = 0 \quad (\mathbf{BR}) \quad (2.12)$$

Here, “ K is a geometric factor. K is 1 for an array of cylinders with its axis collinear with the incident radiation and 2 for spherical nanoparticles” [33]. In the case of nanomaterial-air composite, rearranging Eq. (2.12) to solve for the dielectric function of nanomaterial, ε_m , with equal to unity for air $\varepsilon_h = 1$, gives

$$\varepsilon_m = \frac{\varepsilon_{eff} [f(1 + K\varepsilon_{eff}) + (1-f)K(\varepsilon_{eff} - 1)]}{f(1 + K\varepsilon_{eff}) + (1-f)(1 - \varepsilon_{eff})} \quad (\mathbf{BR}) \quad (2.13)$$

Then the refractive index and extinction coefficient can be obtained respectively from the dielectric function $\tilde{\varepsilon} = \varepsilon_1 + i\varepsilon_2$, $\tilde{\varepsilon}$ is the complex dielectric function, ε_1 and ε_2 are the real and imaginary parts of the $\tilde{\varepsilon}$.

$$n = \left(\frac{1}{2} (\varepsilon_1^2 + \varepsilon_2^2)^{1/2} + \frac{\varepsilon_1}{2} \right)^{1/2} \quad (2.14)$$

$$\text{and } k = \left(\frac{1}{2} (\varepsilon_1^2 + \varepsilon_2^2)^{1/2} - \frac{\varepsilon_1}{2} \right)^{1/2} \quad (2.15)$$

The simple EMA is often used to describe the dielectric function of a composite of two components [34]. The formula can be expressed:

$$\varepsilon_{eff} = f\varepsilon_m + (1-f)\varepsilon_h \quad (\mathbf{Simple EMA}) \quad (2.16)$$

Different EMA models were used for different materials [34]. For example, the simple EMT was found to work with ZnO nanostructures [29], while the BR model works well for tubular and prism-like structures.

2.2.5 Dielectric fitting models

After the experimental dielectric functions ε_m of the pure nanowires/nanoparticles have been obtained from Eq. (2.13), we can then choose appropriate dielectric models to fit the experimental data and extract the optical parameters. In the THz regime, the dielectric function $\tilde{\varepsilon}(\omega)$ consists of contributions from three sources: (1) high-frequency dielectric constant, (2) conduction (free) carriers, and (3) lattice vibrations (phonons). The interaction of THz radiation field with the material determines which model we should use. For metals (and some semiconductors), where free electrons (carriers) dominate the optical response, we neglect the contribution from phonons and adopt the Drude model [29]:

$$\tilde{\varepsilon}(\omega) = \varepsilon_\infty - \frac{\omega_p^2}{\omega^2 + i\gamma\omega} \quad (2.17)$$

The first term ε_∞ is the high-frequency dielectric constant which is a collection of absorbing modes with frequency beyond the maximum investigation frequency ω_m and can be expressed as $\varepsilon_\infty = 1 + \frac{2}{\pi} \int_{\omega_m}^{\infty} \frac{\varepsilon_2(\omega)}{\omega} d\omega$, where $\varepsilon_2(\omega) = 2nk$ is the imaginary part of the dielectric function. The second term of Eq. (2.17) describes the response of the unbound (free) charge carriers. From the plasma frequency $\omega_p = \sqrt{\frac{Ne^2}{\varepsilon_0 m^*}}$ and the scattering rate γ , we can obtain the carrier density N and the effective mass m^* . ε_0 is the free-space permittivity constant ($= 8.854 \times 10^{-12}$ F/m). The mobility can be obtained from

γ via the relation $\mu = e / (m^* \gamma)$.

On the other hand, if lattice vibrations play a dominant role, via phonons absorbing electromagnetic energy, then the dielectric function $\tilde{\epsilon}(\omega)$ has a term arising from the lattice vibrations, and the contribution from free electrons can be neglected. Then the dielectric function can be expressed by the Lorentz model [29]:

$$\tilde{\epsilon}(\omega) = \epsilon_{\infty} + \sum_j \frac{A_j \omega_j^2}{\omega_j^2 - \omega^2 - i\Gamma_j \omega} \quad (2.18)$$

It describes a collection of Lorentz oscillators, where A_j, ω_j, Γ_j are the oscillator strength, oscillator resonance frequency and oscillator damping constant (spectral width) of the j^{th} oscillator, respectively.

In the Drude-Lorentz model [35, 36], the frequency-dependent dielectric function can be described by summing over various oscillators and a residual Drude contribution:

$$\tilde{\epsilon}(\omega) = \epsilon_{\infty} - \frac{\omega_j^2}{\omega^2 + i\gamma\omega} + \sum_j \frac{A_j \omega_j^2}{\omega_j^2 - \omega^2 - i\Gamma_j \omega} \quad (2.19)$$

2.2.6 Conductivity fitting model

For some conductive materials, it is more appropriate to consider the conductivity spectrum $\tilde{\sigma}(\omega)$ rather than the dielectric function $\tilde{\epsilon}(\omega)$. From the complex refractive index, we can obtain the complex optical conductivity $\tilde{\sigma}(\omega) = \sigma_1(\omega) + i\sigma_2(\omega)$ by using the relationship: $\sigma_1(\omega) = 2nk\omega\epsilon_0$; $\sigma_2(\omega) = (\epsilon_{\infty} - n^2 + k^2)\omega\epsilon_0$. The optical conductivity of metals and some conductive semiconductors is described in the Drude model by

$$\tilde{\sigma}(\omega) = \frac{Ne^2\tau / m^*}{(1 - i\omega\tau)} \quad (\text{Drude}) \quad (2.20)$$

N, e, m^* and τ stand for the carrier density, electric charge, effective mass and relaxation time, respectively. The Drude model works well with free electrons in a metal,

where scattering events are completely elastic. The real part of conductivity $\sigma_1(\omega)$ decreases with increasing frequency and has its maximum value at zero frequency, while the imaginary part of conductivity $\sigma_2(\omega)$ is positive with a maximum at the frequency of carrier scattering rate. However, in some nanomaterials and poor metals [30, 37, 38], the conductivity deviates from the Drude model with (1) a non-zero frequency maximum in real conductivity and (2) a negative imaginary conductivity.

The negative imaginary conductivity is often attributed to the backward scattering of electrons off defects, grain boundaries, interfaces and surfaces [30]. This backward scattering can be modeled by including an additional term to the Drude model, via a “persistence-of-velocity parameter” c_1 . Such a model, called the Drude-Smith model [37], is given by

$$\tilde{\sigma}(\omega) = \frac{Ne^2\tau/m^*}{(1-i\omega\tau)} \left[1 + \frac{c_1}{(1-i\omega\tau)} \right] \quad \textbf{(Drude-Smith)} \quad (2.21)$$

The parameter c_1 takes into account the fact that, after the first collision, some fraction of the carrier’s initial velocity is retained. For the Drude case $c_1 = 0$, while for complete carrier backscattering $c_1 = -1$. The calculation of imaginary part conductivity $\sigma_2(\omega) = (\varepsilon_\infty - n^2 + k^2)\omega\varepsilon_0$ depends on the value of ε_∞ , which varies for different investigation frequencies and temperatures. So, the best way is to treat ε_∞ as a fitting parameter. In practice, we initially set $\varepsilon_\infty = 1$ to calculate $\sigma_2(\omega)$, then we *simultaneously* fit $\sigma_1(\omega)$ and $\sigma_2(\omega)$ to the expression:

$$\tilde{\sigma}(\omega) = \frac{Ne^2\tau/m^*}{(1-i\omega\tau)} \left[1 + \frac{c_1}{(1-i\omega\tau)} \right] - i\omega\varepsilon_0(\varepsilon_\infty - 1), \quad \textbf{(Drude-Smith)} \quad (2.22)$$

then use the fitted value of ε_∞ to calculate $\sigma_2(\omega)$. The Drude-Smith model has been used to fit the conductivity data of a variety of poor metals such as $\text{Al}_{63.5}\text{Cu}_{24.5}\text{Fe}_{12}$

quasicrystals [37], and ZnO semiconductor nanomaterials [30]. However, the Drude-Smith model explains the conductivity deviation from the Drude model under the assumption that the carriers retain part of their momentum only at the first scattering event, which has no clear physical basis [39]. The plasmon model offers an extension to the Drude model and gives a similar conductivity spectrum to the Drude-Smith model. In the plasmon model, the motion of carriers is controlled by a restoring force and an external electromagnetic wave. The external THz wave acts as an oscillating electric field that displaces the electron and holes in different directions causing the charges to accumulate at the surfaces. This charge redistribution leads to a restoring force (electrostatic in origin) that drives the carriers back to their original position, resulting in a damped harmonic oscillation [39-42]. The conductivity of the Plasmon model can be expressed as:

$$\tilde{\sigma}(\omega) = \frac{N\tau e^2 / m^*}{1 - i\omega\tau(1 - \omega_0^2 / \omega^2)} \quad \textbf{(Plasmon)} \quad (2.23)$$

The $\sigma_1(\omega)$ is maximum and $\sigma_2(\omega)$ crosses over the frequency axis at plasmon resonance frequency ω_0 . A larger restoring force will shift the ω_0 to higher frequency, as $\omega_0 \propto \sqrt{N}$.

In terms of conductivity, the Lorentz model is expressed as:

$$\tilde{\sigma}(\omega) = \sum_j \frac{\omega_{pj}^2 \epsilon_0 \omega}{i(\omega_{0j}^2 - \omega^2) + \gamma\omega} \quad \textbf{(Lorentz)} \quad (2.24)$$

The $j=1,2,3,\dots$, indicates the number of oscillators, and the Drude-Lorentz model can be expressed:

$$\tilde{\sigma}(\omega) = \frac{\epsilon_0 \omega_p^2}{\gamma - i\omega} + \sum_j \frac{\omega_{pj}^2 \epsilon_0 \omega}{i(\omega_{0j}^2 - \omega^2) + \gamma\omega} \quad \textbf{(Drude-Lorentz)} \quad (2.25)$$

As in the Drude-Smith model, in practice, we initially set $\epsilon_\infty = 1$, then obtain the fitted

value of ε_∞ . So the Lorentz model Eq. 2.23 and Drude-Lorentz model Eq. 2.24 become:

$$\tilde{\sigma}(\omega) = \sum_j \frac{\omega_{pj}^2 \varepsilon_0 \omega}{i(\omega_{0j}^2 - \omega^2) + \gamma \omega} - i\omega \varepsilon_0 (\varepsilon_\infty - 1) \quad \textbf{(Lorentz)} \quad (2.26)$$

$$\tilde{\sigma}(\omega) = \frac{\varepsilon_0 \omega_p^2}{\gamma - i\omega} + \sum_j \frac{\omega_{pj}^2 \varepsilon_0 \omega}{i(\omega_{0j}^2 - \omega^2) + \gamma \omega} - i\omega \varepsilon_0 (\varepsilon_\infty - 1) \quad \textbf{(Drude-Lorentz)} \quad (2.27)$$

2.3 Conclusion

Two experimental techniques, ultrafast optical pump-optical probe and terahertz time-domain spectroscopy, are introduced in this chapter — their basic principles and experimental setups. Data analysis and various theoretical dielectric models are also described.

References

- [1] R. P. Prasankumar, P. C. Upadhyaya, and A. J. Taylor, *Phys. Status Solidi B* **246**, 1973 (2009).
- [2] R. E. Sherriff, *J. Opt. Soc. Am. B: Opt. Phys.* **15**, 1224 (1998).
- [3] R. L. Fork, O. E. Martinez, and J. P. Gordon, *Opt. Lett.* **9**, 150 (1984).
- [4] A. Gitin, *Opt. Commun.* **285**, 1375 (2012).
- [5] J. Hebling, E. J. Mayer, J. Kuhl, and R. Szipocs, *Opt. Lett.* **20**, 919 (1995).
- [6] T. B. Norris, K. Kim, J. Urayama, Z. K. Wu, J. Singh, and P. K. Bhattacharya, *J. Phys. D: Appl. Phys.* **38**, 2077 (2005).
- [7] R. P. Prasankumar, S. Choi, S. A. Trugman, S. T. Picraux, and A. J. Taylor, *Nano Lett.* **8**, 1619 (2008).
- [8] M. Hase, M. Kitajima, A. M. Constantinescu, and H. Petek, *Nature* **426**, 51 (2003).
- [9] R. D. Averitt, and A. J. Taylor, *J. Phys. Condens. Matter* **14**, R1357 (2002).
- [10] F. Rossi, and T. Kuhn, *Rev. Mod. Phys.* **74**, 895 (2002).
- [11] L. J. Carlson, and T. D. Krauss, *Acc. Chem. Res.* **41**, 235 (2008).
- [12] C. A. Schmuttenmaer, *Chem. Rev.* **104**, 1759 (2004).
- [13] A. B. Kuzmenko, *Rev. Sci. Instrum.* **76**, 083108 (2005).
- [14] J. Bardeen, L. N. Cooper, and J. R. Schrieffer, *Phys. Rev.* **108**, 1175 (1957).
- [15] M. D. Frogley, J. F. Dynes, M. Beck, J. Faist, and C. C. Phillips, *Nat. Materials* **5**, 175 (2006).
- [16] B. E. Cole, J. B. Williams, B. T. King, M. S. Sherwin, and C. R. Stanley, *Nature* **410**, 60 (2001).
- [17] C. W. Luo, K. Reimann, M. Woerner, T. Elsaesser, R. Hey, and K. H. Ploog, *Phys. Rev. Lett.* **92**, 047402 (2004).
- [18] S. L. Dexheimer, *Terahertz spectroscopy : principles and applications* (CRC Press, 2008).
- [19] D. S. Kurtz, J. L. Hesler, T. W. Crowe, and R. M. Weikle, *IEEE Trans. Microw. Theory Tech.* **50**, 2610 (2002).
- [20] C. H. Lin, T. A. Merz, D. R. Doust, J. Joh, J. A. del Alamo, U. K. Mishra, and L. J. Brillson, *IEEE Trans. Electron Devices* **59**, 2667 (2012).
- [21] A. Tredicucci, R. Kohler, L. Mahler, H. E. Beere, E. H. Linfield, and D. A. Ritchie, *Semicond. Sci. Technol.* **20**, S222 (2005).
- [22] A. Rice, Y. Jin, X. F. Ma, X. C. Zhang, D. Bliss, J. Larkin, and M. Alexander, *Appl. Phys. Lett.* **64**, 1324 (1994).
- [23] D. M. Mittleman, and R. A. Cheville. *Terahertz Generation and Applications.pdf*, <http://frog.gatech.edu/ultratext.html>.
- [24] B. Chmielak, M. Waldow, C. Matheisen, C. Ripperda, J. Bolten, T. Wahlbrink, M. Nagel, F. Merget, and H. Kurz, *Opt. Express* **19**, 17212 (2011).
- [25] W. Withayachumnankul, B. M. Fischer, H. Y. Lin, and D. Abbott, *J. Opt. Soc. Am. B* **25**, 1059 (2008).
- [26] L. Duvillaret, F. Garet, and J. L. Coutaz, *IEEE J. Sel. Top. Quantum Electron.* **2**, 739 (1996).
- [27] C. Kadlec, V. Skoromets, F. Kadlec, H. Němec, J. Hlinka, J. Schubert, G. Panaitov, and P. Kužel, *Phys. Rev. B* **80**, 174116 (2009).

- [28] C. Kang, I. H. Maeng, S. J. Oh, S. C. Lim, K. H. An, Y. H. Lee, and J.-H. Son, *Phys. Rev. B* **75**, 085410 (2007).
- [29] J. G. Han, W. Zhang, W. Chen, S. Ray, J. Zhang, M. X. He, A. K. Azad, and Z. Y. Zhu, *J. Phys. Chem. C* **111**, 13000 (2007).
- [30] J. B. Baxter, and C. A. Schmuttenmaer, *J. Phys. Chem. B* **110**, 25229 (2006).
- [31] J. C. M. Garnett, *Philos. Trans. R. Soc. London, Ser. A* **203**, 385 (1904).
- [32] D. A. G. Bruggeman, *Ann. Phys.* **24**, 636 (1935).
- [33] M. R. Black, Y. M. Lin, S. B. Cronin, O. Rabin, and M. S. Dresselhaus, *Phys. Rev. B* **65**, 195417 (2002).
- [34] H. C. Weissker, J. Furthmüller, and F. Bechstedt, *Phys. Rev. B* **67**, 165322 (2003).
- [35] A. B. Kuzmenko, *Rev. Sci. Instrum.* **76**, 083108 (2005).
- [36] D. Talbayev, A. D. LaForge, S. A. Trugman, N. Hur, A. J. Taylor, R. D. Averitt, and D. N. Basov, *Phys. Rev. Lett.* **101**, 247601 (2008).
- [37] N. V. Smith, *Phys. Rev. B* **64**, 155106 (2001).
- [38] G. M. Turner, M. C. Beard, and C. A. Schmuttenmaer, *J. Phys. Chem. B* **106**, 11716 (2002).
- [39] H. K. Nienhuys, and V. Sundstrom, *Appl. Phys. Lett.* **87**, 012101 (2005).
- [40] R. Ulbricht, E. Hendry, J. Shan, T. F. Heinz, and M. Bonn, *Rev. Mod. Phys.* **83**, 543 (2011).
- [41] J. Lloyd-Hughes, and T. I. Jeon, *J Infrared Milli Terahz Waves* **33**, 871 (2012).
- [42] H. Nemec, P. Kuzel, and V. Sundstrom, *J. Photochem. Photobiol., A* **215**, 123 (2010).

Chapter 3. Effect of annealing on the temperature-dependent dielectric properties of LaAlO_3 at terahertz frequencies

In this chapter, temperature-dependent dielectric properties of lanthanum aluminate (LAO) are studied by terahertz time-domain spectroscopy. Both annealing and crystal orientation have great impact on the dielectric properties of LAO. This study provides important information for the investigation of functional thin films grown on the LAO substrate.

3.1 Introduction

Lanthanum aluminate (LaAlO_3 , LAO) is a rhombohedrally-distorted perovskite commonly used as a substrate for high-temperature superconductors and functional thin films [1]. A cubic-to-rhombohedral transition in LAO occurs at $T_c \approx 850$ K, that is caused by the rotation or tilt of the oxygen octahedra (AlO_6) along the (111) cubic unit cell direction [2]. In order to understand the structural and optical properties of LAO, many experimental and theoretical studies have been performed, for example, neutron diffraction, Raman and infrared spectra, and microwave absorption [3-7]. Room-temperature absorption spectra were also studied at terahertz (THz) frequencies which contain information of large molecule and intermolecular vibrations [8, 9].

In addition, LAO is one of the most commonly used substrates in the growth of complex functional thin films such as high-temperature superconductors, multiferroics and manganites. In such strongly correlated electron systems, due to the presence of many competing degrees of freedom (e.g. orbital, lattice, electronic, spin), and the

absence of a dominant energy scale, low-energy dynamics, particularly at THz (or far-infrared) frequencies, frequently reveal the interplay among these different degrees of freedom [10]. In THz studies, a reliable extraction of the temperature-dependent complex conductivity (or equivalently, refractive index) of the thin film depends critically on the complex refractive index of the underlying LAO substrate, at every temperature. Moreover, since thin-film growth invariably involves annealing, the effects of annealing on the optical properties of LAO must also be taken into account. Furthermore, it is well known that domains are present in LAO substrates, but their effect on the optical properties of LAO is not known. As far as we know, no systematic temperature or annealing-dependent studies have been carried out on LAO at THz frequencies. Our work fills this gap in knowledge, enabling future researchers to use the temperature-dependent refractive index of LAO to characterize their thin films more accurately. In this chapter, we report the temperature-dependent (10 K — 300 K) dielectric response of LAO by terahertz time-domain spectroscopy (THz-TDS) from 0.2 THz — 3 THz. After annealing, strong absorption peaks appear in $k(\omega)$, with peak positions shifting to higher frequencies with increasing temperature.

3.2 Experiment and data analysis

Our investigated samples are single crystals of (100) LAO: a $10 \times 10 \times 1 \text{ mm}^3$ piece from CrysTec GmbH (Berlin, Germany), and a $10 \times 10 \times 0.5 \text{ mm}^3$ piece from SWI (Hsinchu, Taiwan). Since both samples give the similar results, we only show data from the CrysTec sample. The dielectric response of LAO was measured by a commercial THz-TDS system (TeraView Spectra 3000). From THz-TDS, we can directly obtain

material dielectric parameters [11-16] like complex refractive index $\tilde{n}(\omega) = n(\omega) + ik(\omega)$, optical conductivity $\tilde{\sigma}(\omega) = \sigma_1(\omega) + i\sigma_2(\omega)$ and dielectric function $\tilde{\epsilon}(\omega) = \epsilon_1(\omega) + i\epsilon_2(\omega)$.

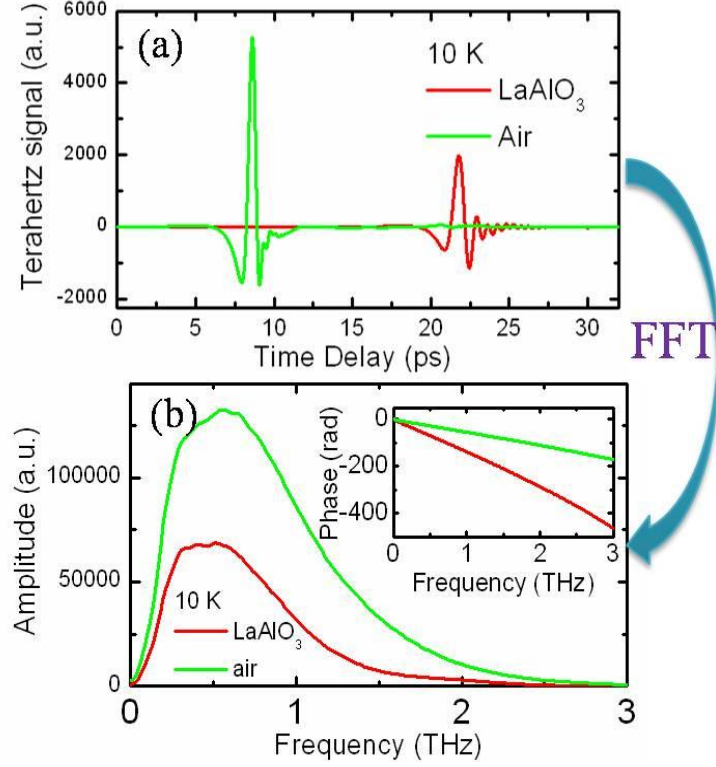


Figure 3.1 (a) Time-domain terahertz signal from sample LAO (without annealing) and air reference at 10 K. (b) Amplitude and phase spectra in the frequency domain from the FFT of (a).

The time-domain electric fields of a THz pulse transmitted through the LAO sample ($\tilde{E}_s(t)$), as well as through air reference ($\tilde{E}_r(t)$) are shown in Figure 3.1(a). The THz wave form was attenuated and delayed after passing through LAO sample. Fast Fourier transform (FFT) yields the amplitude and phase at different spectra components of the THz electromagnetic wave, as shown in Figure 3.1(b). Without invoking Kramers-Kronig relations, the complex refractive index $\tilde{n}(\omega)$ can be obtained by

numerically solving the equation [17]:

$$\tilde{T}(\omega) = \frac{\tilde{E}_s(\omega)}{\tilde{E}_r(\omega)} = \frac{4\tilde{n}(\omega)}{(1 + \tilde{n}(\omega))^2} \exp[i\omega d(\tilde{n}(\omega) - 1)/c], \quad (2.4)$$

where $\tilde{T}(\omega)$, $\tilde{n}(\omega)$, d , c are complex transmittance, LAO complex refractive index, sample thickness and speed of light (in vacuum), respectively.

3.3 Results and discussion

The annealing effect can cause absorption peaks in the extinction coefficient $k(\omega)$ and sudden change in the refractive index $n(\omega)$ at certain frequencies. The absorption peak positions are temperature-dependent. Also, different LAO crystal orientations have different dielectric properties.

3.3.1 LAO as grown and after annealing process in 0° orientation

The refractive index $n(\omega)$ and extinction coefficient $k(\omega)$ of LAO (without annealing) at different temperatures are shown in Figure 3.2(a) and 3.2(b). $n(\omega)$ is temperature-dependent and increases monotonically with frequency. The values of $k(\omega)$ are very small, and no obvious absorption peaks appeared in our experimental frequency range. The extracted $n(\omega)$ and $k(\omega)$ are consistent with other reports [4, 18] at 300 K. Next, the LAO was annealed under the condition of 1000°C in vacuum for 3 hours. This annealing temperature makes sure the LAO had experienced the cubic-to-rhombohedral transition phase transition at $T_c \approx 850$ K. As the sample is cooled back down below T_c , it went back to the rhombohedral phase. Then, as THz-TDS data were taken at the same orientation as before, the extracted $n(\omega)$ now exhibits jumps at certain frequencies (Figure 3.2(c)), where it suddenly drops, then recovers slowly with frequency. Also,

several absorption peaks appear in $k(\omega)$ (Figure 3.2(d)). These absorption peaks are temperature-dependent — shifting to higher frequency with increasing temperature.

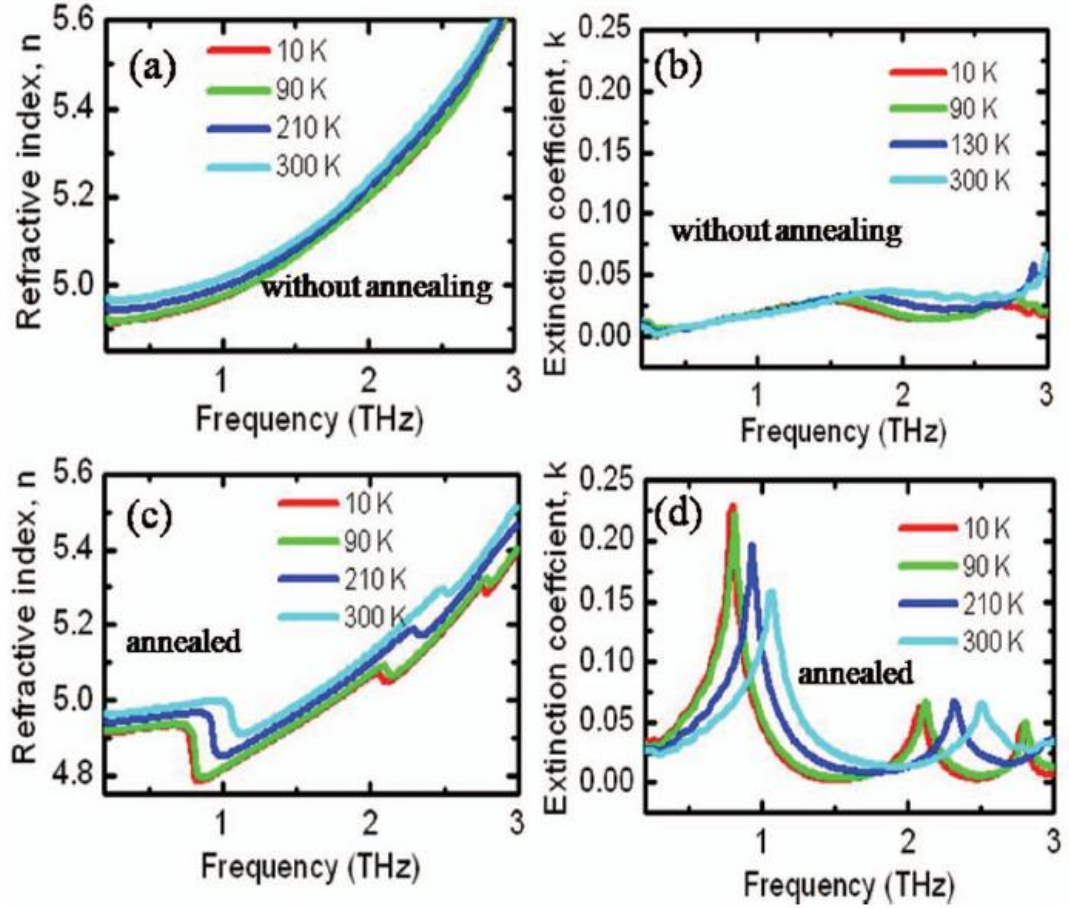


Figure 3.2 Extracted refractive index n and extinction coefficient k of LAO before and after annealing treatment at different temperatures. Before annealing (a), (b) and after annealing (c), (d).

We attribute the appearance of absorption peaks in $k(\omega)$ after annealing to a relocation of oxygen vacancies in the LAO crystal. Before annealing, below 730 K, the immobile oxygen vacancies form clusters and effectively pin the domain walls [3]. During the annealing of LAO at 1000°C, the self-diffusion coefficient of these oxygen vacancies increase significantly at high temperature [8]. As the oxygen vacancies diffuse

and relocate throughout the crystal, the effect of pinning will be reduced, resulting in the domain walls becoming more mobile, until they disappear.

3.3.1.1 Spectral weight transfer

The real part of optical conductivity $\sigma_1(\omega)$ can be obtained from the relationship $\sigma_1(\omega) = 2n(\omega)k(\omega)\omega\epsilon_0$. Figure 3.3 shows the spectrum of $\sigma_1(\omega)$ before and after annealing, at different temperatures. Before annealing, in the "as-is" sample, $\sigma_1(\omega)$ increases slightly with frequency, and does not show any sharp features. Upon annealing, however, temperature-dependent peaks develop in $\sigma_1(\omega)$. According to the f -sum rule for $\sigma_1(\omega)$ [19], the spectral weight, defined as the area under the conductivity spectrum $\int_0^\infty \sigma_1(\omega)d\omega$, is proportional to the ratio of the electronic density to the electronic mass $\frac{\pi Ne^2}{2m}$. This f -sum rule can be expressed rigorously as $\int_0^\infty \sigma_1(\omega)d\omega = \frac{\pi}{2} \sum_j \frac{(q_j)^2}{M_j}$ for any kind of excitation in the solid. Here q_j and M_j are the effective charge and mass of the j^{th} excitation, respectively. For phonon excitations, for example, q may not be equal to e , and more importantly M is much larger than m due to the heavy ionic mass [20]. Comparing the $\sigma_1(\omega)$ before and after annealing in Figure 3.3, we noticed that, after annealing, $\sigma_1(\omega)$ exhibits peaks only at some particular frequencies, and is almost zero away from these frequencies. This indicates the spectral weight is redistributed and transferred towards these frequencies after annealing. Annealing above the transition temperature T_c will usually relax the thermal strains and redistribute the oxygen defects, causing twin walls to appear elsewhere and in different orientations when the crystal is again cooled to below T_c [18].

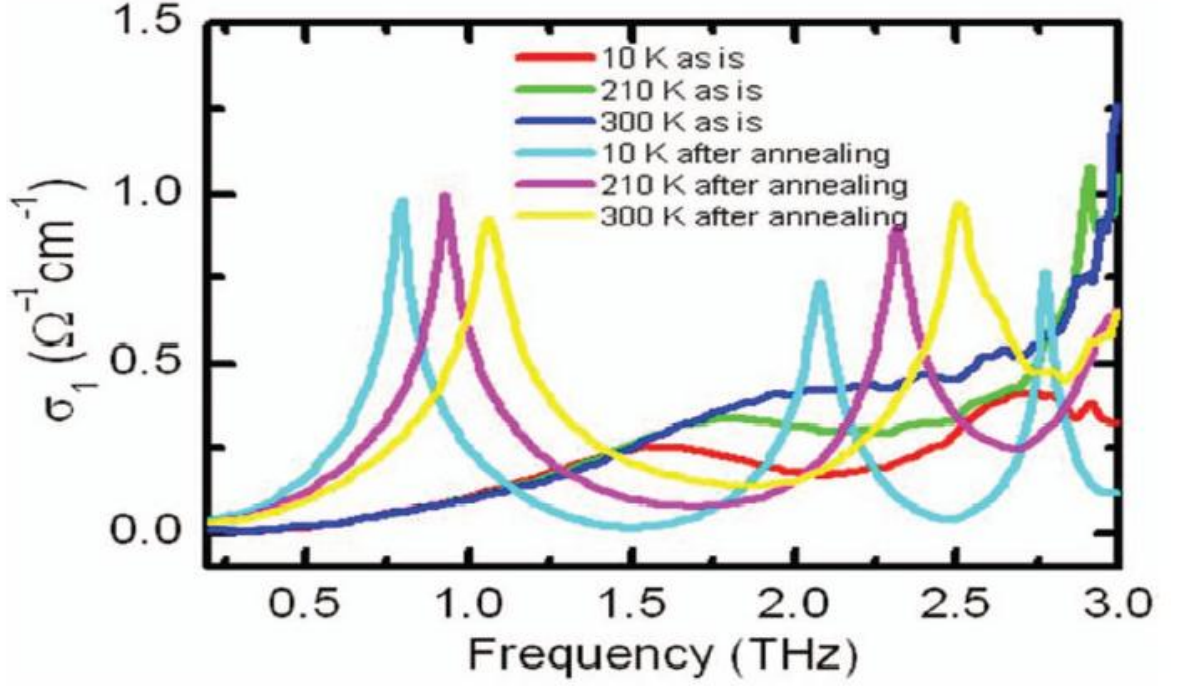


Figure 3.3 Real part conductivity of LAO before and after annealing at various temperatures.

3.3.1.2 Drude-Lorentz model fitting and discussion

In order to probe the origin of these temperature-dependent absorption peaks, we compute the complex dielectric function of annealed LAO from $n(\omega)$ and $k(\omega)$ by the relations: $\varepsilon_1(\omega) = n(\omega)^2 - k(\omega)^2$ and $\varepsilon_2(\omega) = 2n(\omega)k(\omega)$. The real and imaginary parts of dielectric function are simultaneously fitted with the Drude-Lorentz model [21, 22]. In this model, frequency-dependent dielectric function can be described by summing over various oscillators and a residual Drude contribution:

$$\tilde{\varepsilon}(\omega) = \varepsilon_\infty - \frac{\omega_p^2}{\omega^2 + i\Gamma_0\omega} + \sum_k \frac{A_k \omega_k^2}{\omega_k^2 - \omega^2 - i\Gamma_k\omega} \quad (2.19)$$

The first term ε_∞ is the high-frequency dielectric constant $\varepsilon_\infty = 4.82$ [6, 23]; the second term is the Drude term, which describes the response of the unbound (free) charge

carriers; ω_p and Γ_0 are the plasma frequency and scattering rate of free electrons, respectively. The last term describes a collection of Lorentz oscillators, where A_k, ω_k, Γ_k are the oscillator strength, oscillator resonance frequency and oscillator damping constant (spectral width) of the k^{th} oscillator, respectively.

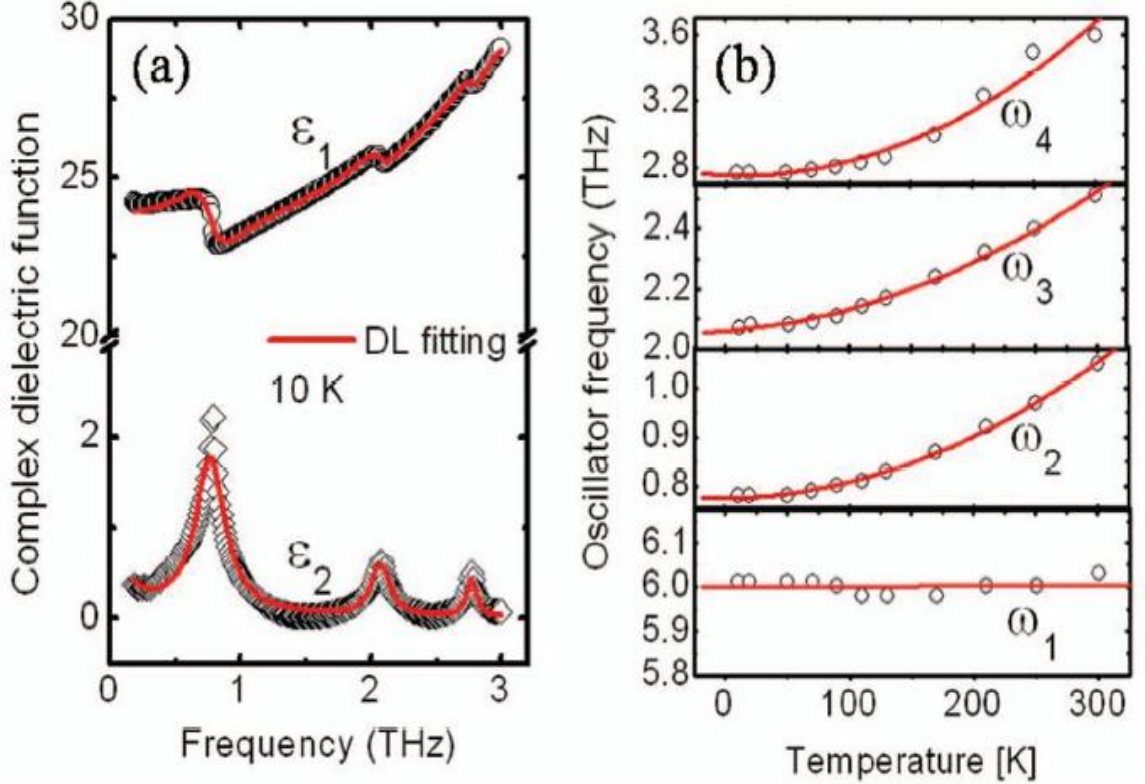


Figure 3.4 (a) Real and imaginary parts of dielectric function of LAO and the Drude-Lorentz model fitting. (b) Oscillator frequencies evolve with temperature, red lines are linear fitting for ω_1 and quadratic fitting for ω_2, ω_3 and ω_4 .

To obtain a good fit, we used four Lorentz oscillators. Figure 3.4(a) shows the real and imaginary parts of $\epsilon(\omega)$, and the corresponding Drude-Lorentz model fitting, where, for the sake of clarity, only the 10 K data and fitting are presented. Generally, THz absorption is attributed to the interactions of THz field with the fundamental lattice

vibrations in the crystal. The optical modes of Brillouin zone center associated with the first-order dipole moment give rise to intrinsic absorption due to lattice vibrations. Among the four resonances, the strongest absorption peak ω_1 is located at ~ 6 THz with a temperature-independent peak position. This strong ($A_1 \sim 18$) 6 THz peak corresponds to the main infrared (IR) triplet mode at 167 cm^{-1} in the undistorted perovskite, which transforms into the $168 \text{ cm}^{-1} A_{2u}$ IR singlet and $179 \text{ cm}^{-1} E_u$ IR doublet upon undergoing rhombohedral distortion [6]. The other three resonances ($\omega_2 \sim 1.0$ THz, $\omega_3 \sim 2.5$ THz, $\omega_4 \sim 3.5$ THz at 300 K) are much weaker than ω_1 , with temperature-dependent peak positions — shifting to higher frequency with increasing temperature, as shown in Figure 3.4(b). It has been confirmed experimentally and theoretically that Raman modes in LAO [5, 6] appear at ~ 1 THz and ~ 3.7 THz. The observation of the 1 THz (ω_2) and 3.5 THz (ω_4) modes in our data showed that, upon annealing, these Raman modes have acquired IR character as well. This is not surprising, as lattice distortion induced at high temperatures ($\sim 500^\circ\text{C}$) may have caused an asymmetry in the lattice structure that results in the appearance of absorption peaks at these previously Raman-active frequencies [8]. Our temperature-dependent ω_3 has not been reported before — it possibly originates from multiple phonon processes [14].

We now discuss the phonon stiffening with increasing temperature. Normally, the frequency change of lattice modes is related to the rate of change in volume V of the crystal via $\frac{\Delta f}{f} = -\gamma \frac{\Delta V}{V}$, where γ is an average Grüneisen constant [24]. In most materials, $\gamma > 0$, so phonons soften upon thermal expansion, which is attributed to the presence anharmonic components in interatomic potentials. This deviation from harmonicity causes scattering between the phonon. However, in vanadium metal, the

phonons stiffen with increasing temperature [24]. This was attributed to coupling between phonons and the electron bandstructure. For LAO crystal, the AlO_6 structural unit (AlO_6) can rotate as a rigid unit, thus breaking the symmetry of a structure of packed octahedra. Also, the corner oxygen atoms of AlO_6 are not shared by other octahedra, thus having more freedom to be involved in the reorientations [25]. These features may be responsible for the phonon stiffening with increasing temperature in the annealed LAO crystal. The low energy vibrational modes in ZrW_2O_8 and HfMo_2O_8 , with similar local structure as LAO, also show a stiffening with increasing temperature. To fully elucidate the phonon frequencies stiffening with increasing temperature, additional theoretical calculations are required [26].

3.3.2 LAO as grown and after annealing process in 90° orientation

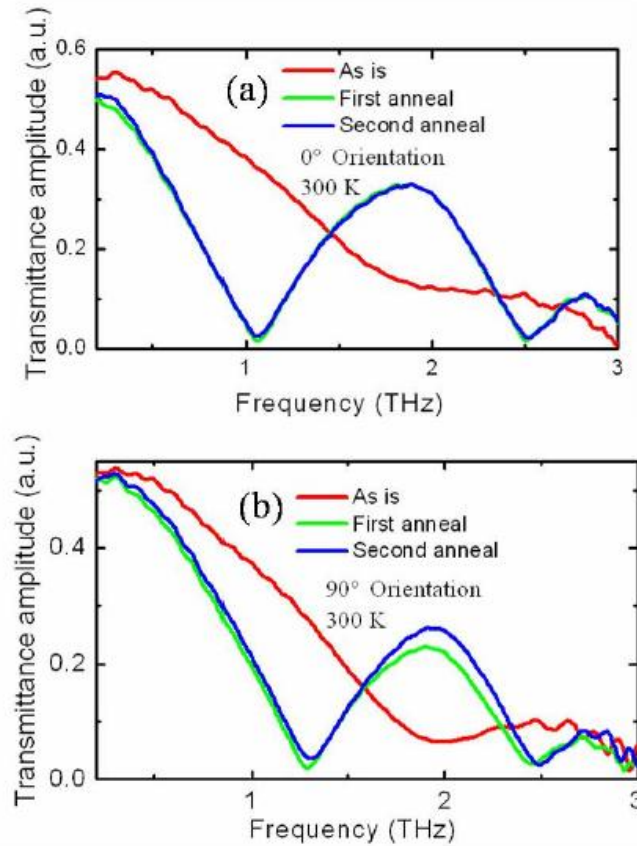


Figure 3.5 Transmittance amplitude at (a) 0° and (b) 90° LaAlO_3 orientation.

We also measured the transmission spectra after rotating sample by 90° in the plane parallel to LAO (100) surface. The transmission spectra before rotation (0°) and after rotation (90°) are shown in Figure 3.5. In the 0° orientation, annealing causes the appearance of several absorption peaks in the transmission spectra (Figure 3.5(a)), and these peaks can also be seen in Figure 3.2(d). Subsequent annealing treatment does not change the spectra.

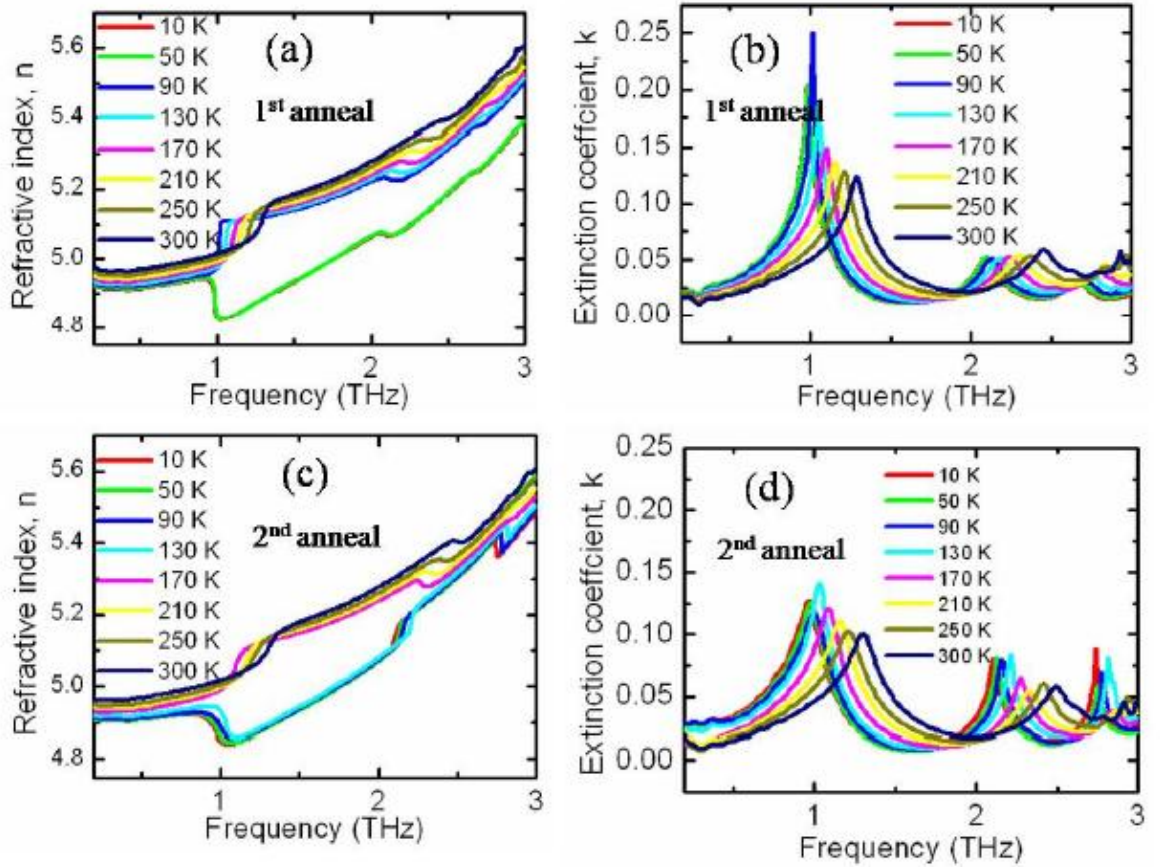


Figure 3.6 Comparison of refractive index n and extinction coefficient k after the first and the second annealing treatments in 90° orientation. First annealing (a), (b) and second annealing (c), (d).

However, in the 90° orientation, we observed differences after the first and second

annealing (Figure 3.5(b)). Surprisingly, the transmittance amplitude after the second annealing is slightly higher than the first. These differences were also reflected in the complex refractive index as shown in Figure 3.6. The refractive index behaviors between the two annealing treatments are not exactly the same like the 0° orientation. Based on our experimental results, we attribute the annealing effects on optical properties to the redistribution of LAO domains. We suggest that, for optical measurement of thin films grown on LAO substrate (eg. THz-TDS), the reference substrate should undergo the same annealing conditions as the sample growing process. Also, the orientation, temperature and frequency dependent of complex refractive index should be taken into account when extracting the sample's optical parameters.

3.4 Conclusion

Temperature-dependent THz dielectric response of as-is and annealed LAO have been studied using THz-TDS from 0.2 THz — 3 THz. Annealing greatly affects its optical properties. The appearance of the absorption peaks in $k(\omega)$ upon annealing is attributed to the diffusion and relocation of oxygen vacancies — these disordered oxygen vacancies reduce the pinning effects on the domain walls in the LAO crystal. The change of $\sigma_1(\omega)$ from featureless, to peaks occurring at certain frequencies, is attributed to spectral weight transfer. Most of this work has been published in AIP Advances **2**, 012120 (2012).

References

- [1] R. J. Zeches, M. D. Rossell, J. X. Zhang, A. J. Hatt, Q. He, C. H. Yang, A. Kumar, C. H. Wang, A. Melville, C. Adamo, G. Sheng, Y. H. Chu, J. F. Ihlefeld, R. Erni, C. Ederer, V. Gopalan, L. Q. Chen, D. G. Schlom, N. A. Spaldin, L. W. Martin, and R. Ramesh, *Science* **326**, 977 (2009).
- [2] S. A. Hayward, S. A. T. Redfern, and E. K. H. Salje, *J. Phys.: Condens. Matter* **14**, 10131 (2002).
- [3] S. A. Hayward, F. D. Morrison, S. A. T. Redfern, E. K. H. Salje, J. F. Scott, K. S. Knight, S. Tarantino, A. M. Glazer, V. Shuvaeva, P. Daniel, M. Zhang, and M. A. Carpenter, *Phys. Rev. B* **72**, 054110 (2005).
- [4] Z. M. Zhang, B. I. Choi, M. I. Flik, and A. C. Anderson, *J. Opt. Soc. Am. B* **11**, 2252 (1994).
- [5] V. G. Sathe, and A. Dubey, *J. Phys.: Condens. Matter* **19**, 382201 (2007).
- [6] P. Delugas, V. Fiorentini, and A. Filippetti, *Phys. Rev. B* **71**, 134302 (2005).
- [7] C. Zuccaro, M. Winter, N. Klein, and K. Urban, *J. Appl. Phys.* **82**, 5695 (1997).
- [8] K. Nomura, S. Okami, X. J. Xie, M. Mizuno, K. Fukunaga, and Y. Ohki, *Jpn. J. Appl. Phys.* **50**, 021502 (2011).
- [9] D. Grischkowsky, and S. Keiding, *Appl. Phys. Lett.* **57**, 1055 (1990).
- [10] R. D. Averitt, and A. J. Taylor, *J. Phys. Condens. Matter* **14**, R1357 (2002).
- [11] J. Shan, F. Wang, E. Knoesel, M. Bonn, and T. F. Heinz, *Phys. Rev. Lett.* **90**, 247401 (2003).
- [12] K. R. Mavani, M. Nagai, D. S. Rana, H. Yada, I. Kawayama, M. Tonouchi, and K. Tanaka, *Appl. Phys. Lett.* **93**, 231908 (2008).
- [13] J. B. Baxter, and C. A. Schmuttenmaer, *Phys. Rev. B* **80**, 235205 (2009).
- [14] J. G. Han, B. K. Woo, W. Chen, M. Sang, X. C. Lu, and W. L. Zhang, *J. Phys. Chem. C* **112**, 17512 (2008).
- [15] J. L. Tomaino, A. D. Jameson, J. W. Kevek, M. J. Paul, A. M. van der Zande, R. A. Barton, P. L. McEuen, E. D. Minot, and Y. S. Lee, *Opt. Express* **19**, 141 (2011).
- [16] T. R. Tsai, S. J. Chen, C. F. Chang, S. H. Hsu, T. Y. Lin, and C. C. Chi, *Optics Express* **14**, 4898 (2006).
- [17] L. Duvillaret, F. Garet, and J. L. Coutaz, *IEEE J. Sel. Top. Quantum Electron.* **2**, 739 (1996).
- [18] S. Bueble, K. Knorr, E. Brecht, and W. W. Schmahl, *Surf. Sci.* **400**, 345 (1998).
- [19] D. N. Basov, R. D. Averitt, D. van der Marel, M. Dressel, and K. Haule, *Rev. Mod. Phys.* **83**, 471 (2011).
- [20] M. Dressel, and G. Grüner, (Cambridge University Press, Cambridge, 2002).
- [21] A. B. Kuzmenko, *Rev. Sci. Instrum.* **76**, 083108 (2005).
- [22] D. Talbayev, A. D. LaForge, S. A. Trugman, N. Hur, A. J. Taylor, R. D. Averitt, and D. N. Basov, *Phys. Rev. Lett.* **101**, 247601 (2008).
- [23] R. Vali, *Comput. Mater. Sci.* **44**, 779 (2008).
- [24] O. Delaire, M. Kresch, J. A. Munoz, M. S. Lucas, J. Y. Y. Lin, and B. Fultz, *Phys. Rev. B* **77**, 214112 (2008).
- [25] B. Fultz, *Prog. Mater. Sci.* **55**, 247 (2010).
- [26] X. Zou, M. He, D. Springer, D. Lee, S. K. Nair, S. A. Cheong, T. Wu, C. Panagopoulos, D. Talbayev, and E. E. M. Chia, *AIP Advances* **2**, 012120 (2012).

Chapter 4. Carrier dynamics of graphene probed by optical pump-probe technique

In this chapter, we will discuss the ultrafast pump-probe results of bilayer graphene and FeCl₃-intercalated bilayer graphene. Electronic band structures of these two materials are calculated by density functional theory. We find that FeCl₃-intercalation can introduce additional bands in the electronic band structure and result in differences in the pump-probe data.

4.1 Introduction

Graphene was believed to be unstable and presumed not to exist in the free state, until free-standing graphene was unexpectedly found [1]. Graphene is a basic building block for all other graphitic materials, such as fullerenes (0D), nanotubes (1D) or graphite (3D), as shown in Figure 4.1 [2]. Graphene is a two-dimensional plane of carbon atoms arranged on a honeycomb structure, and has a linear energy dispersion of the conduction and valence bands intersecting at the Dirac point. The linear energy dispersion gives rise to the massless relativistic behavior of quasiparticles. It has attracted intense research interest due to the interesting physics and potential applications. For example, the extremely high carrier mobility ($10^4 \text{ cm}^2\text{V}^{-1}\text{s}^{-1}$) [3] at room temperature of graphene is ten times higher than that in silicon. Also, the charge carrier density can be easily controlled by applying a gate voltage. These advantages, which are superior to those of conventional semiconductors, may enable graphene to be a key component of future-generation electronics [4, 5].

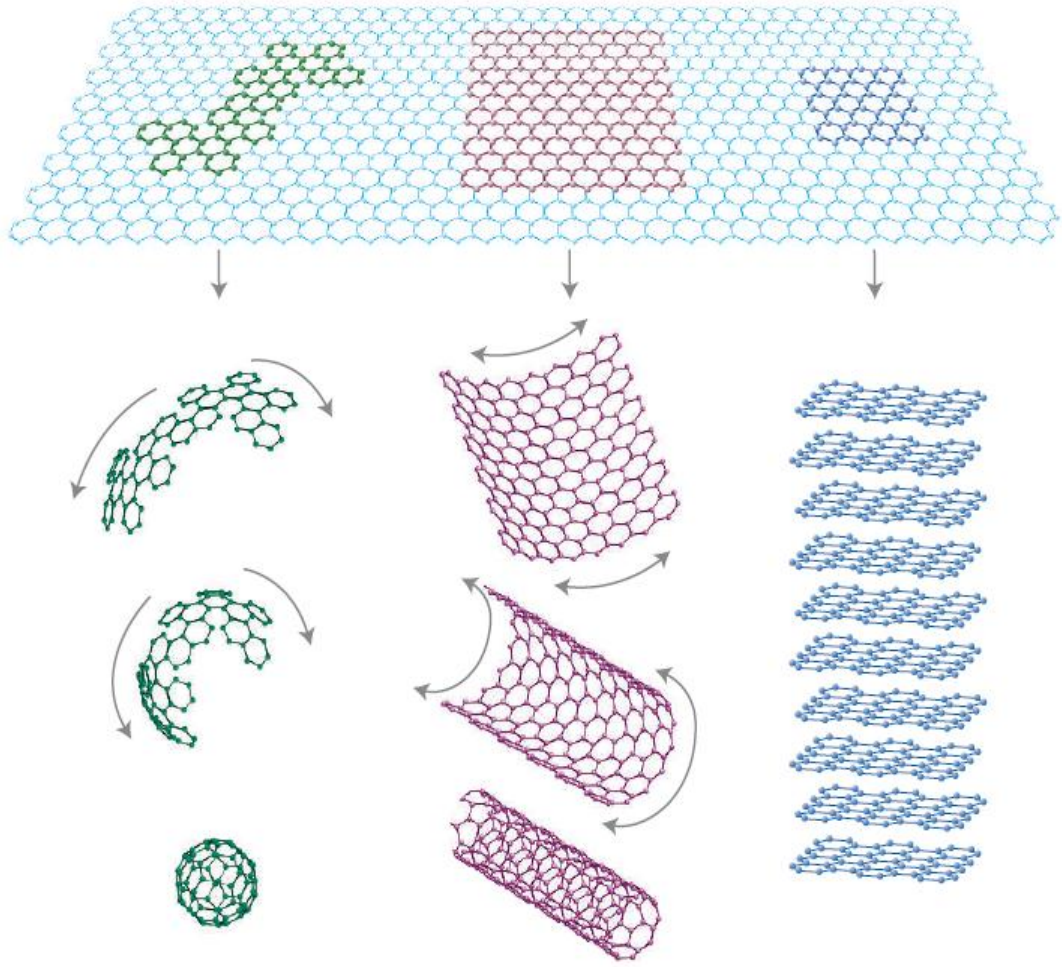


Figure 4.1 Graphene is a basic 2D building block for all other carbon materials. It can be wrapped up into 0D buckyballs, rolled into 1D nanotubes or stacked into 3D graphite.

Figure taken from Ref. [2].

Bilayer graphene (BLG) is composed of two single layer graphene (SLG), with usually an AB-stacking order, plus a coupling between the two layers. Reference [6] has described the BLG stacking order: “In the most common (Bernal) stacking, adjacent layers are shifted by one atomic spacing, so that B atoms of layer 2 (B2) sit directly on top of A atoms of layer 1 (A1) and B1 and A2 atoms are in the centre of the hexagons of the opposing layer”. Figure 4.2 shows the structure of BLG with unit vectors \vec{a}_1 , \vec{a}_2 and the relevant hopping parameters in the system. In the presence of interlayer coupling, the

linear energy dispersion near the K point in SLG is converted to a parabolic one for the BLG with an effective mass of $\sim 0.03m_e$ [7-9]. The band gap between valence and conduction bands can be tuned by applying an electric field perpendicular to the sample. The difference between SLG (linear dispersion) and BLG (quadratic dispersion) has prompted work to explore and contrast various dielectric properties in the two systems [6]. The tunability of the bandgap via an electric field makes BLG a promising material for future nanoelectronic and nanophotonic devices [10].

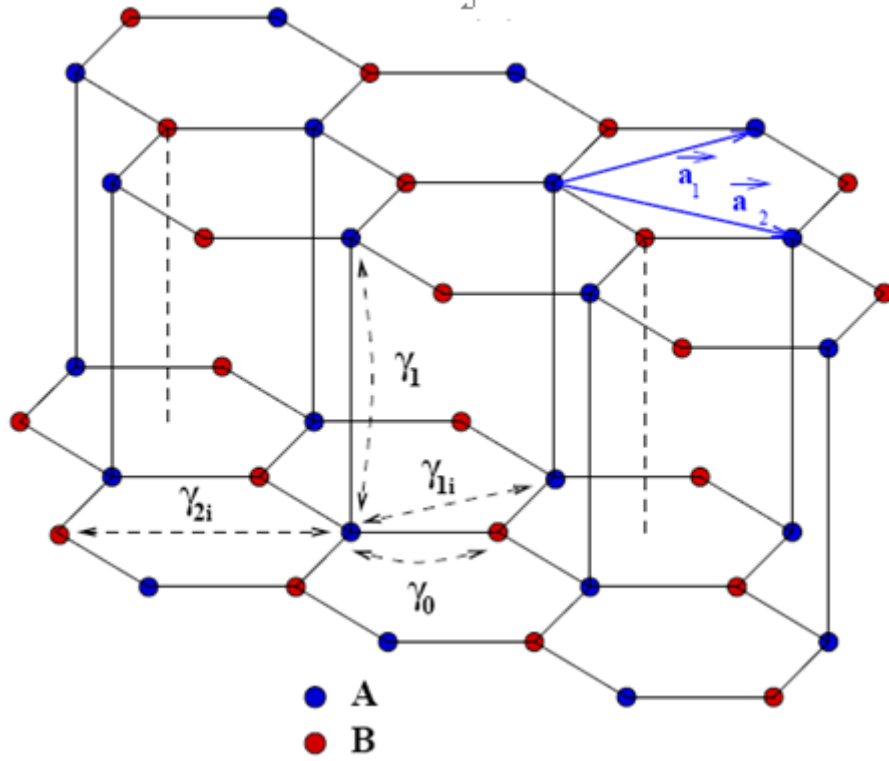


Figure 4.2 Structure of bilayer graphene and hopping parameters nearest neighbour in-plane coupling energy (γ_0), nearest neighbor inter-plane coupling energy (γ_1), next-nearest neighbor in-plane coupling energy (γ_{1i}) and next-to-next nearest neighbor in-plane coupling energy (γ_{2i}). Figure taken from Ref. [7].

Similar to the SLG, small scale high-quality BLG can be achieved experimentally by mechanical exfoliation of graphite onto SiO₂ substrates. To obtain large-scale BLG, epitaxial growth on SiC substrate and CVD (chemical vapor deposition) methods are often used. However, the quality is not as good as the mechanical exfoliated sample, and decoupling of the graphene layer is often observed [11-13].

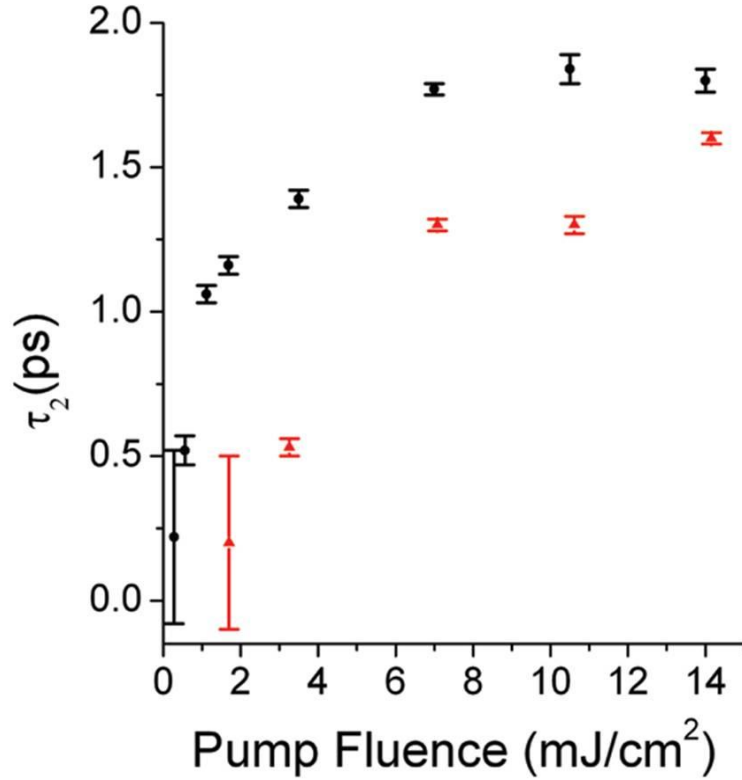


Figure 4.3 Value of τ_2 as a function of pump fluence, the red triangles are another position with few graphene layers on the sample. Figure taken from Ref. [18].

The first measurements of ultrafast carrier dynamics in epitaxial graphene reveal two distinct time scales, which was attributed to the relaxation of nonequilibrium photoexcited quasiparticles [14]. Time-resolved terahertz spectroscopy on graphite [15], revealed a strong coupling between electrons and the lattice (~500 fs), and subsequent

cooling of hot phonons (~ 7 ps). All optical pump-probe spectroscopy of freestanding thin graphite films revealed a fast intraband carrier equilibration (~ 20 - 30 fs), and a subsequent relaxation of the hot carriers (via emission of optical phonons) with a timescale of ~ 200 fs [16, 17].

There have been many subsequent reports on the ultrafast dynamics of charge carriers in graphene, using optical pump-probe [18, 19] and THz techniques [20, 21]. Most of these experiments found a fast relaxation process (several hundred fs) followed by a slower relaxation process (a few ps). The fast relaxation process is assigned to the coupling between the electrons and optical phonons in graphene [22, 23], while the slow relaxation process assignment is more complicated. In the literature, the slow component has been attributed to minority carrier recombination [21], coupling between electrons and acoustic phonons [24] and hot phonon effect [18]. In a fluence-dependent study, the slow relaxation time reaches a limiting value at high pump intensities, then the slow relaxation time is assigned to the decay of the optical phonons [18]. The slow relaxation time initially increases with pump fluence, and levels off at a certain pump fluence, as shown in Figure 4.3. The limiting value of the slow relaxation time at high pump intensity reflects the relaxation time for the optical phonon modes [18].

The electronic properties of graphene, via a change in its structure, can be tuned by intercalation (e.g. nitrogen or boron [25,26]), surface adsorption of metal atoms or molecules, or using different substrates [27]. Such ability to control the properties of graphene can pave the way for novel photonics and electronics [28]. Ultrafast measurements and theoretical calculations have been applied to study the optical and electrical properties of graphite and graphene in recent years [14-20, 22, 24, 29]. The

dynamics of electrons and holes after photoexcitation in graphene occurs on an ultrashort time scale (a few ps).

Although many ultrafast studies have been done on graphite, graphene and multilayer graphene, ultrafast pump-probe measurement of FeCl₃-intercalated bilayer graphene (FeCl₃-G, FeCl₃ layer sandwiched by two graphene layers) has not been reported yet. Chemical doping resulting from adsorption or intercalation may well become an important aspect of future graphene research. For example, an induced potential difference between surface and interior layers by adsorption or intercalation with Br₂ and I₂ vapors can open a band gap [26]. Also, graphite intercalated with FeCl₃ can cause the material to be hole-doped [30, 31]. Superconductivity was discovered when graphite was intercalated with alkali metals [32] and rare earth materials [33]. Thus, the understanding of electron dynamics in graphene intercalated with different materials will be important for future graphene-based device applications.

In this chapter, we studied the ultrafast degenerate pump-probe measurement of the FeCl₃-G and BLG deposited on the SiO₂/Si substrate from 10 K to room temperature. Comparing the results with BLG which has a fast rise time (~100 fs) and two subsequent relaxation processes, FeCl₃-G exhibits a slower rise time (~0.2 – 0.8 ps) and only one subsequent relaxation process. Both the rise and relaxation times are temperature-dependent and decrease with increasing lattice temperature from 10 K to 300 K. This chapter is outlined as follows:

- (a). Sample preparation and Raman characterization.
- (b). Pump-probe results of FeCl₃-G and BLG samples.
- (c). Electronic band structure calculation and discussions.

(d). Pump fluence effect on the relaxation times of FeCl₃-G and BLG samples.

4.2 Sample preparation and Raman characterization

The bilayer graphene sheets were fabricated on polycrystalline Cu foils by low pressure CVD process [34] using a mixture of methane and hydrogen. The number of graphene layers was confirmed by contrast spectra [35, 36]. Reference [37] describes the sample preparation process (the FeCl₃-FLGIC is the same as FeCl₃-G in this thesis): “The two-zone vapor transport method was used for fabricating FeCl₃-FLGIC. The reaction took place inside a vessel constructed from a glass tube. The graphene samples and anhydrous FeCl₃ powder (approximately 0.03 g) were separated by around 6 cm. The tube was pumped to 10⁻² torr and sealed. In our experiment, the two-zone method was processed using a single furnace instead of the traditional two-furnace technique. The temperature distribution in the furnace was measured by a thermocouple before the experiment. The reaction vessel was placed in an appropriate position in the furnace to achieve the desired two-zone temperatures (360 °C for graphene samples and 310 °C for anhydrous FeCl₃ powder). The heating rate was set at 10 °C min⁻¹, and the vessel was kept for 10 h at the set temperature. Finally the furnace was cooled at a rate of 10 °C min⁻¹ to room temperature.” (The BLG and FeCl₃ intercalated BLG samples were grown by Dr. Luo Zhiqiang and Zhan Da in Prof. Shen Zexiang’s group).

Reference [37] describes the Raman spectroscopy measurement:” Raman spectra were recorded by a WITEC CRM200 system with a spectral resolution of 1 cm⁻¹. The excitation laser was 532 nm (2.33 eV) and the laser power at sample was kept below 0.5 mW to avoid laser heating effect. A 100 × objective lens with a numerical aperture of

0.95 was used.” Figure 4.4 shows the Raman spectra of BLG and FeCl₃-G at room temperature. The CVD-based BLG normally does not show AB stacking order, but is misoriented. Such misoriented BLG presents a single Lorentzian 2D peak [38] with a FWHM (full wave half maximum) $\sim 43\text{ cm}^{-1}$.

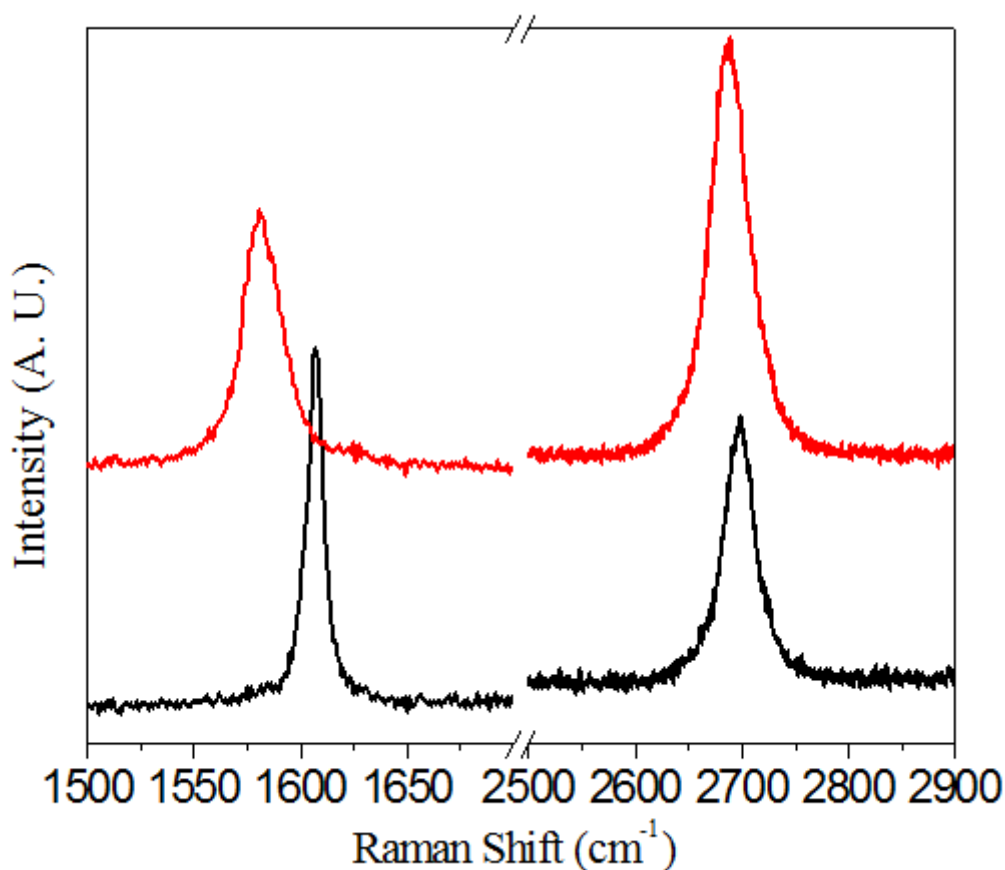


Figure 4.4 Raman spectra of CVD-based BLG (red) and FeCl₃-G (black).[Raman spectra was taken by Dr. Luo Zhiqiang].

The number of layers of such misoriented graphene can be measured by contrast spectra [35, 36], and it is found that the BLG covered more than 80% of the whole graphene region (the remainder 20% is mainly dominated by single layer and trilayer graphene). After the intercalation process, it is estimated that more than 60% area of the

graphene regions has been successfully intercalated by FeCl_3 according to the strong blue shift of the G peak position ($\sim 1612 \text{ cm}^{-1}$) of these area. This is because of the electrons transferred from each graphene layer to intercalated FeCl_3 give rise to the strong hole doping effect of each graphene layer [30, 31]. The other regions of BLG only show a tiny blue shift of the G peak position ($\sim 1590 \text{ cm}^{-1}$) compared to the intercalated region, and this tiny blue shift effect of G peak is caused by the normal doping effect after vacuum annealing [39]. The much sharper G peak of FeCl_3 -G compared with pristine BLG is due to the nonadiabatic removal of the Kohn anomaly [40-42]. In addition to the change of G peak feature, it is found that the FeCl_3 -G shows an even sharper single Lorentzian 2D peak (FWHM is about 35 cm^{-1}) compared with the precursor misoriented BLG. This indicates that the interaction between graphene layers is very small because of the intercalation of FeCl_3 .

4.3 Pump-probe results of FeCl_3 -G and BLG samples

Our degenerate pump-probe setup [43] uses a Ti:sapphire mode-locked laser with 80 MHz pulse repetition rate, generating 800 nm, 40 fs pulses. The pump beam was focused to a spot size of $60 \text{ }\mu\text{m}$ on the sample surface to generate photoexcited carriers, while the weaker $25 \text{ }\mu\text{m}$ -diameter probe beam was used to measure the change in the reflectivity ($\Delta R/R$) as a function of the probe delay time relative to the pump. The intensity ratio of the pump pulse (0.075 nJ/pulse) and probe pulse is ~ 30 , and polarization between the pump (P polarized) and probe (S polarized) is orthogonal to minimize detection of scattered pump. The pump beam was modulated at a frequency of 1 MHz using an acoustic-optical modulator (AOM), and the photoinduced change in the reflected probe

intensity at different delay times between the pump and probe pulses was measured with a lock-in amplifier.

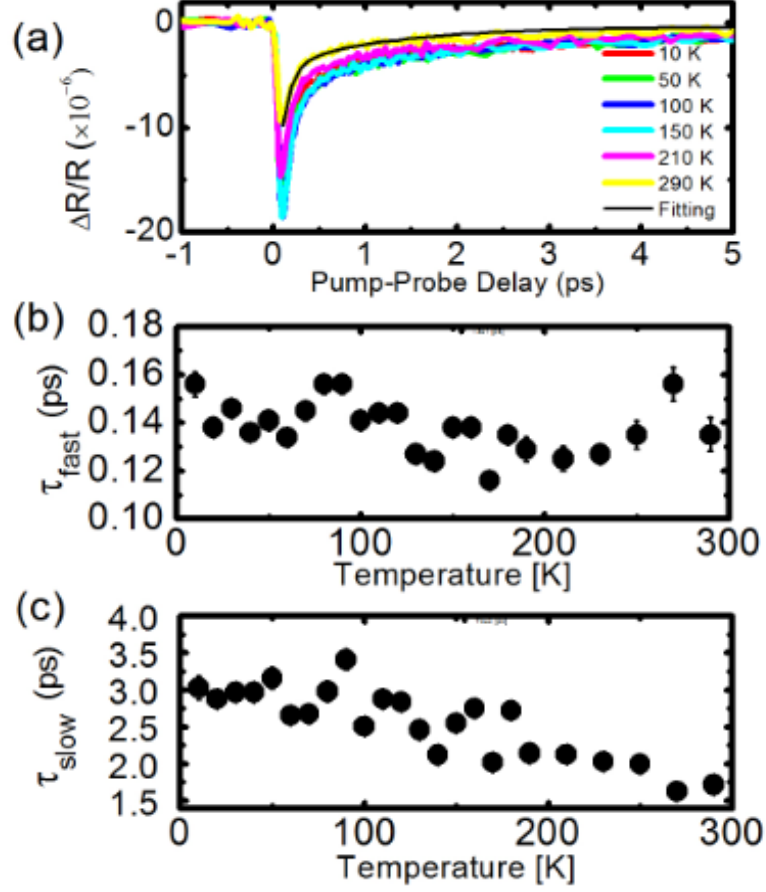


Figure 4.5 (a) Differential reflectivity $\Delta R/R$ versus pump-probe delay of BLG at different temperatures. Black line is a two-exponential fitting to the 290 K data. (b) τ_{fast} and (c) τ_{slow} evolve with temperature.

The differential reflectivity $\Delta R/R$ of the BLG sample at different temperatures are presented in Figure 4.5(a). The sign of $\Delta R/R$ is negative with a rising time of the order of the pulse width and the recovery of $\Delta R/R$ exhibits two distinct time scales: a fast decay time τ_{fast} and a slower one τ_{slow} . Our data are fitted using a bi-exponentially decaying function, $\Delta R/R = A_{fast} \exp(-t/\tau_{fast}) + A_{slow} \exp(-t/\tau_{slow})$. The time scales of

τ_{fast} (< 160 fs) and τ_{slow} ($1.5 - 3.4$ ps) are consistent with those of other reports [15-17, 19, 20]. The processes of the relaxation can be explained by using optical phonon emission and optical phonon-acoustic phonon coupling.

The pump pulse creates non-equilibrium free electrons and holes in the conduction and valence bands, respectively. Carrier-carrier scattering thermalize the carriers into a Fermi-Dirac distribution with a temperature higher than the lattice temperature [44]. This initial thermalization occurs on a timescale of $20 - 30$ fs [16] and is beyond our experimental resolution. After thermalization, coupling between hot electrons and optical phonons cools the electrons on a timescale τ_{fast} observed in Figure 4.5(b). This is consistent with the timescale in graphite, when most of the photoexcited electron energy is transferred to the optical phonons during the first 200 fs [16]. The rough temperature-independence of the electron-phonon relaxation time τ_{fast} is consistent with the data seen in metals such as Ag and Au [45]. Subsequently, the optical phonons transfer their energies to acoustic phonons via optical-acoustic phonon coupling, which accounts for the slow process ($\tau_{slow} \sim \text{few ps}$) shown in Figure 4.5(c). Eventually, the photoexcited electrons reach thermal equilibrium with the lattice.

Figure 4.6(a) shows $\Delta R / R$ versus pump-probe time delay in the $\text{FeCl}_3\text{-G}$ sample at different temperatures. The rise time of the signal in $\text{FeCl}_3\text{-G}$ ($0.2 - 0.8$ ps) is much longer than that in BLG (~ 100 fs) and decreases with increasing lattice temperature, as shown in the inset of Figure 4.6(a). The fast relaxation component found in the BLG sample disappears, leaving only the slower one in $\text{FeCl}_3\text{-G}$. The relaxation process can be fitted using a single-exponential decay function: $\Delta R / R = A_{slow} \exp(-t / \tau_{slow})$. Figure 4.6(b) shows that the relaxation time τ_{slow} decreases with increasing lattice temperature,

similar to BLG. However, the values of τ_{slow} in FeCl₃-G are larger than in BLG. The difference in pump-probe data of BLG and FeCl₃-G originates from the difference in the electronic band structures.

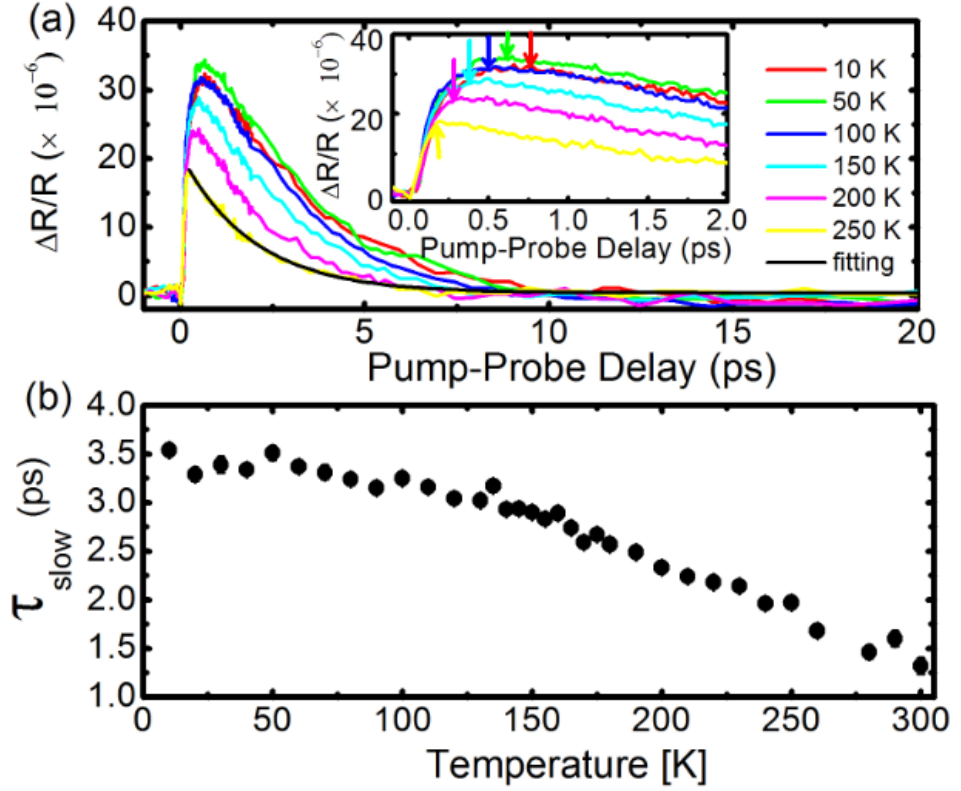


Figure 4.6 (a) Differential reflectivity $\Delta R/R$ versus pump-probe delay of FeCl₃-G at different temperatures. Black line is a one-exponential fitting to the 250 K data. Inset: region expanded near the peak position. (b) Temperature dependence of the single relaxation time τ_{slow} . Arrows show the peaks of the signals.

4.4 Electronic band structure calculation and discussions

Reference [37] describes the electronic band structure calculation method: “A supercell with lattice constants $a = 12.12 \text{ \AA}$ and $c = 9.370 \text{ \AA}$ was constructed, where the

layered FeCl_3 with 2×2 periods was taken as commensurate with the graphene of 5×5 unit cells, as shown in Figure 2. The DFT calculations based on the generalized gradient approximation (PBE-GGA)^[43] were performed using the plane-wave basis VASP code.^[44] The projector augmented wave (PAW) method is employed to describe the electron-ion interactions. A kinetic energy cutoff of 400 eV and k -points sampling with 0.05 \AA^{-1} separation in the Brillouin zone were used. The structure was optimized by a conjugate gradient algorithm with a force convergence criterion of 0.01 eV \AA^{-1} . Figure 4.7 shows the calculated electronic band structure of $\text{FeCl}_3\text{-G}$ (black line) and BLG (blue line). Note the presence of numerous horizontal bands in the $\text{FeCl}_3\text{-G}$ sample which originate from the d orbitals of iron. The Dirac point of the $\text{FeCl}_3\text{-G}$ is now located at $\sim +1 \text{ eV}$, demonstrating that FeCl_3 intercalated layer causes the material to become hole-doped.

The presence of a FeCl_3 layer sandwiched between two graphene layers can accept electrons from the top and bottom graphene layers, causing the graphene layers to become hole-doped, and modify the electronic transport properties in graphene. Moreover, the FeCl_3 intercalated layer introduces additional electronic states in the energy band structure which result in three effects in the pump probe results. First, these additional electronic states facilitate photoexcited electron transition between lower and higher energy levels with the assistance of optical phonons. Optical phonons can be emitted and *reabsorbed* by the carriers in the higher energy states, thus slowing down the energy relaxation of the photoexcited electrons, as shown in Figure 4.5(c) and Figure 4.6(b), that is, $\tau_{\text{slow}}(\text{FeCl}_3) > \tau_{\text{slow}}(\text{BLG})$. Second, optical phonon emission and reabsorption causes the number of photoexcited electrons to be built up slowly, resulting in a longer rise time, and causes the disappearance of the initial fast relaxation process

observed in BLG. This scenario is consistent with the case of sulfate-covered gold nanoparticles [46]. There the sulfate adsorbates act as a transient energy reservoir which results in the back and forth inelastic scattering of nonequilibrium electrons, causing a retardation of the internal thermalization time compared to bulk gold. Third, the opposite signs of the signals from the two samples is due to state-filling effects (in BLG) and induced probe absorption (in FeCl₃-G) dominating the absorption of the probe pulse. In the linear absorption range, probe differential reflectivity $\Delta R/R$ is proportional to pump fluence F , the relationship can be expressed as: $\Delta R/R \propto C \times \Delta\alpha \times F$, where C is a parameter depends on the interaction of probe with the excited sample, $\Delta\alpha$ is sample absorbance change. In the FeCl₃-G sample, electrons below the Fermi level in the valence band are excited to the horizontal bands located at energy ~ 1.5 eV higher by the pump photons. These photoexcited electrons in the horizontal bands can then be excited to higher energy states by absorbing the incoming probe photons (induced probe absorption), and therefore resulting in a larger probe absorption. Compare this to BLG, where the absorption of pump photons by the valence band electrons to the graphene conduction band decreases the density of empty states in the conduction band, thus resulting in a smaller probe absorption [47]. Our results show that, though the band structure of pure carbon graphene is dominated by the Dirac description, chemical modification (adsorption, substitution and intercalation) of graphene can modify the band structure and affect the carrier dynamics.

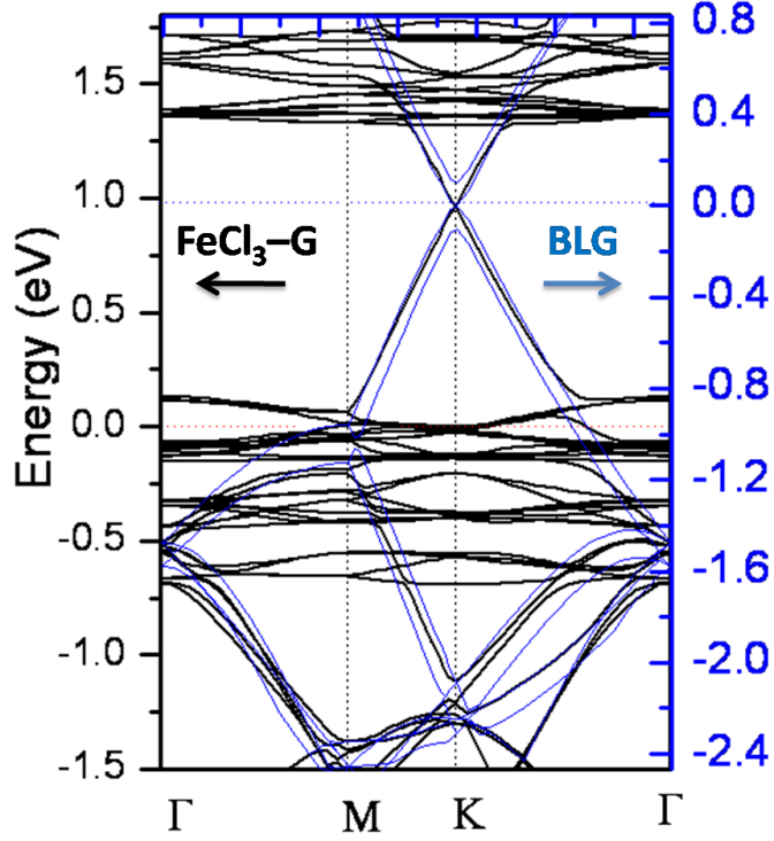


Figure 4.7 Calculated band structure of the $\text{FeCl}_3\text{-G}$ (black) and BLG (blue). The horizontal bands originate from d orbitals of iron and the Dirac point is located at $\sim +1$ eV after FeCl_3 intercalation. [Band structure calculated by Dr. Fan Xiaofeng]

4.5 Pump fluence effect on the relaxation times of $\text{FeCl}_3\text{-G}$ and BLG samples

We also examined the influence of photoexcited carrier density on the relaxation time of both BLG and $\text{FeCl}_3\text{-G}$ samples at room temperature, by varying the pump power. The amplitude, which is related to the photogenerated carrier density, increases linearly with pump power for both samples, as shown in Figures 4.8(a), 4.8(b) and 4.8(c), showing that we are not saturating the optical transitions in our experiments. The τ_{fast} of BLG in Figure 4.8(d) increases with pump fluence at low fluence, and is attributed to the

coupling between electrons and optical phonons — the number of optical phonons created by hot electron relaxation is proportional to the pump fluence, and these optical phonons can be reabsorbed by the electrons, slowing the rate of hot electron cooling. This behavior of τ_{fast} versus pump fluence also agrees with theoretical calculations at low photoexcited electron density [29].

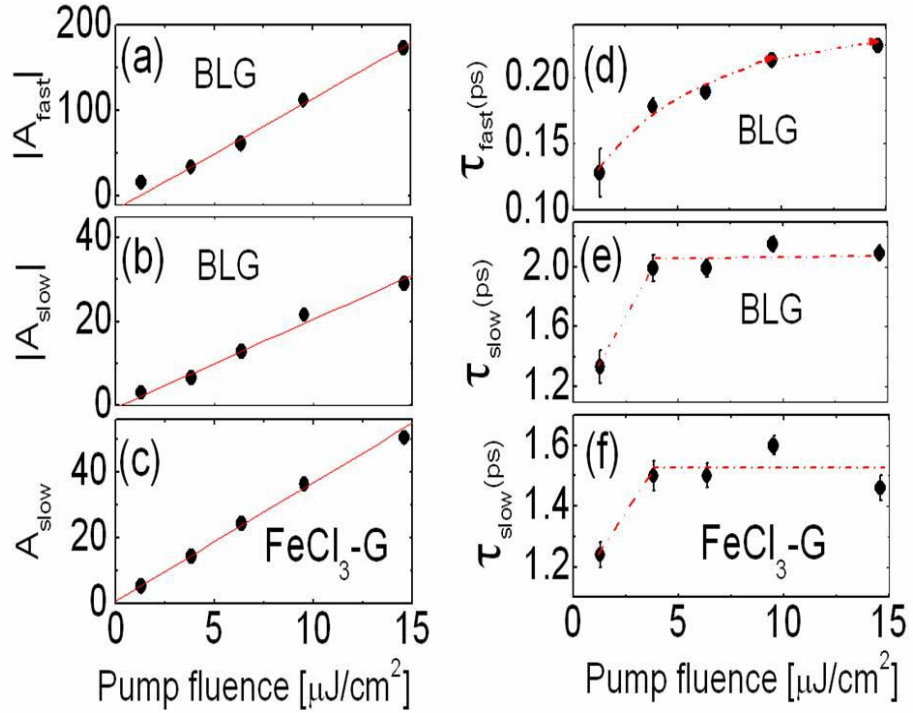


Figure 4.8 Pump fluence dependence of the amplitude (a) $|A_{fast}|$, (b) $|A_{slow}|$ in BLG and (c) A_{slow} in FeCl₃-G. (d) The value of τ_{fast} increases with the pump fluence. The behaviors of τ_{slow} with pump fluence in BLG and FeCl₃-G are presented in (e), (f), respectively. The red solid lines are linear fits, and the dash dot lines are guide to the eyes.

The behavior of τ_{slow} in both samples are very similar, as seen in Figures 4.8(e) and 4.8(f). The value of τ_{slow} increases at low fluence and become fluence-independent beyond a fluence of 3.8 $\mu\text{J}/\text{cm}^2$. With increasing pump fluence, hot electron relaxation

creates a larger number of optical phonons. These optical phonons can couple energy back into the electron distribution by being reabsorbed, thereby slowing the rate of electron cooling. This accounts for the increase in τ_{slow} with increasing pump fluence. At high pump fluences, hot electrons and optical phonon modes reach a quasi-equilibrium. Here the decay of the electron energy is controlled by the relaxation of optical phonons which occurs through coupling to low-energy acoustic phonon modes. Therefore, the decay of optical phonons serves as a bottleneck for the electron energy relaxation and the limiting value of τ_{slow} at high pump fluence reflects the relaxation time for the lifetime of optical phonon modes [18]. Hence τ_{slow} levels off at high pump fluence.

4.6 Conclusion

In this chapter, we have investigated the ultrafast carrier dynamics in BLG and FeCl₃-G grown on SiO₂/Si substrates from 10 K to room temperature. A fast relaxation process followed by a slower one is found in the BLG sample. However, in FeCl₃-G sample, different carrier dynamics are observed: an opposite sign of $\Delta R/R$, a slower rise time, and a single (instead of double) exponential relaxation. We attribute these differences in dynamics to the down-shifting of the Fermi level in FeCl₃-G, as well as the formation of numerous horizontal bands arising from the *d*-orbitals of Fe. Our work shows that intercalation can dramatically change the electronic structure of graphene and its associated carrier dynamics. Most of this work has been published in Applied Physics Letters **97**, 141910 (2010).

References

- [1] K. S. Novoselov, A. K. Geim, S. V. Morozov, D. Jiang, Y. Zhang, S. V. Dubonos, I. V. Grigorieva, and A. A. Firsov, *Science* **306**, 666 (2004).
- [2] A. K. Geim, and K. S. Novoselov, *Nat. Mater.* **6**, 183 (2007).
- [3] Y. B. Zhang, Y. W. Tan, H. L. Stormer, and P. Kim, *Nature* **438**, 201 (2005).
- [4] S. Y. Zhou, G. H. Gweon, A. V. Fedorov, P. N. First, W. A. De Heer, D. H. Lee, F. Guinea, A. H. C. Neto, and A. Lanzara, *Nat. Mater.* **6**, 770 (2007).
- [5] J. B. Oostinga, H. B. Heersche, X. L. Liu, A. F. Morpurgo, and L. M. K. Vandersypen, *Nat. Mater.* **7**, 151 (2008).
- [6] G. H. Li, A. Luican, J. dos Santos, A. H. C. Neto, A. Reina, J. Kong, and E. Y. Andrei, *Nat. Phys.* **6**, 109 (2010).
- [7] R. Kundu, *Int. J. Mod. Phys. B* **25**, 1877 (2011).
- [8] S. Adam, and S. Das Sarma, *Phys. Rev. B* **77**, 115436 (2008).
- [9] R. Sensarma, E. H. Hwang, and S. Das Sarma, *Phys. Rev. B* **82**, 195428 (2010).
- [10] Y. B. Zhang, T. T. Tang, C. Girit, Z. Hao, M. C. Martin, A. Zettl, M. F. Crommie, Y. R. Shen, and F. Wang, *Nature* **459**, 820 (2009).
- [11] M. Sprinkle, D. Siegel, Y. Hu, J. Hicks, A. Tejada, A. Taleb-Ibrahimi, P. Le Fèvre, F. Bertran, S. Vizzini, H. Enriquez, S. Chiang, P. Soukiassian, C. Berger, W. A. de Heer, A. Lanzara, and E. H. Conrad, *Phys. Rev. Lett.* **103**, 226803 (2009).
- [12] A. Reina, X. T. Jia, J. Ho, D. Nezich, H. B. Son, V. Bulovic, M. S. Dresselhaus, and J. Kong, *Nano Lett.* **9**, 30 (2009).
- [13] Z. Q. Luo, T. Yu, J. Z. Shang, Y. Y. Wang, S. Lim, L. Liu, G. G. Gurzadyan, Z. X. Shen, and J. Y. Lin, *Adv. Funct. Mater.* **21**, 911 (2011).
- [14] J. M. Dawlaty, S. Shivaraman, M. Chandrashekhar, F. Rana, and M. G. Spencer, *Appl. Phys. Lett.* **92**, 042116 (2008).
- [15] T. Kampfrath, L. Perfetti, F. Schapper, C. Frischkorn, and M. Wolf, *Phys. Rev. Lett.* **95**, 187403 (2005).
- [16] M. Breusing, C. Ropers, and T. Elsaesser, *Phys. Rev. Lett.* **102**, 086809 (2009).
- [17] H. N. Wang, J. H. Strait, P. A. George, S. Shivaraman, V. B. Shields, M. Chandrashekhar, J. Hwang, F. Rana, M. G. Spencer, C. S. Ruiz-Vargas, and J. Park, *Appl. Phys. Lett.* **96**, 081917 (2010).
- [18] L. B. Huang, G. V. Hartland, L. Q. Chu, Luxmi, R. M. Feenstra, C. X. Lian, K. Tahy, and H. L. Xing, *Nano Lett.* **10**, 1308 (2010).
- [19] R. W. Newson, J. Dean, B. Schmidt, and H. M. van Driel, *Opt. Express* **17**, 2326 (2009).
- [20] P. A. George, J. Strait, J. Dawlaty, S. Shivaraman, M. Chandrashekhar, F. Rana, and M. G. Spencer, *Nano Lett.* **8**, 4248 (2008).
- [21] H. Choi, F. Borondics, D. A. Siegel, S. Y. Zhou, M. C. Martin, A. Lanzara, and R. A. Kaindl, *Appl. Phys. Lett.* **94**, 172102 (2009).
- [22] S. Butscher, F. Milde, M. Hirtschulz, E. Malic, and A. Knorr, *Appl. Phys. Lett.* **91**, 203103 (2007).
- [23] R. Bistritzer, and A. H. MacDonald, *Phys. Rev. Lett.* **102**, 206410 (2009).
- [24] D. Sun, Z. K. Wu, C. Divin, X. B. Li, C. Berger, W. A. de Heer, P. N. First, and T. B. Norris, *Phys. Rev. Lett.* **101**, 157402 (2008).

- [25] M. S. Dresselhaus, and G. Dresselhaus, *Adv. Phys.* **51**, 1 (2002).
- [26] N. Jung, N. Kim, S. Jockusch, N. J. Turro, P. Kim, and L. Brus, *Nano Lett.* **9**, 4133 (2009).
- [27] G. Giovannetti, P. A. Khomyakov, G. Brocks, P. J. Kelly, and J. van den Brink, *Phys. Rev. B* **76**, 073103 (2007).
- [28] A. H. Castro Neto, F. Guinea, N. M. R. Peres, K. S. Novoselov, and A. K. Geim, *Rev. Mod. Phys.* **81**, 109 (2009).
- [29] W. K. Tse, and S. Das Sarma, *Phys. Rev. B* **79**, 235406 (2009).
- [30] N. Caswell, and S. A. Solin, *Solid State Commun.* **27**, 961 (1978).
- [31] C. Underhill, S. Y. Leung, G. Dresselhaus, and M. S. Dresselhaus, *Solid State Commun.* **29**, 769 (1979).
- [32] N. B. Hannay, T. H. Geballe, B. T. Matthias, K. Andres, P. Schmidt, and D. MacNair, *Phys. Rev. Lett.* **14**, 225 (1965).
- [33] G. Csanyi, P. B. Littlewood, A. H. Nevidomskyy, C. J. Pickard, and B. D. Simons, *Nat. Phys.* **1**, 42 (2005).
- [34] X. S. Li, W. W. Cai, J. H. An, S. Kim, J. Nah, D. X. Yang, R. Piner, A. Velamakanni, I. Jung, E. Tutuc, S. K. Banerjee, L. Colombo, and R. S. Ruoff, *Science* **324**, 1312 (2009).
- [35] Z. H. Ni, H. M. Wang, J. Kasim, H. M. Fan, T. Yu, Y. H. Wu, Y. P. Feng, and Z. X. Shen, *Nano Lett.* **7**, 2758 (2007).
- [36] Y. Y. Wang, Z. H. Ni, Z. X. Shen, H. M. Wang, and Y. H. Wu, *Appl. Phys. Lett.* **92**, 043121 (2008).
- [37] D. Zhan, L. Sun, Z. H. Ni, L. Liu, X. F. Fan, Y. Y. Wang, T. Yu, Y. M. Lam, W. Huang, and Z. X. Shen, *Adv. Funct. Mater.* **20**, 3504 (2010).
- [38] Z. H. Ni, Y. Y. Wang, T. Yu, Y. M. You, and Z. X. Shen, *Phys. Rev. B* **77**, 235403 (2008).
- [39] L. Liu, S. M. Ryu, M. R. Tomasik, E. Stolyarova, N. Jung, M. S. Hybertsen, M. L. Steigerwald, L. E. Brus, and G. W. Flynn, *Nano Lett.* **8**, 1965 (2008).
- [40] A. Das, S. Pisana, B. Chakraborty, S. Piscanec, S. K. Saha, U. V. Waghmare, K. S. Novoselov, H. R. Krishnamurthy, A. K. Geim, A. C. Ferrari, and A. K. Sood, *Nat. Nanotechnol.* **3**, 210 (2008).
- [41] S. Pisana, M. Lazzeri, C. Casiraghi, K. S. Novoselov, A. K. Geim, A. C. Ferrari, and F. Mauri, *Nat. Mater.* **6**, 198 (2007).
- [42] M. Lazzeri, and F. Mauri, *Phys. Rev. Lett.* **97**, 266407 (2006).
- [43] E. E. M. Chia, D. Talbayev, J.-X. Zhu, H. Q. Yuan, T. Park, J. D. Thompson, C. Panagopoulos, G. F. Chen, J. L. Luo, N. L. Wang, and A. J. Taylor, *Phys. Rev. Lett.* **104**, 027003 (2010).
- [44] A. Othonos, *J. Appl. Phys.* **83**, 1789 (1998).
- [45] G. Kresse, and J. Furthmüller, *Phys. Rev. B* **54**, 11169 (1996).
- [46] C. Bauer, J. P. Abid, and H. H. Girault, *J. Phys. Chem. B* **110**, 4519 (2006).
- [47] X. Q. Zou, D. Zhan, X. F. Fan, D. Lee, S. K. Nair, L. Sun, Z. H. Ni, Z. Q. Luo, L. Liu, T. Yu, Z. X. Shen, and E. E. M. Chia, *Appl. Phys. Lett.* **97**, 141910 (2010).

Chapter 5. Terahertz Time-Domain spectroscopy studies of bilayer graphene

This chapter is focused on conductivity experiments of bilayer graphene using terahertz time-domain spectroscopy. A rotation between two graphene layers can induce van-Hove singularities which can be reflected in the real part of optical conductivity. The overall Drude shape was analyzed using a disorder-dependent model, while the conductivity peak at ~ 2.7 THz was attributed to van-Hove singularity.

5.1 Introduction

In bilayer graphene (BLG), electrons can then hop between these two A sites with a hopping energy t_{\perp} . In the undoped case, though both SLG and BLG are gapless semi-metals, carriers in SLG exhibit linear dispersion, while those in BLG show quadratic dispersion. An energy gap in SLG opens up due to finite geometry effects, but its control has proven to be unreliable [1]. On the other hand, the electronic gap in BLG can be reliably opened and controlled by an applied electric field, shown theoretically and demonstrated experimentally [2-5], and promises interesting applications. Both SLG and BLG however, are sensitive to disorder. Hence, to realize graphene-based optoelectronic devices, an understanding of the temperature and disorder effects in the transport and spectroscopic properties of BLG is needed. Temperature and disorder-dependent conductivity of BLG have been derived theoretically [1, 6]. Experimentally, spectroscopies (from terahertz (THz) to visible) and ultrafast dynamics of various flavors of graphene have been reported, such as SLG, few and many-layer

graphene, and graphite [7-11]. For example, Fourier-transform infrared spectroscopy (FTIR) on large-area MLG grown by chemical vapor deposition (CVD) revealed a Drude-like frequency dependence of the spectral density from THz to mid-infrared at different carrier concentrations [12]. In addition, graphene plasmons, which lie in the THz range, are strongly coupled to the interband electronic transitions and decay by exciting interband electron-hole pairs [13]. Hence knowledge of graphene's electromagnetic response, as a function of disorder, in the THz frequency range is critical for applications such as graphene-based THz oscillators [14].

BLG grown by CVD also has a great tendency to twist. A typical 10 mm x 10 mm piece of CVD-BLG has been shown to be a collection of crystallites of twisted BLG with a distribution of different twisting angles [15, 16]. Twisting occurs when there is rotation between the top and bottom layers of BLG (see Figure 5.1). When there is rotation through a (twisting) angle θ about an A (B') site in BLG, only a discrete set of commensurate angles is allowed [17]:

$$\cos(\theta_i) = \frac{3i^2 + 3i + 1/2}{3i^2 + 3i + 1}, \quad (5.1)$$

where $i = 0, 1, 2, \dots$. Such rotation between graphene layers have been observed as a Moiré pattern on graphite surfaces [18], and recently in BLG [15]. Such twisting causes van Hove singularities (VHS) to develop near the Fermi energy, with the van Hove singularities energy scale being a strong function of θ , resulting in an enhanced density of states at those energies [17]. Such enhancement in the density of states should show up in the conductivity spectrum. For example, for large twisting angles of 7.5° , 13.7° and 54.6° , anomalies in the real conductivity $\sigma_1(\omega)$ were seen in the visible region using contrast spectroscopy [19]. However, they have not been demonstrated in the THz regime.

An accurate characterization of electrical and optical conductivities at THz frequencies of BLG, as a function of temperature, disorder and twisting, is thus needed, but has not been reported.

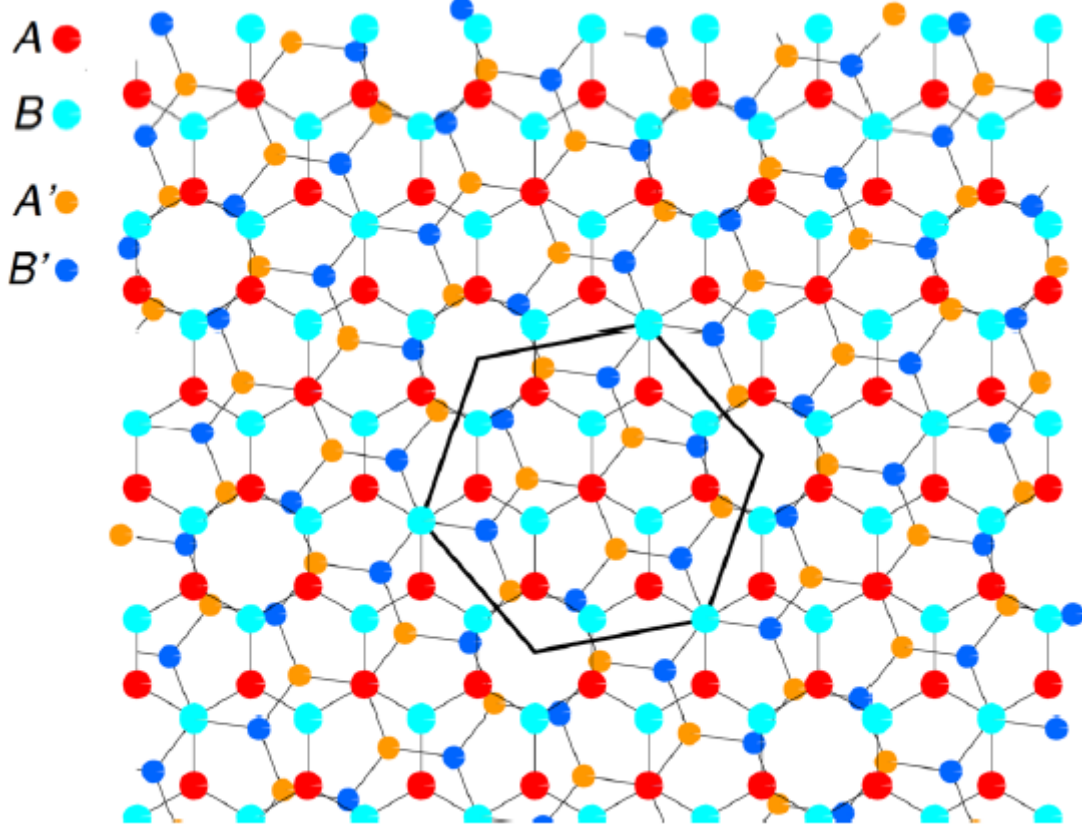


Figure 5.1 Atomic arrangement of atoms in BLG, for twisting angle $\theta = 21.8^\circ$. A (A') and B (B') are the sublattices of the first (second) layer. The black hexagon depicts the unit cell of the twisted BLG.

For certain angles of rotation, the energies of these VHS can be very close to the Fermi energy, of the order of milli-electronvolts (meV), which lie in the THz regime [17]. THz pulses with meV energy can thus probe such low-energy VHS. In this Chapter, we present THz time-domain spectroscopy (THz-TDS) studies of twisted BLG at different temperatures (10 K – 300 K), to study its frequency-dependent far-infrared conductivity.

On top of a Drude-like response, we see peaks in the real conductivity. The overall Drude shape was analyzed using a disorder-dependent model, while the conductivity peak at 2.7 THz was attributed to an enhanced density of states at that energy, which is caused by the presence of low-energy VHS arising from a commensurate twisting of the graphene layers relative to each other.

5.2 Experimental section

The samples studied here are large-scale BLG grown by CVD and deposited on z-cut quartz. Both contrast and absorption spectroscopies confirmed the sample to be a BLG film [20]. Our experimental set-up performs an average over the entire area of the sample. Nevertheless, our data were able to discern the feature arising from $\theta_{i=28} = 1.161^\circ$, on top of a broad background produced by the disorder in the sample, as will be discussed later in this Chapter.

The transmission THz spectra of the BLG were measured using a conventional THz-TDS system (TeraView Spectra 3000) with a Janis ST-100-FTIR cryostat. THz-TDS has proven to be a very useful noncontact technique to study the optical conductivity of materials in the far-infrared range without the need for Kramers-Kronig analysis [21, 22]. The THz wave was generated and detected by photoconductive antennas fabricated on low-temperature-grown GaAs films. The aperture diameter is 7 mm, enabling accurate measurements of the low-frequency spectral components of the THz wave. For each sample or reference run, 900 THz traces were taken over 180 seconds. The sample holder was moved from the sample to the reference position (and vice versa) by means of a vertical motorized stage with 2.5 μm resolution. The time-domain electric fields of a THz

pulse transmitted through Sample 1 ($\tilde{E}_s(t)$ — BLG deposited on 1-mm thick z-cut quartz substrate from CrysTec, Germany), as well as through the reference ($\tilde{E}_r(t)$, bare z-cut quartz substrate) are shown in the inset of Figure 5.2(a).

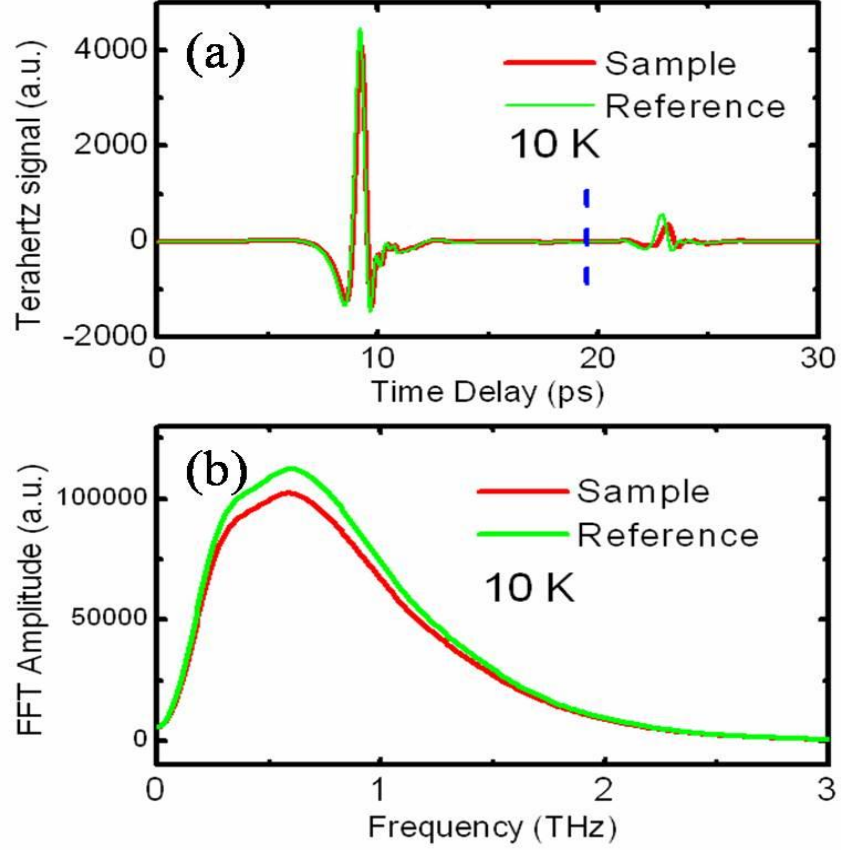


Figure 5.2 (a) Terahertz time-domain signal from sample and reference at 10 K. The dashed line indicates the point where we truncated the data before Fourier Transform. (b) Amplitude spectra in frequency domain from FFT of the main pulse in (a).

5.3 Data analysis

Before BLG deposition, the substrates for sample and reference were carefully characterized by THz-TDS — from their phase difference we obtained the thickness difference ΔL of the two substrates, which will be taken into account in our subsequent analysis. An accurate determination of ΔL is crucial to an accurate extraction of the

optical constants of thin film and nanomaterials [23]. After the main pulse, a weaker pulse (etalon) appears due to the first internal reflection in the z-cut quartz substrate. Since the main pulse and etalon pulse are well separated in the time domain, we truncate the time-domain data at the dotted line position as shown in the Figure 5.2(a). Subsequent data analysis was performed only on the main pulse without loss of validity. Fast Fourier Transform (FFT) was then performed to obtain the amplitude and phase as a function of frequency. The FFT amplitude spectrum of the main pulse is shown in Figure 5.2(b).

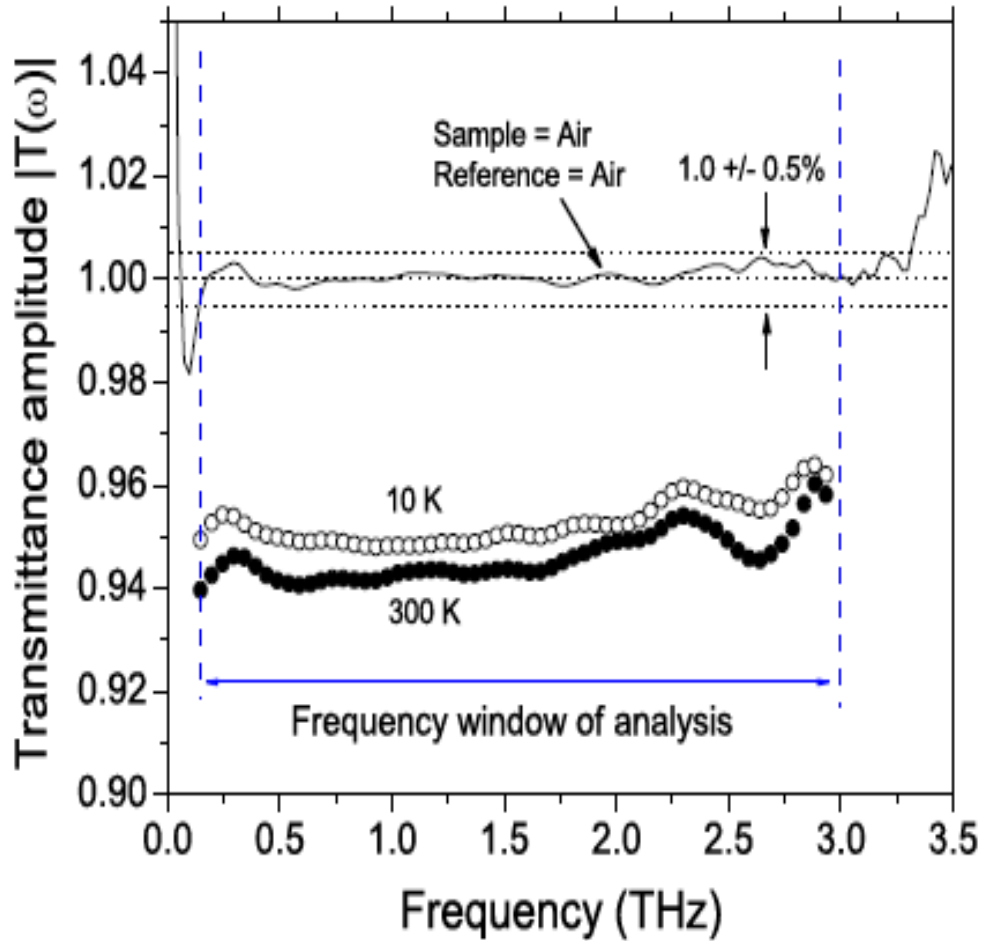


Figure 5.3 Amplitude of complex transmission coefficient (or transmittance), at 10 K and 300 K. The solid line indicates the transmission amplitude when both sample and reference are vacuum.

The absorption of the THz pulse by the BLG is obvious, even though the sample is of atomic-scale thickness. Figure 5.3 shows the amplitude of the experimental transmission coefficient (or transmittance) $\tilde{T}(\omega)$, defined as the ratio between complex spectral field of the sample $\tilde{E}_s(\omega)$ and reference $\tilde{E}_r(\omega)$. For both samples $|\tilde{T}(\omega)|$ is almost frequency-independent at about 95%. In the same figure is $|\tilde{T}(\omega)|$ when both sample and reference are vacuum — in this case $|\tilde{T}(\omega)|$ deviates only 0.5% away from unity in the frequency range 0.3 — 3.0 THz, which will be the frequency window of our analysis.

Theoretically, $\tilde{T}(\omega)$ can be written as [24]:

$$\tilde{T}(\omega) = \frac{\tilde{E}_s(\omega)}{\tilde{E}_r(\omega)} = \frac{2\tilde{n}(\tilde{n}_{sub} + 1) \exp[i\omega d(\tilde{n} - 1)/c] \exp[i\omega \Delta L(1 - \tilde{n}_{sub})/c]}{(1 + \tilde{n})(\tilde{n} + \tilde{n}_{sub}) + (\tilde{n} - 1)(\tilde{n}_{sub} - \tilde{n}) \exp[2i\omega d\tilde{n}/c]}, \quad (2.9)$$

where \tilde{n} and \tilde{n}_{sub} are the complex refractive indices of BLG and z-cut quartz substrate, respectively, d ($= 1$ nm) is the thickness of the BLG [25], ΔL is the thickness difference between sample and reference substrates, and c is the speed of light in vacuum. The complex refractive index \tilde{n}_{sub} of z-cut quartz was first measured with vacuum as reference at different temperatures. The result shows that z-cut quartz is a very good THz transparent material with a temperature-independent, and almost frequency-independent, refractive index, in our frequency and temperature range — we took its slight frequency dependence into account when calculating the optical constants of BLG. The complex refractive index $\tilde{n}(\omega) = n(\omega) + ik(\omega)$ was then extracted from Eq. (2.9) by numerical iteration, which was then used to calculate the complex optical conductivity $\tilde{\sigma}(\omega) = \sigma_1(\omega) + i\sigma_2(\omega)$, where $\sigma_1(\omega) = 2nk\omega\epsilon_0$ and $\sigma_2(\omega) = (\epsilon_\infty - n^2 + k^2)\omega\epsilon_0$, ϵ_0 being the free space permittivity, and high frequency dielectric constant $\epsilon_\infty = 8$ for graphene [11]. However, the values of $\sigma_2(\omega)$ are very sensitive to the value of ΔL ,

due to the very small thickness of BLG compared to $\Delta L (\sim \mu\text{m})$. Hence we only discuss the real conductivity σ_1 in our subsequent analysis. Note that, for a very thin metallic film on an insulating substrate, the following assumptions can be used: $n \gg n_{sub} > 1$ and $d\tilde{n}\omega/c \ll 1$, and Eq. (2.9) becomes the commonly-used thin-film expression [26]

$$T(\omega) = \frac{1 + \tilde{n}_{sub}}{1 + \tilde{n}_{sub} + Z_0 \sigma(\omega)d} \exp[i\omega\Delta L(1 - \tilde{n}_{sub})/c] \quad (5.2)$$

where Z_0 is the free space impedance. The values of σ_1 obtained from Eq. (5.2) are identical to those from Eq. (2.9).

5.4 Theoretical modeling and discussion

The Drude shaped conductivity of BLG is analyzed by an impurity scattering model, from which the chemical potential μ , impurity concentration n_i and inter-layer coupling energy t_\perp can be obtained. The origin of the 2.7-THz peak in real conductivity is discussed.

5.4.1 Chemical potential and charged impurity concentration of BLG by Raman spectroscopy

The BLG sample is also studied by the Raman spectroscopy. The G mode and 2D mode peaks were obtained by using the Lorentzian fitting. Standard undoped bilayer graphene G mode is located at 1580 cm^{-1} and 2D mode is 2688 cm^{-1} . The Raman measurement can be used to distinguish electron or hole doping by monitoring the G and 2D peak positions [27]. In our sample, the averaged D peak position is around $1581.7 \pm 0.5 \text{ cm}^{-1}$ and 2D mode position is $2689.8 \pm 2.4 \text{ cm}^{-1}$. From the G peak position shift compared with the standard undoped bilayer graphene,

$\omega_G - 1580 \text{ cm}^{-1} = (42 \text{ cm}^{-1}/\text{eV}) \times |\mu|$ [28], we can estimate the chemical potential of our BLG sample to be $(-0.040 \pm 0.012) \text{ eV}$ [28, 29]. The charged impurity concentration is less than 10^{13} cm^{-2} referring to the Raman result of monolayer graphene. Since one hexagonal cell has two lattice sites and its area is $A = 6 \times \frac{1}{2} \times \frac{\sqrt{3}}{2} a^2$, where a is the carbon-carbon bond length $a = 0.142 \text{ nm}$. The number of lattice sites on 1 cm^2 area is $N = 2 \times \frac{1}{A} \text{ cm}^2$, So the impurity concentration is calculated $< 10^{13}/N = 0.0026$ per BLG.

5.4.2 Impurity scattering model

The impurity scattering model was developed by Nilsson *et al.* to study the effects of disorder (defects) on the electronic properties in BLG and multilayer graphene [1]. It is a model that computes the frequency-dependent conductivity of Bernal-stacked BLG as a function of chemical potential μ , impurity concentration n_i , inter-layer coupling t_\perp and temperature. It starts by considering the Hamiltonian of the bilayer graphene under the tight binding model. By using the T -matrix and Coherent-Potential Approximation to consider unitary scattering introduced by vacancies, one derives the self-energy of BLG. With the Hamiltonian and self-energy, the Green's function matrix can be calculated. Finally, using the Kubo formula, the conductivity can be obtained from integrals of the Green's function elements. The self-energies can be obtained from the t -matrix by :

$$\Sigma_A = \frac{n_i}{F_A^0 + i\pi\rho_A^0(\omega)} \quad (5.3)$$

$$\Sigma_B = \frac{n_i}{F_B^0 + i\pi\rho_B^0(\omega)} \quad (5.4)$$

where n_i is the impurity density in the system and the ρ^0 's and F^0 's are given by

$$\rho_A^0(\omega) = -\frac{1}{\pi} \text{Im} \bar{G}_A = \frac{|\omega|}{2\Lambda^2} [1 + \Theta(|\omega| - t_\perp)] \quad (5.5)$$

$$\rho_B^0(\omega) = -\frac{1}{\pi} \text{Im} \bar{G}_B = \frac{|\omega|}{2\Lambda^2} [1 + \Theta(|\omega| - t_\perp)] + \frac{t_\perp}{2\Lambda^2} [1 - \Theta(|\omega| - t_\perp)] \quad (5.6)$$

$$F_A^0 \equiv -\text{Re}[\bar{G}_{AA}^0] = \frac{\omega}{2\Lambda^2} \log\left(\frac{\Lambda^4}{\omega^2 |\omega^2 - t_\perp^2|}\right) \quad (5.7)$$

$$F_B^0 \equiv -\text{Re}[\bar{G}_{BB}^0] = F_A^0 + \frac{t_\perp}{2\Lambda^2} \log\left|\frac{\omega - t_\perp}{\omega + t_\perp}\right| \quad (5.8)$$

$$\text{Re}[\sigma(\omega)] = \frac{2e^2}{\pi h} \int d\varepsilon \left[-\frac{n_F(\varepsilon + \omega) - n_F(\varepsilon)}{\omega} \right] \Xi(\varepsilon, \varepsilon + \omega) \quad (5.9)$$

From the contributions of the form $\langle J_{x1}, J_{x1} \rangle$ to the kernel which is

$$\Xi_{x1,x1} = \int_0^{\Lambda^2} d(v_F^2 k^2) \left\{ \text{Im}[g_{AA}^D(\varepsilon, k)] \text{Im}[g_{BB}^D(\varepsilon + \omega, k)] + \text{Im}[g_{BB}^D(\varepsilon, k)] \text{Im}[g_{AA}^D(\varepsilon + \omega, k)] \right\} \quad (5.10)$$

Similary, the cross term $\langle J_{x1}, J_{x2} \rangle$ has a contribution:

$$\Xi_{x1,x2} = 2 \int_0^{\Lambda^2} d(v_F^2 k^2) \text{Im}[g_{AB}^{ND}(\varepsilon, k)] \text{Im}[g_{AB}^{ND}(\varepsilon + \omega, k)] \quad (5.11)$$

Here, the superscript D (ND) stands for diagonal (nondiagonal) in the layer index, the components of the g matrices are expressed as:

$$g_{AA}^{D,ND} = \frac{\omega - \Sigma_B}{2D_-} \pm \frac{\omega - \Sigma_B}{2D_+} \quad (5.12)$$

$$g_{BB}^{D,ND} = \frac{\omega - t_\perp - \Sigma_A}{2D_-} \pm \frac{\omega + t_\perp - \Sigma_A}{2D_+} \quad (5.13)$$

$$g_{AB}^{D,ND} = \frac{k}{2D_-} \pm \frac{k}{2D_+} \quad (5.14)$$

$$\text{And } D_\pm(\omega, p) = [\omega \pm t_\perp - \Sigma_A(\omega)][\omega - \Sigma_B(\omega)] - k^2 \quad (5.15)$$

5.4.3 Impurity scattering model fitting

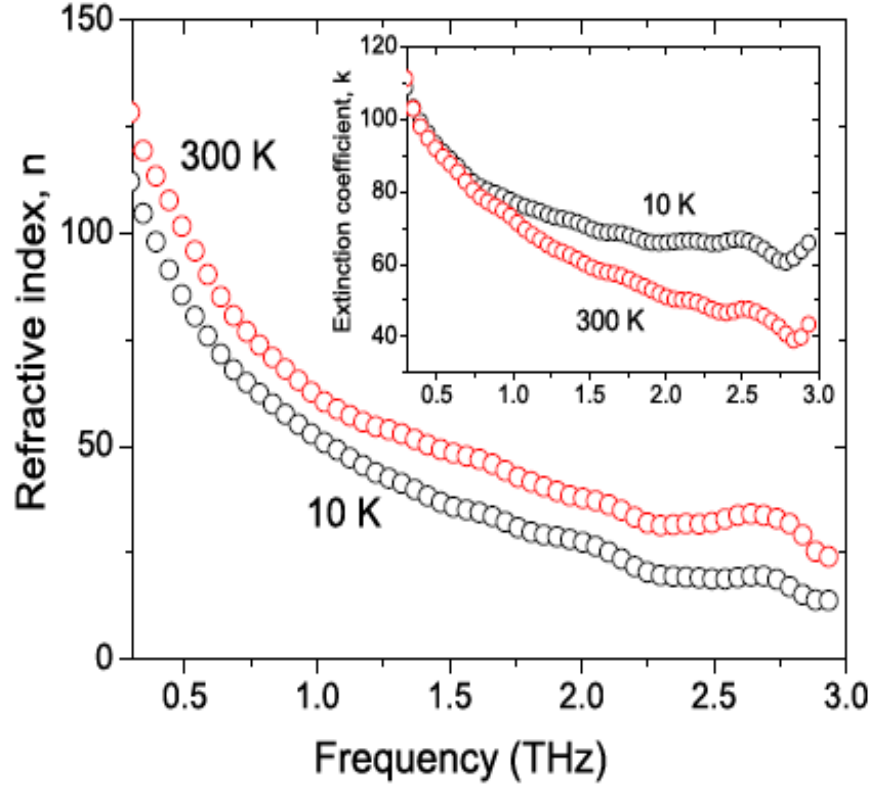


Figure 5.4 Refractive index $n(\omega)$ of BLG at different temperatures. Inset is the extinction coefficient $k(\omega)$.

Figure 5.4 shows the extracted refractive index $n(\omega)$ and extinction coefficient $k(\omega)$ at 10 K and 300 K. Both $n(\omega)$ and extinction coefficient $k(\omega)$ decrease with increasing frequency, consistent with the results of Wang *et al.*[30] obtained in the visible range. Figure 5.5 (a) shows $\sigma_1(\omega)$ at 10 K, 100 K and 300 K of Sample 1. Note the very small difference between $\sigma_1(\omega, 10 \text{ K})$ and $\sigma_1(\omega, 100 \text{ K})$. Superposed on top of a Drude-like response, is a strong and narrow peak centered at $\sim 2.7 \text{ THz}$. We first analyze the Drude-like background using a theoretical model developed by Nilsson *et al.* [1] for unitary scatterers for Bernal BLG. It starts by considering a Hamiltonian of the BLG under the tight binding model. Within the T-matrix approximation for unitary scattering,

one derives the electron self-energy of BLG, which gives the Green's function in the presence of disorder via the Dyson equation. The conductivity is then calculated from integrals of the Green's function elements (encoded in the kernel Ξ), as a function of chemical potential μ , impurity concentration n_i , interlayer coupling (hopping) t_\perp and temperature, to be

$$\sigma_1(\omega) \propto \frac{8e^2}{\pi h} \int d\varepsilon \left[-\frac{n_F(\varepsilon + \omega) - n_F(\varepsilon)}{\omega} \right] \Xi(\varepsilon, \varepsilon + \omega) \quad (5.16)$$

where n_F is the Fermi distribution function. The pre-factor $8e^2/(\pi h)$ is the *approximate* minimal conductivity per BLG, whose exact value will depend on the actual distribution of impurities among the inequivalent sites of the A and B sublattices [1]. In Figure 5.5(a), the 10 K, 100 K and 300 K data were *simultaneously* fitted with the model via Eq. (5.16), shown by black (10 K), red (100 K) and blue (300 K) solid lines. The resulting fitting parameters were $\mu^{\text{fit}} = -0.044$ eV, $n_i^{\text{fit}} = 0.00091$, and $t_\perp^{\text{fit}} = 0.049$ eV. Note the small difference between the 10 K and 100 K fits — where is consistent with the data. In fact, the theoretical $\sigma_1(\omega, 100 \text{ K})$ is smaller in magnitude than $\sigma_1(\omega, 10 \text{ K})$, showing that a spectral weight redistribution has taken place. We were initially surprised that the 100 K conductivity should be so similar to the 10 K conductivity, with the 300 K conductivity lying above both of them. These features, however, can be captured by the impurity-scattering model, lending strong credence to the validity of the model in explaining the THz data of Bernal BLG. In the above fittings, the fitted values of μ and n_i are consistent with Raman data of the same sample on the same substrate, with charged impurity concentration $< 10^{13} \text{ cm}^{-2}$ (corresponding to < 0.0026 per BLG) and $\mu = (-0.042 \pm 0.012)$ eV, determined by the Raman peak positions of the G and 2D bands, and the intensity ratio of the 2D and G peaks [29, 31, 32]. The unitary scatterer concentration

of the sample is typically $< 10^{-5}$, which was calculated using the ratio of the D and G peak intensities [33].

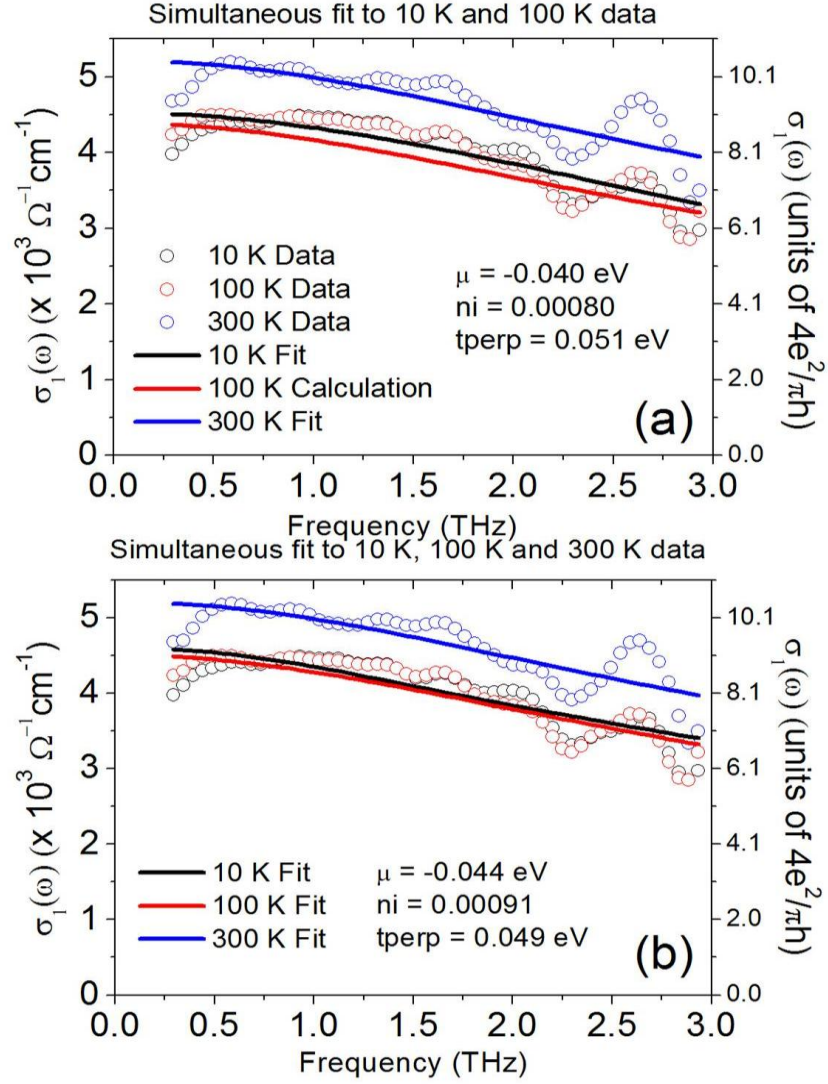


Figure 5.5 Real conductivity $\sigma_1(\omega)$ of BLG of (a) Sample 1 and (b) Sample 2. Circles are the experimental data. Solid lines are simultaneous fits of the unitary scattering model to the 10 K (black), 100 K (red) and 300 K (blue) data. Vertical axes on the right expresses $\sigma_1(\omega)$ in units of the minimum conductivity $8e^2/(\pi h)$ as specified in Nilsson's model [1].

Figure 5.5(b) shows the frequency dependence of the real conductivity, $\sigma_1(\omega)$, at 20

K, 100 K and 300 K, of Sample 2. The *simultaneous* fits (solid lines) of the data to Eq. (5.16) now yield fitting parameters $\mu^{\text{fit}} = -0.012$ eV, $n_i^{\text{fit}} = 0.00071$, and $t_{\perp}^{\text{fit}} = 0.076$ eV. Once again the fitted μ is consistent with Raman data, where $\mu = (-0.012 \pm 0.008)$ eV, and similar impurity concentration as Sample 1.

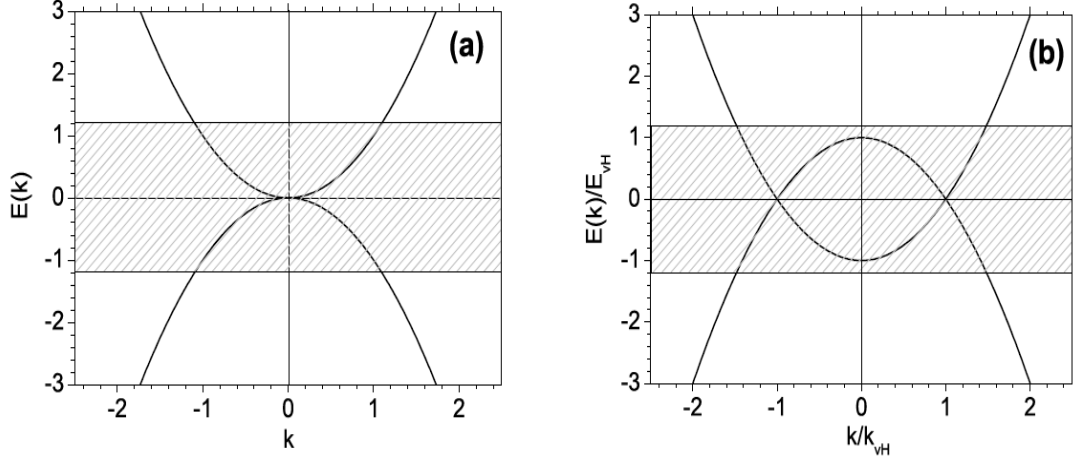


Figure 5.6 Schematic dispersion of a (a) Bernal BLG and (b) twisted BLG. The shaded region indicates the states that have been broadened by disorder in the sample, hence our data for twisted BLG could be fitted with a theory developed for Bernal BLG, but with a smaller value of t_{\perp} .

Note that both fitted values of t_{\perp}^{fit} are smaller than the value $t_{\perp} = 0.27$ eV for Bernal BLG. In fact, for a single monodomain of twisted BLG, the interlayer hopping is angle dependent, but for small angles it can be approximated as $t_{\perp}^{\theta} \approx 0.4t_{\perp} \approx 0.1$ eV [34], and $t_{\perp}^{\theta} < 0.1$ eV for larger θ 's (larger θ implies a larger separation between the layers, hence smaller interlayer hopping). Hence the value of t_{\perp}^{fit} obtained ($\approx 50 - 70$ meV) could be an average of interlayer couplings from all possible twisting angles in the sample, re-expressed in the form of perfect Bernal stacking. The fit to a theory based on an

"effective" Bernal BLG only works because disorder broadens all the features that can distinguish Bernal from twisted BLG at low energies, namely, the presence of VHS in the density of states of twisted BLGs [17] (see Figure 5.6). The difference in absolute values of $\sigma_1(\omega)$ between samples 1 and 2 is consistent with sample-to-sample variations observed in other works on BLG [35].

5.4.4 Van-Hove singularities in twisted BLG

A close inspection of $\sigma_1(\omega)$ reveals the presence of a peak that appears on top of the background signal. In twisted BLG, van-Hove singularities develop near the Fermi energy, which results in an enhanced density of states [17]. The energy scale of such van-Hove singularities is a strong function of twisting angle θ , given by [15]

$$E_{vhs} = \frac{8\pi\hbar v_F}{3a} |\sin(\theta/2)| - 2t_{\perp}^{\theta} \quad (5.17)$$

where $v_F = 1.0 \times 10^6$ m/s [36] is the Fermi velocity and $a \approx 2.46$ Å the lattice constant. We observed a strong and sharp peak at ~ 2.64 THz, whose presence is reproducible from sample to sample. Its position is consistent with the second non-zero E_{vhs} , computed from Eq. (5.17) to be 2.77 THz, and corresponds to $\theta_{28} = 1.161^\circ$ (from Eq. (5.1)). Note that the first non-zero E_{vhs} of 0.89 THz, arising from $\theta_{29} = 1.121^\circ$, is not visible from Figure 5.5. Theoretical density of states calculations [34] show that, for $\theta_{27} = 1.20^\circ$, the van-Hove peaks are still barely visible, whereas for $\theta_{30} = 1.08^\circ$ the van-Hove singularities have disappeared [34]. Also, since disorder builds up the density of states near the Dirac point, the van-Hove singularities are broadened by being in the middle of a continuum of disordered states. These factors may explain our inability to see any clear feature near 1 THz.

5.5 THz-TDS study of monolayer graphene

From Boltzmann transport theories, conductivity of monolayer graphene has a Drude form. The frequency dependent conductivity can be described by the Drude model using the dynamical conductivity $\tilde{\sigma}(\omega) = (iD) / (\pi(\omega + i\Gamma))$, where D is the Drude weight and carrier scattering rate $\Gamma = 1/\tau$. The Drude weight D has the value $D = (v_F e^2 / \hbar)(\pi n)^{1/2}$ when electron-electron interactions are neglected, with v_F being the Fermi velocity (1.0×10^6 m/s) and n the carrier density [12, 28]. The Drude weight in the monolayer graphene is quite different from classical materials where $D = \pi n e^2 / m^*$.

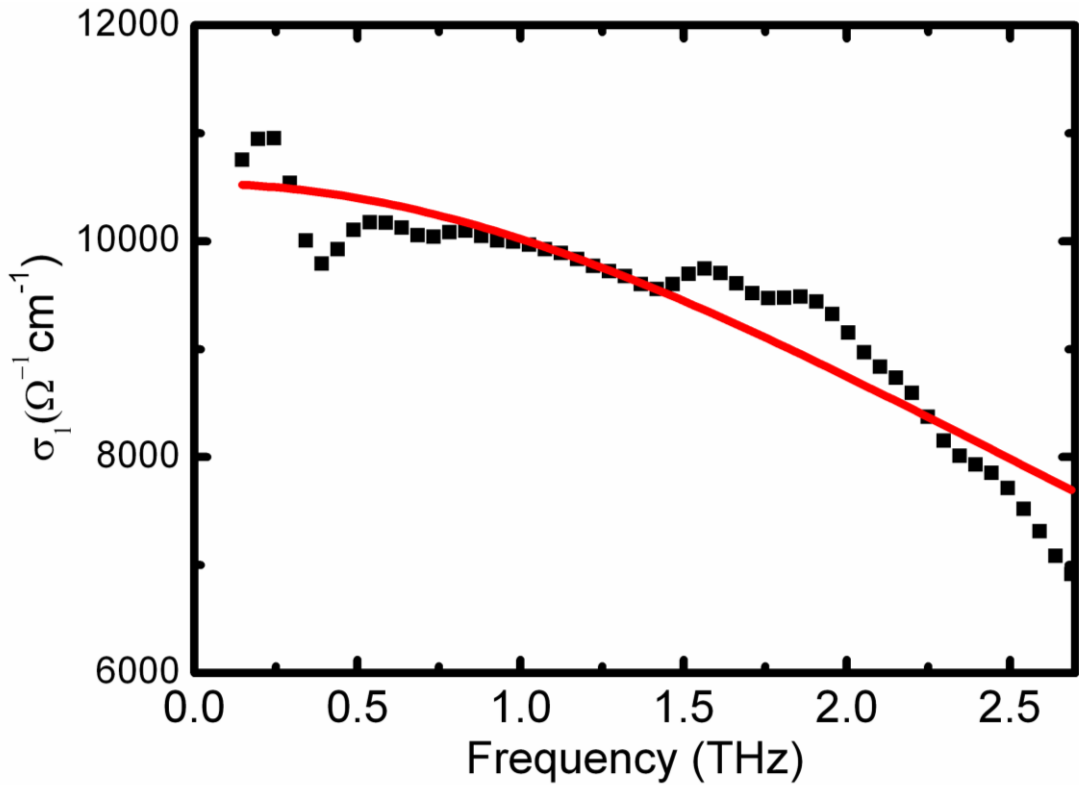


Figure 5.7 Conductivity of monolayer graphene (black square) and the Drude model fitting (red solid line).

We also have studied the conductivity of the monolayer graphene, as shown in Figure 5.7. Drude model $\tilde{\sigma}(\omega) = (iD)/(\pi(\omega + i\Gamma))$ is used to fit the real part conductivity of the monolayer graphene. Parameters like carrier density n and scattering time τ are obtained from the fitting results. In our monolayer graphene sample, the carrier density $n = 2.2 \times 10^{12} \text{ cm}^{-2}$ and $\tau = 36 \text{ fs}$ are consistent with the results of the infrared spectroscopy study of graphene, where the $n = 0.6 \times 10^{12} \text{ cm}^{-2}$ and $\tau = 20 \text{ fs}$ for epitaxial graphene [28].

5.6 Conclusion

We studied the far-infrared dielectric response of bilayer graphene at different temperatures by THz-TDS. On top of a Drude-like response, we see peaks in the real conductivity. The overall Drude shape was analyzed using a disorder-dependent model, while the conductivity peak 2.7 THz were attributed to an enhanced density of states at those energies, which is caused by the presence of low-energy van-Hove singularities arising from a commensurate twisting of the top graphene layer relative to the bottom layer. The work presented in this chapter has been submitted to Physical Review Letters. The fitting of BLG data using the impurity-scattering model was performed by Mr. Leaw Jia Ning of Assistant Professor Cheong Siew Ann's group.

References

- [1] J. Nilsson, A. H. Castro Neto, F. Guinea, and N. M. R. Peres, *Phys. Rev. B* **78**, 045405 (2008).
- [2] E. McCann, and V. I. Fal'ko, *Phys. Rev. Lett.* **96**, 086805 (2006).
- [3] E. McCann, *Phys. Rev. B* **74**, 161403 (2006).
- [4] E. V. Castro, K. S. Novoselov, S. V. Morozov, N. M. R. Peres, J. M. B. L. dos Santos, J. Nilsson, F. Guinea, A. K. Geim, and A. H. C. Neto, *Phys. Rev. Lett.* **99**, 216802 (2007).
- [5] J. B. Oostinga, H. B. Heersche, X. Liu, A. F. Morpurgo, and L. M. K. Vandersypen, *Nat. Mater.* **7**, 151 (2008).
- [6] H. P. Dahal, A. V. Balatsky, and J.-X. Zhu, *Phys. Rev. B* **77**, 115114 (2008).
- [7] H. Choi, F. Borondics, D. A. Siegel, S. Y. Zhou, M. C. Martin, A. Lanzara, and R. A. Kaindl, *Appl. Phys. Lett.* **94**, 172102 (2009).
- [8] N. M. R. Peres, F. Guinea, and A. H. Castro Neto, *Phys. Rev. B* **73**, 125411 (2006).
- [9] X. Q. Zou, D. Zhan, X. F. Fan, D. Lee, S. K. Nair, L. Sun, Z. H. Ni, Z. Q. Luo, L. Liu, T. Yu, Z. X. Shen, and E. E. M. Chia, *Appl. Phys. Lett.* **97**, 141910 (2010).
- [10] J. Z. Shang, Z. Q. Luo, C. X. Cong, J. Y. Lin, T. Yu, and G. G. Gurzadyan, *Appl. Phys. Lett.* **97**, 163103 (2010).
- [11] A. B. Kuzmenko, E. van Heumen, F. Carbone, and D. van der Marel, *Phys. Rev. Lett.* **100**, 117401 (2008).
- [12] J. Horng, C. F. Chen, B. S. Geng, C. Girit, Y. B. Zhang, Z. Hao, H. A. Bechtel, M. Martin, A. Zettl, M. F. Crommie, Y. R. Shen, and F. Wang, *Phys. Rev. B* **83**, 165113 (2011).
- [13] F. Rana, *IEEE Trans. Nanotechnol.* **7**, 91 (2008).
- [14] A. A. Dubinov, V. Y. Aleshkin, M. Ryzhii, T. Otsuji, and V. Ryzhii, *Appl. Phys. Express* **2**, 092301 (2009).
- [15] G. H. Li, A. Luican, J. dos Santos, A. H. C. Neto, A. Reina, J. Kong, and E. Y. Andrei, *Nat. Phys.* **6**, 109 (2010).
- [16] A. Reina, X. Jia, J. Ho, D. Nezich, H. Son, V. Bulovic, M. S. Dresselhaus, and J. Kong, *Nano Lett.* **9**, 30 (2009).
- [17] J. M. B. Lopes dos Santos, N. M. R. Peres, and A. H. Castro Neto, *Phys. Rev. Lett.* **99**, 256802 (2007).
- [18] Z. Y. Rong, and P. Kuiper, *Phys. Rev. B* **48**, 17427 (1993).
- [19] Y. Y. Wang, Z. H. Ni, L. Liu, Y. H. Liu, C. X. Cong, T. Yu, X. J. Wang, D. Z. Shen, and Z. X. Shen, *ACS Nano* **4**, 4074 (2010).
- [20] Z. H. Ni, H. M. Wang, J. Kasim, H. M. Fan, T. Yu, Y. H. Wu, Y. P. Feng, and Z. X. Shen, *Nano Lett.* **7**, 2758 (2007).
- [21] D. Grischkowsky, S. Keiding, M. Vanexter, and C. Fattinger, *J. Opt. Soc. Am. B* **7**, 2006 (1990).
- [22] J. B. Baxter, and C. A. Schmuttenmaer, *J. Phys. Chem. B* **110**, 25229 (2006).
- [23] C. Kadlec, V. Skoromets, F. Kadlec, H. Němec, J. Hlinka, J. Schubert, G. Panaitov, and P. Kužel, *Phys. Rev. B* **80**, 174116 (2009).
- [24] L. Duvillaret, F. Garet, and J. L. Coutaz, *IEEE J. Sel. Top. Quantum Electron.* **2**, 739 (1996).

- [25] A. Gupta, G. Chen, P. Joshi, S. Tadigadapa, and P. C. Eklund, *Nano Lett.* **6**, 2667 (2006).
- [26] R. D. Averitt, and A. J. Taylor, *J. Phys. Condens. Matter* **14**, R1357 (2002).
- [27] A. Das, S. Pisana, B. Chakraborty, S. Piscanec, S. K. Saha, U. V. Waghmare, K. S. Novoselov, H. R. Krishnamurthy, A. K. Geim, A. C. Ferrari, and A. K. Sood, *Nat. Nanotechnol.* **3**, 210 (2008).
- [28] H. G. Yan, F. N. Xia, W. J. Zhu, M. Freitag, C. Dimitrakopoulos, A. A. Bol, G. Tulevski, and P. Avouris, *ACS Nano* **5**, 9854 (2011).
- [29] C. Casiraghi, *Phys. Rev. B* **80**, 233407 (2009).
- [30] X. F. Wang, Y. P. Chen, and D. D. Nolte, *Opt. Express* **16**, 22105 (2008).
- [31] A. Das, B. Chakraborty, S. Piscanec, S. Pisana, A. K. Sood, and A. C. Ferrari, *Phys. Rev. B* **79**, 155417 (2009).
- [32] D. Ziegler, P. Gava, J. Güttinger, F. Molitor, L. Wirtz, M. Lazzeri, A. M. Saitta, A. Stemmer, F. Mauri, and C. Stampfer, *Phys. Rev. B* **83**, 235434 (2011).
- [33] L. G. Cançado, A. Jorio, E. H. M. Ferreira, F. Stavale, C. A. Achete, R. B. Capaz, M. V. O. Moutinho, A. Lombardo, T. S. Kulmala, and A. C. Ferrari, *Nano Lett.* **11**, 3190 (2011).
- [34] J. M. B. Lopes dos Santos, N. M. R. Peres, and A. H. Castro Neto, *Phys. Rev. B* **86**, 155449 (2012).
- [35] S. Das Sarma, E. H. Hwang, and E. Rossi, *Phys. Rev. B* **81**, 161407 (2010).
- [36] W. A. de Heer, C. Berger, X. S. Wu, P. N. First, E. H. Conrad, X. B. Li, T. B. Li, M. Sprinkle, J. Hass, M. L. Sadowski, M. Potemski, and G. Martinez, *Solid State Commun.* **143**, 92 (2007).

Chapter 6. Terahertz conductivity study of tin oxide nanowire film

In this chapter, the complex conductivity of SnO₂ nanowires is investigated by the Drude-Smith and plasmon model combined with the simple effective medium approximation. The temperature-dependent parameters of carrier density and scattering rate are extracted. Carrier mobility at 300 K is compared and discussed with bulk material and nanoparticles.

6.1 Introduction

Semiconducting oxide nanowires have provoked great interest in recent years due to their promising applications in photonic and optoelectronic devices [1]. Tin oxide (SnO₂), as a wide bandgap functional semiconductor, is of particular interest: Arising from its nanometer dimension-induced unique optical and electrical properties, applications of SnO₂ nanowires have been demonstrated in gas sensing, transparent conductors, field effect transistors, solar cells, etc [2, 3]. As such, understanding the physical properties of SnO₂ nanowires, like electrical conductivity, is very important for the above-mentioned applications. Traditional Hall measurements are commonly employed for the conductivity of thin films. However, it is a challenge for nanowire samples where ohmic contacts are required.

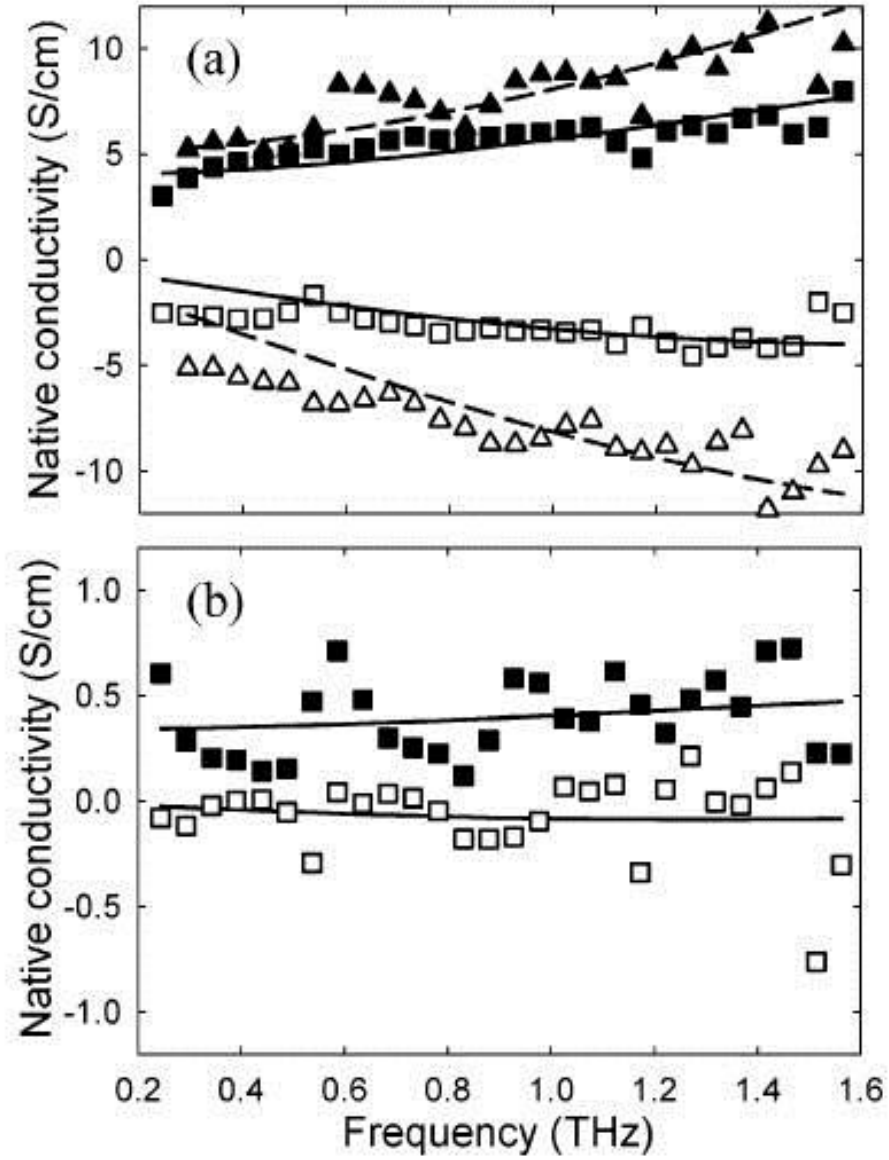


Figure 6.1 Native conductivity (points) and Drude-Smith model fitting (lines) of ZnO films and nanowires. (a) As-grown films (squares, solid lines) and as-grown nanowires (triangles, dashed lines). (b) Annealed films. Solid symbols are the real part of the conductivity, and open symbols are the imaginary part. Figure taken from Ref. [4].

Terahertz time-domain spectroscopy (THz-TDS) is a useful technique for obtaining the native (native means pure, without the host matrix) conductivity of nanomaterials in the THz regime. Fitting the conductivity with appropriate models enables the electron density and scattering time to be extracted. Baxter *et al.* [4] measured the conductivity of

ZnO nanowires, nanoparticles and thin films using THz-TDS, and obtained the frequency-dependent complex conductivity of ZnO nanomaterials, as shown in Figure 6.1. The Drude-Smith model (section 2.2.6) is used to fit the complex conductivity, and the electron density, scattering time and persistence-of-velocity parameter c_1 are presented in Table 6.1.

For bulk single crystal ZnO wafer, the mobility is found to be $\sim 200 \text{ cm}^2 \text{ V}^{-1} \text{ s}^{-1}$ by Hall measurement at 300 K [5]. However, for ZnO nanomaterials, the mobility can vary greatly depending on morphology, microstructure and growth conditions [6-8]. Nanomaterials have much larger surface to volume fraction and defects compared with bulk materials. Thus electrons moving through such materials often back-scatter off such defects. For a Drude conductor, the mobility can be calculated from the carrier density and scattering time using the formula:

$$\mu = \frac{e\tau}{m^*} \quad (6.1)$$

However, nanomaterials that obey Drude-Smith conductivity behavior have mobility given by $(1+c_1)\mu$, which is much smaller than the bulk mobility. For example, the ZnO nanowires have a mobility of $16 \text{ cm}^2 \text{ V}^{-1} \text{ s}^{-1}$ much smaller than that of bulk crystal [4].

	N_e (10^{17} cm^{-3})	τ (fs)	c_1
nanowires	19	28	-0.92
film	6.1	35	-0.84
annealed film	0.25	39	-0.7

Table 6.1 Parameters from the Drude-Smith fits of native conductivity (Ref. [4])

THz-TDS as a noncontact method, is advantageous for measuring the native conductivity and carrier density of semiconductor materials, such as ZnO nanowires, nanostructured TiO_2 , doped Si and GaAs wafers [4, 9-14]. THz-TDS measures both the amplitude and phase of the THz electric field, and extracts the extinction coefficient and refractive index without the need for Kramers-Kronig transformation. Though many materials have been studied by THz-TDS [15-28], a temperature-dependent THz-TDS study of SnO_2 nanowires has not been reported yet. In this chapter, films of randomly-aligned SnO_2 nanowires were investigated using THz-TDS in a wide temperature range from 10 to 300 K. By fitting the complex conductivity to the Drude-Smith model, the carrier density and scattering time are obtained, both of which are found to be temperature dependent.

6.2 Sample preparation and THz-TDS experiment

The SnO_2 nanowires were synthesized on 1 mm z -cut quartz substrate by a catalyst-assisted chemical vapor deposition (CVD) [29]. (The SnO_2 nanowires are grown by Dr. Cheng Chuanwei and Mr. Luo Jingshan of Prof. Fan Hongjin's group). The morphology of SnO_2 nanowires was characterized by a JEOL JSM-6700F field emission scanning electron microscope (FESEM). Structure characterization was performed by X-ray powder diffraction (XRD) using a Bruker D8 Advanced Diffractometer and $\text{Cu K}\alpha$ radiation. THz-TDS measurements were performed using a conventional THz-TDS system (TeraView Spectra 3000) with a Janis ST-100-FTIR cryostat. For each sample or reference run, 900 THz traces were taken over a 3-minute interval. The THz wave was generated and detected by photoconductive antennas fabricated on

low-temperature-grown GaAs films.

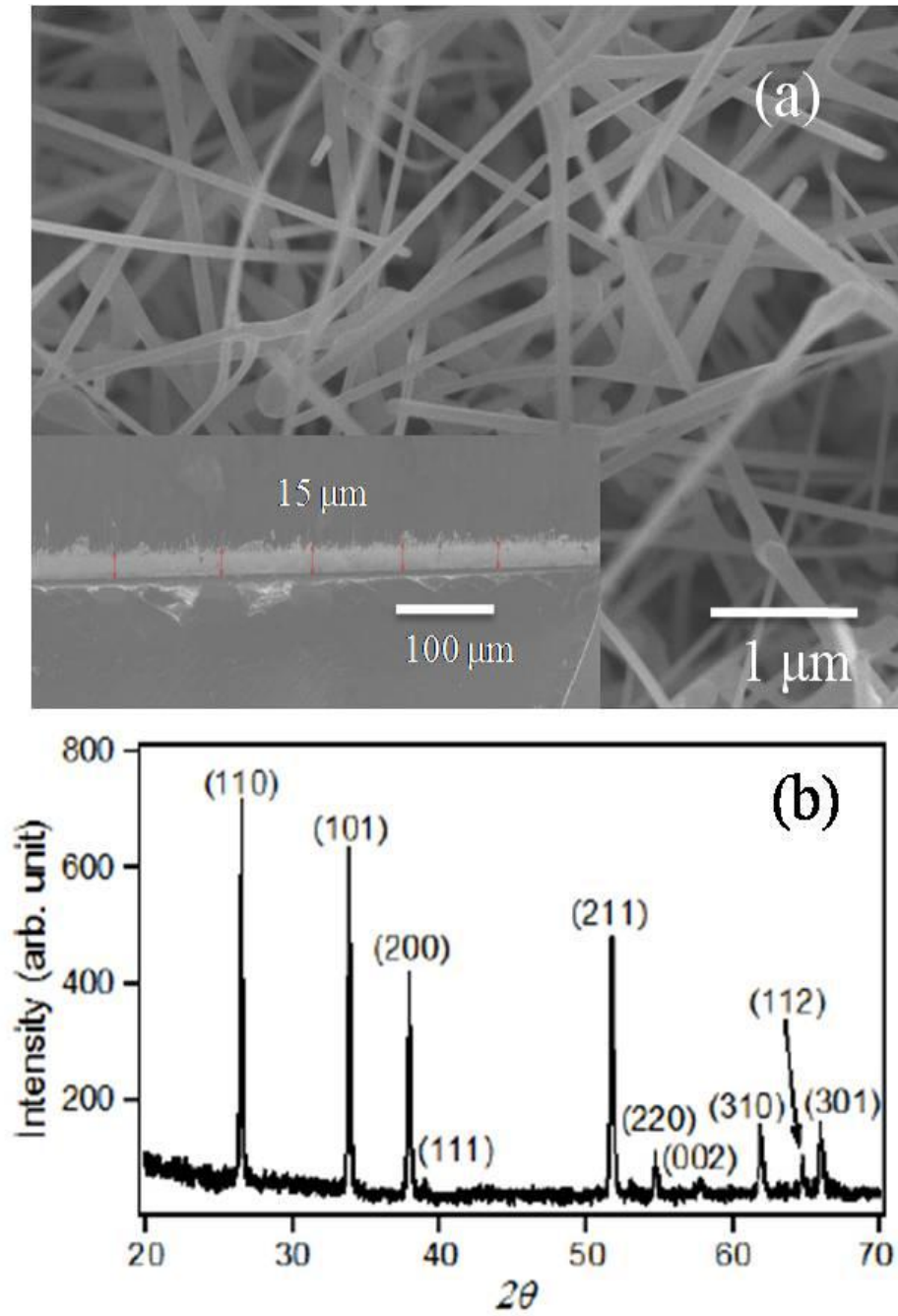


Figure 6.2 SEM image (a) and XRD pattern (b) of as grown SnO₂ nanowires. Inset of (a) is the cross-sectional view SEM image.

As shown in Figure 6.2(a), the as-grown SnO₂ nanowires were uniformly deposited on the z-cut quartz, with average diameters around 100 nm and length of several

micrometers (μm). The thickness of SnO_2 nanowire film is determined to be $\sim 15 \mu\text{m}$ by cross-sectional SEM image (Inset of Figure 6.2(a)). The further structural characterization by XRD (Figure 6.2(b)) confirmed that SnO_2 nanowires have a tetragonal rutile crystal structure.

THz-TDS measurements were performed using a THz-TDS system (TeraView Spectra 3000) incorporated with a Janis ST-100-FTIR cryostat. The THz wave was generated and detected by photoconductive antennas fabricated on low-temperature-grown GaAs films. To study the spectroscopic information of a material, we need a reference material with a well-known complex refractive index in the frequency region under investigation. In our experiment, a bare z-cut quartz is used as reference. The complex refractive index properties of the z-cut quartz are initially investigated as a function of different temperatures. Our results show that z-cut quartz is a very good transparent material in the terahertz range, with the complex refractive index $2.10+0.002i$, which is temperature- and almost frequency independent.

For each sample (SnO_2 nanowires on z-cut quartz) or reference (z-cut quartz) run, 900 THz traces were taken over a 3 minute interval. So the electric field of the THz pulses passing through the sample $E_s(t)$ and the reference $E_r(t)$ are recorded by moving the sample holder up and down as shown in Figure 6.3(a). After the main pulse, a small etalon pulse appears due to the multiple reflections between the front and back surface of the substrate. We can truncate the etalon in the time domain signal since the main pulse and etalon are well separated (Figure 6.3(b)). Although the optical thickness of SnO_2 nanowires is small compared with the bulk z-cut quartz, there still have some change to the terahertz waveform — attenuate and delay of the terahertz pulse, as shown in the

inset of Figure 6.3(b), the enlarged figure of terahertz pulse peak. The fast Fourier transform (FFT) allow us to obtain the frequency spectra information (amplitude and phase) of the sample and reference (Figure 6.3(c)).

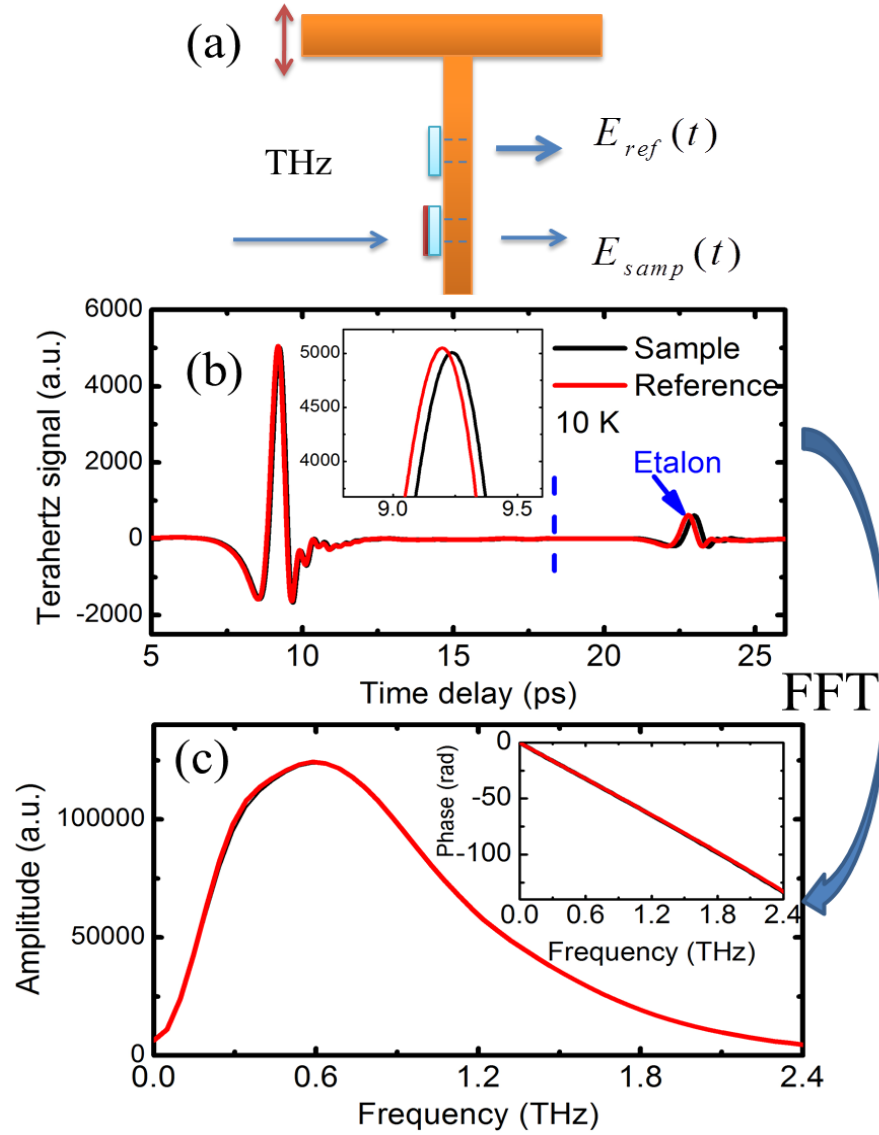


Figure 6.3 (a) THz-TDS sample holder figure. (b) Time domain signal of the THz pulse transmit through sample and reference. Inset: enlarged figure of the terahertz pulse peak (c) Amplitude and phase spectra after FFT from (a).

The frequency-dependent refractive index was then extracted by numerically

solving the equation,

$$\tilde{T}(\omega) = \frac{\tilde{E}_s(\omega)}{\tilde{E}_r(\omega)} = \frac{2\tilde{n}(\tilde{n}_{sub} + 1)\exp[i\omega d(\tilde{n} - 1)/c]\exp[i\omega\Delta L(1 - \tilde{n}_{sub})/c]}{(1 + \tilde{n})(\tilde{n} + \tilde{n}_{sub}) + (\tilde{n} - 1)(\tilde{n}_{sub} - \tilde{n})\exp(2i\omega d\tilde{n}/c)} \quad (2.9)$$

where \tilde{n} is the complex refractive index of the SnO₂-air composite, \tilde{n}_{sub} is the complex refractive index of z-cut quartz substrate, d is sample thickness, ΔL is the thickness difference between sample and reference substrates, and c is the speed of light in vacuum. An accurate determination of ΔL is crucial to an accurate extraction of the optical constants of thin film and nanomaterials [30]. — before growing the SnO₂ nanowires on the sample substrate, the thickness of the two z-cut quartz substrates were measured by a precision digital micrometer (resolution = 1 μm).

6.3 Results and discussions

The dielectric properties of measured materials are a composite of SnO₂ nanowires and vacuum. The dielectric properties of pure SnO₂ nanowires are analyzed by simple effective medium approximation. Drude-Smith model and plasmon model are used to fit the complex conductivity.

6.3.1 Dielectric properties of SnO₂ nanowires using simple EMA

The complex refractive index of the SnO₂ nanowires and vacuum composite is shown in Figure 6.4(a). After extracting the refractive index, we can obtain the complex dielectric function of the composite by using the relationship: $\tilde{\epsilon}_{eff} = \tilde{n}_{eff}^2$, as shown in Figure 6.4(b). Since the sample is a composite of pure SnO₂ nanowires and vacuum, We have to use effective medium theories to extract the frequency-dependent complex dielectric function of the pure nanowires from that of the composite [4, 17, 31].

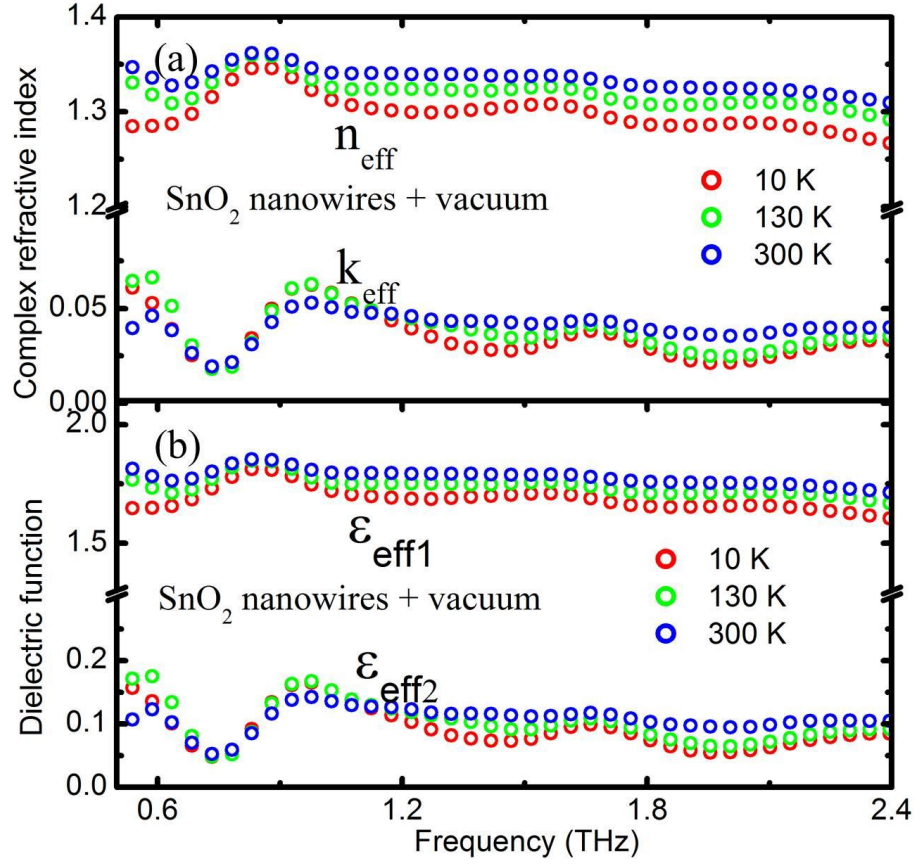


Figure 6.4 Complex refractive index and dielectric function of the SnO₂ nanowires and vacuum composite.

When deciding which EMA model to use, we make use of the fact that our SnO₂ nanowires are entangled with each other, so the sample is more percolated than not. Also, the volume fraction (0.077) is small, so we follow the method described in Han *et al.* [15, 32], where the simple effective theory was used for MgO nanocrystals (volume fraction 0.19) and ZnO tetrapod structures (volume fraction 0.017). We then extract the complex dielectric function of pure SnO₂ nanowires with the simple effective medium theory [15], $\tilde{\epsilon}_{eff}(\omega) = f\tilde{\epsilon}_m(\omega) + (1-f)\tilde{\epsilon}_h(\omega)$, where the filling factor f denotes the volume fraction of the nanowires, and is experimentally measured to be $f = 0.077$. $\tilde{\epsilon}_m(\omega)$ and $\tilde{\epsilon}_h(\omega)$ are the dielectric functions of SnO₂ nanowire and host medium, respectively. Here $\tilde{\epsilon}_h(\omega) = \epsilon_{vacuum} = 1.0$. The real and imaginary dielectric constants of the SnO₂ nanowire as

a function of frequency at different temperatures are obtained as shown in Figure 6.5(a).

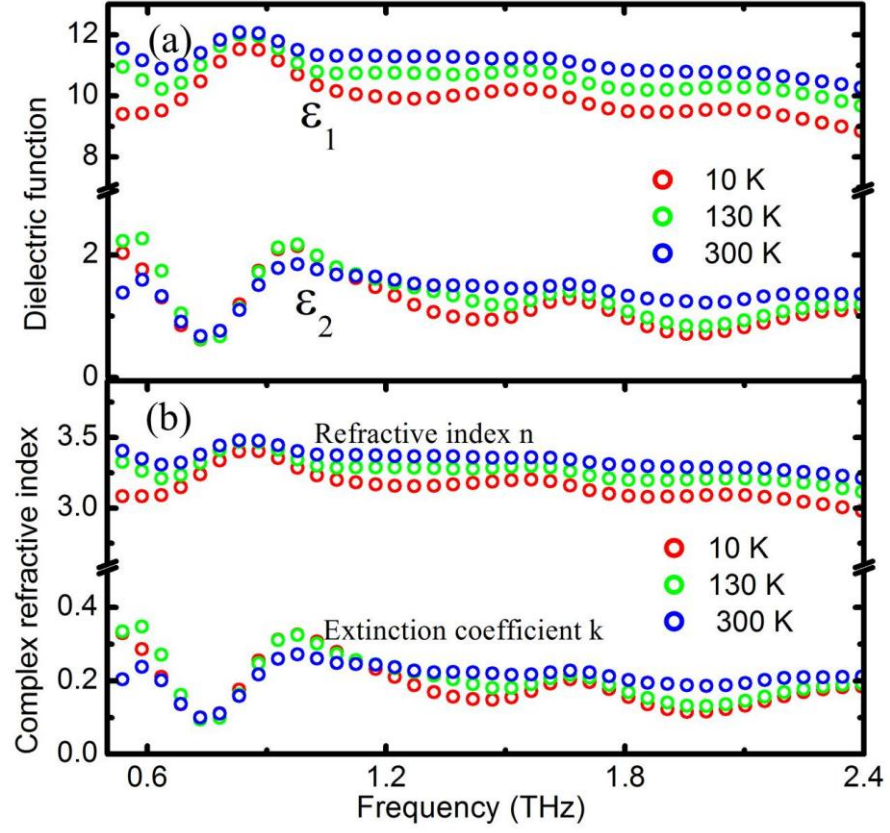


Figure 6.5 Dielectric function (a) and complex refractive index (b) of pure SnO₂ nanowires at different temperatures.

The refractive index and extinction coefficient can then be calculated respectively from the dielectric function $\varepsilon = \varepsilon_1 + i\varepsilon_2$.

$$n = \left(\frac{1}{2} (\varepsilon_1^2 + \varepsilon_2^2)^{1/2} + \frac{\varepsilon_1}{2} \right)^{1/2} \quad (6.2)$$

$$\text{and } k = \left(\frac{1}{2} (\varepsilon_1^2 + \varepsilon_2^2)^{1/2} - \frac{\varepsilon_1}{2} \right)^{1/2} \quad (6.3)$$

Figure 6.5(b) shows the extracted extinction coefficient $k(\omega)$ and refractive index $n(\omega)$ of the pure SnO₂ nanowires in the frequency range 0.5 THz — 2.4 THz and from 10 K — 300 K. The $n(\omega)$ slightly decreases with increasing frequency and increases with

temperature. The extinction coefficient $k(\omega) \approx 0.2$ is almost frequency-independent, because the lowest IR active transverse optical (TO) phonon mode is $\sim 140 \text{ cm}^{-1}$ (4.2 THz), well above the investigating frequency [33].

6.3.2 Complex conductivity fitting and discussion

The native conductivity $\tilde{\sigma}(\omega) = \sigma_1(\omega) + i\sigma_2(\omega)$ of SnO_2 nanowires can then be determined from $n(\omega)$ and $k(\omega)$ by the relationships:

$$\sigma_1(\omega) = 2nk\omega\epsilon_0; \quad (6.4)$$

$$\sigma_2(\omega) = (\epsilon_\infty - n^2 + k^2)\omega\epsilon_0, \quad (6.5)$$

where ϵ_0 is the free space permittivity, and ϵ_∞ is the high-frequency dielectric constant.

A collection of absorbing modes with frequency beyond the maximum investigation frequency ω_m acts as the high-frequency dielectric constant, and can be expressed as

$$\epsilon_\infty = 1 + \frac{2}{\pi} \int_{\omega_m}^{\infty} \frac{\epsilon_2(\omega)}{\omega} d\omega, \text{ where } \epsilon_2(\omega) = 2nk \text{ is the imaginary part of the dielectric}$$

function. Hence optical investigations in different frequency ranges (such as infrared, visible and ultraviolet) will have different corresponding ϵ_∞ . Moreover, ϵ_∞ does not just depend on the maximum investigated frequency as the definition indicates, but also depends on the temperature. Dielectric property studies show that the absorption modes will stiffen or soften with increasing temperature [34] — such stiffening or softening effects directly affect the frequency of the absorption modes and the value of ϵ_∞ . Hence, in our analysis, at every temperature, ϵ_∞ is one of the fitting parameters in the fit of $\sigma_1(\omega)$ and $\sigma_2(\omega)$ to the Drude-Smith model.

Due to the larger surface-to-volume ratio and defect concentration than in bulk single crystals, carrier localization and/or backscattering commonly occurs in nanowires,

resulting in a negative $\sigma_2(\omega)$. This negative $\sigma_2(\omega)$ deviates from the Drude model, which is often used to fit the conductivity of metals and semiconductors. Smith [35] considered the backscattering of carriers and proposed a modification to the Drude model. In the Drude-Smith model, an additional term appears in the complex conductivity to become (same as Eq. (2.21))

$$\tilde{\sigma}(\omega) = \frac{Ne^2\tau/m^*}{(1-i\omega\tau)} \left[1 + \frac{c_1}{(1-i\omega\tau)} \right] \quad (6.6)$$

where the parameters have been explained below Eq. (2.21). For SnO_2 , $m^* = 0.31m_0$ [36] where m_0 is the free electron mass. The Drude-Smith model has been used to fit the conductivity data of a variety of materials, such as TiO_2 nanoparticle arrays and ZnO nanomaterials [4, 37].

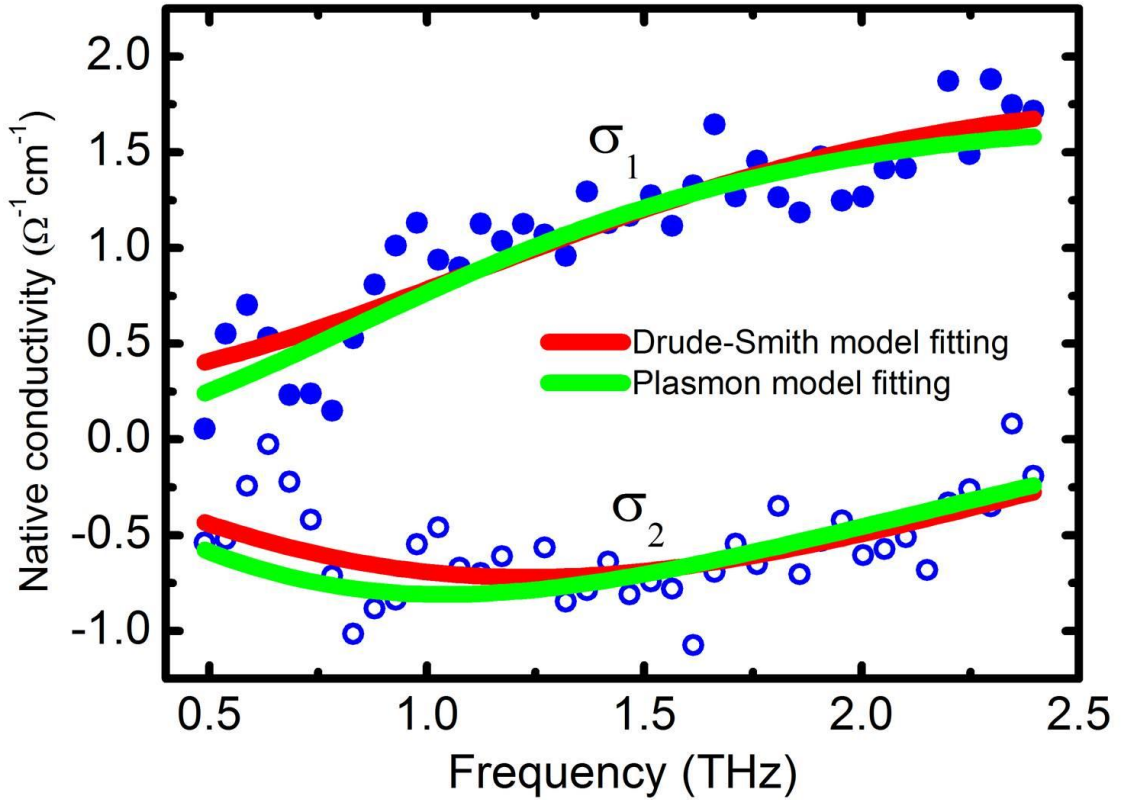


Figure 6.6 Drude-Smith model fitting (red solid line) and plasmon model fitting (green solid line) of native conductivity (solid and open circles) of SnO_2 nanowires at 300 K.

At every temperature, we obtain fitting parameters N , τ , c_1 and ε_∞ by *self-consistently* fitting $\sigma_1(\omega)$ and $\sigma_2(\omega)$ [given by Eq. (6.4) and Eq. (6.5)] with the Drude-Smith model [Eq. (6.6)]. The resulting $\sigma_1(\omega)$ and $\sigma_2(\omega)$, and the Drude-Smith fits, are shown in Figure 6.6. From the fits, ε_∞ varies from 9.4 to 10.8 between 10 K and 300 K. — these values are similar to the ε_∞ obtained from taking the value of n^2 just beyond our frequency window (~ 2.4 THz), as was done for single-walled carbon nanotubes [38] and ZnO nanoparticles [39]. From our fits, we find that the N and τ are temperature-dependent. The carrier density N increases from $\sim 3.8 \times 10^{16} \text{ cm}^{-3}$ at 10 K to $\sim 8.0 \times 10^{16} \text{ cm}^{-3}$ at 300 K, as shown in Figure 6.7(a). Since the electron effective mass ($0.31m_0$) is much smaller than the hole effective mass ($\sim 1.0 m_0$) [36], the electrons contribute more significantly to the photoconductivity and the extracted carrier density can be treated as electron density. Our extracted carrier density has the same order of magnitude as the result from a recent THz-TDS study of SnO_2 nanowires at room temperature [40]. As carrier density increases with temperature, more carriers are confined in the nanowires, which results in an increased carrier-carrier scattering rate. Another, greater electron-phonon scattering rate is expected in the higher temperatures [41]. These two reasons may explain a decreasing of the scattering time τ from ~ 70 fs at 10 K to ~ 50 fs at 300 K, as shown in Figure 6.7(b). The persistence of velocity parameter, c_1 , approaches -1 in Figure 6.7(c), this phenomenon often appears in disordered systems such as nanowires or nanoparticles, for example in ZnO nanowires ($c_1 = -0.92$) and dye-sensitized TiO_2 nanoparticles ($c_1 = -0.93$) [4, 37].

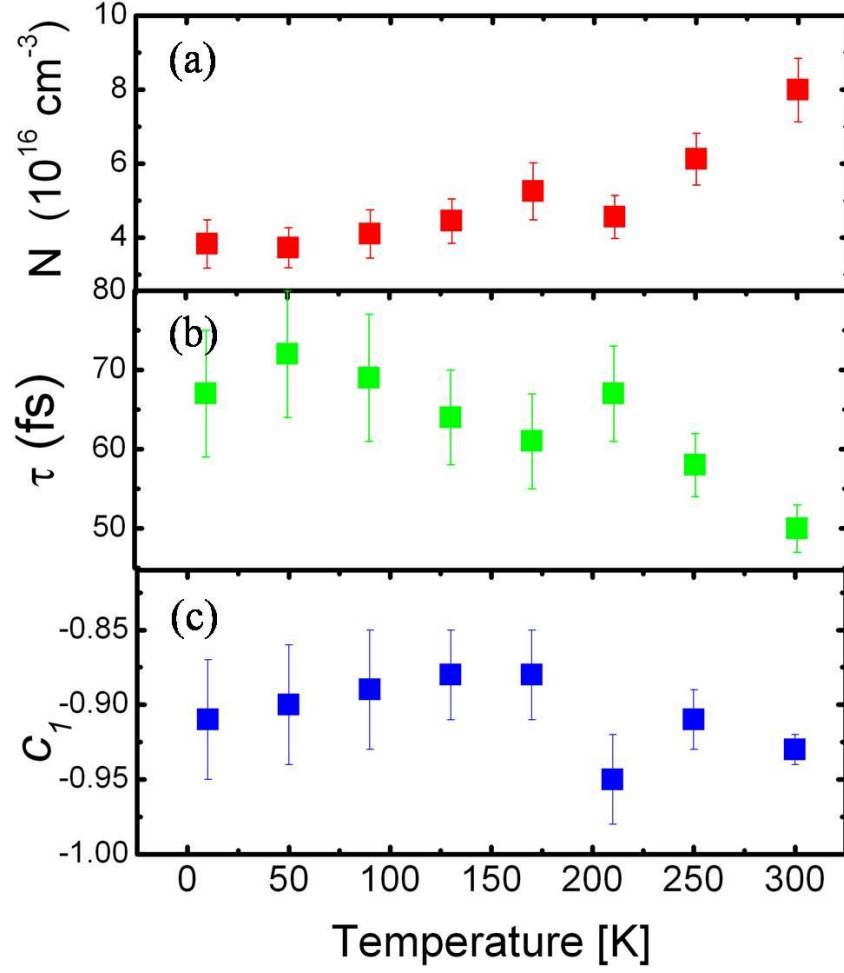


Figure 6.7 Carrier density (a), scattering time (b) and parameter c_1 (c) extracted from Drude-Smith model as a function of temperature.

The Drude-Smith model explains the conductivity deviation under one assumption that the carriers retain parts of their momentum only at the first scattering event, which has no clear physical basis. Plasmon model (described in Section 2.2.6) [12-14,42] offers an extension to the Drude model and has a very similar conductivity spectrum to the Drude-Smith model. The conductivity of the Plasmon model can be expressed as:

$$\tilde{\sigma}(\omega) = \frac{N\tau e^2 / m^*}{1 - i\omega\tau(1 - \omega_0^2 / \omega^2)} \quad (6.7)$$

The $\sigma_1(\omega)$ is maximum and $\sigma_2(\omega)$ crosses over the frequency axis at plasmon resonance frequency ω_0 . A larger restoring force will shift the ω_0 to higher frequency,

as $\omega_0 \propto \sqrt{N}$. The plasmon model is also used to fit the 300K conductivity data, as shown in Figure 6.6, it is almost identical to the Drude-Smith model fitting. Extracted parameters of N , τ and ω_0 as a function of temperatures are displayed in Figure 6.8. Compared with these parameters from Drude-Smith model, N is similar and τ has smaller values. The plasmon resonant frequency increases with temperature, which agrees with the plasmon model. From temperature-dependent carrier density $N(T)$, the thermal activation energy (E_D) for the ionization of the shallow donors was determined to be (68 ± 6) meV from the expression $N \propto \exp(\frac{-E_D}{2k_B T})$ [43]. Different activation energies of SnO_2 single crystal have been reported from 10 meV to 150 meV in different research groups [33]. The activation energy in our sample is close with Chang's result (~ 60 meV) [44].

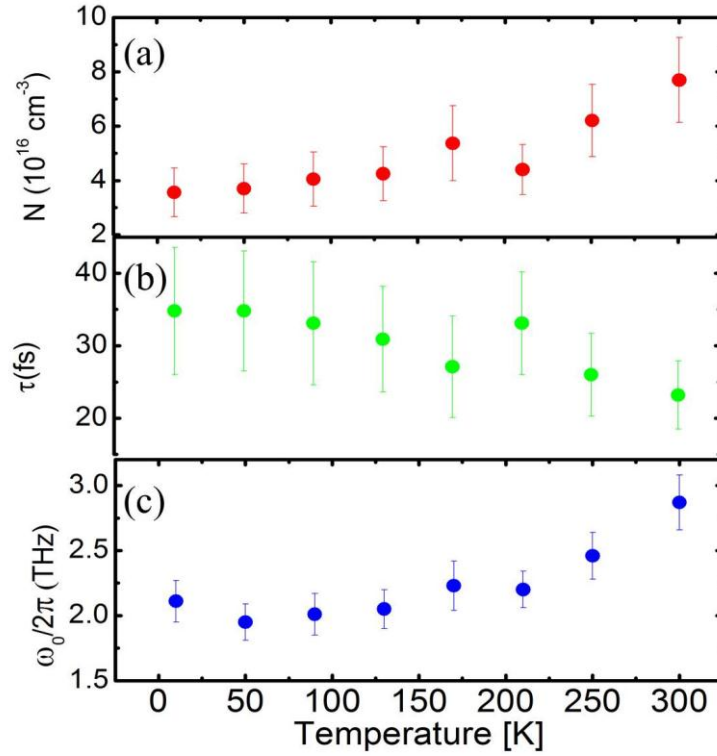


Figure 6.8 Carrier density (a), scattering time (b) and plasmon resonance frequency (c) extracted from plasmon model as a function of temperature.

6.3.3 Carrier mobility of SnO₂ nanowires

The room temperature (300 K) carrier mobility calculated from Drude model $\mu = e\tau / m^*$ is $\sim 287 \text{ cm}^2\text{V}^{-1}\text{s}^{-1}$. However, according to Drude-Smith model, the mobility should be $(1+c_l)\mu$. This gives an experimental carrier mobility of $\sim 20 \text{ cm}^2\text{V}^{-1}\text{s}^{-1}$ at the THz frequency range, which is one order magnitude smaller than the mobility of bulk SnO₂ ($\sim 250 \text{ cm}^2\text{V}^{-1}\text{s}^{-1}$) [45]. This is not surprising, since mobility can vary widely depending on morphology, microstructure and growth conditions [4]. A recent optical-pump THz-probe study done on dye-sensitized thin films made of sintered pastes of SnO₂ nanoparticles (10 nm wide, 20 nm long) [46], obtained a carrier mobility of $\sim 1.0 \text{ cm}^2\text{V}^{-1}\text{s}^{-1}$ at the THz range. Our value of room-temperature mobility is also consistent with that from the THz-TDS study of SnO₂ nanowires (50 - 100 nm in diameter, 10 μm long, $\mu \sim 72 \text{ cm}^2\text{V}^{-1}\text{s}^{-1}$) [40].

6.4 Conclusion

In conclusion, SnO₂ nanowires have been investigated by temperature-dependent THz-TDS from 0.5 THz to 2.4 THz. The complex refractive index and conductivity of SnO₂ nanowires have been obtained using the simple effective medium theory. The real and imaginary conductivity were simultaneously fitted to the Drude-Smith and plasmon model. The extracted carrier density increases and scattering time decreases with increasing temperature. The reduction in carrier mobility compared to the bulk material indicates the presence of carrier trapping and localization in these nanowires. The work presented in this chapter has been published in *Journal of Physics D: Applied Physics*, **45**, 465101 (2012).

References

- [1] E. N. Dattoli, Q. Wan, W. Guo, Y. B. Chen, X. Q. Pan, and W. Lu, *Nano Lett.* **7**, 2463 (2007).
- [2] S. Gubbala, V. Chakrapani, V. Kumar, and M. K. Sunkara, *Adv. Funct. Mater.* **18**, 2411 (2008).
- [3] H. Y. Yang, S. F. Yu, C. W. Cheng, S. H. Tsang, H. K. Liang, and H. J. Fan, *Appl. Phys. Lett.* **95**, 201104 (2009).
- [4] J. B. Baxter, and C. A. Schmuttenmaer, *J. Phys. Chem. B* **110**, 25229 (2006).
- [5] D. C. Look, D. C. Reynolds, J. R. Sizelove, R. L. Jones, C. W. Litton, G. Cantwell, and W. C. Harsch, *Solid State Commun.* **105**, 399 (1998).
- [6] Z. Y. Zhang, C. H. Jin, X. L. Liang, Q. Chen, and L. M. Peng, *Appl. Phys. Lett.* **88**, 073102 (2006).
- [7] K. Ellmer, *J. Phys. D: Appl. Phys.* **34**, 3097 (2001).
- [8] C. A. Wolden, T. M. Barnes, J. B. Baxter, and E. S. Aydil, *J. Appl. Phys.* **97**, 043522 (2005).
- [9] E. Hendry, M. Koeberg, B. O'Regan, and M. Bonn, *Nano Lett.* **6**, 755 (2006).
- [10] M. Vanexter, and D. Grischkowsky, *Appl. Phys. Lett.* **56**, 1694 (1990).
- [11] N. Katzenellenbogen, and D. Grischkowsky, *Appl. Phys. Lett.* **61**, 840 (1992).
- [12] R. Ulbricht, E. Hendry, J. Shan, T. F. Heinz, and M. Bonn, *Rev. Mod. Phys.* **83**, 543 (2011).
- [13] J. Lloyd-Hughes, and T. I. Jeon, *J Infrared Milli Terahz Waves* **33**, 871 (2012).
- [14] H. Nemecek, P. Kužel, and V. Sundstrom, *J. Photochem. Photobiol., A* **215**, 123 (2010).
- [15] J. G. Han, B. K. Woo, W. Chen, M. Sang, X. C. Lu, and W. L. Zhang, *J. Phys. Chem. C* **112**, 17512 (2008).
- [16] S. Kumar, N. Kamaraju, B. Karthikeyan, M. Tondusson, E. Freysz, and A. K. Sood, *J. Phys. Chem. C* **114**, 12446 (2010).
- [17] J. G. Han, W. Zhang, W. Chen, S. Ray, J. Zhang, M. X. He, A. K. Azad, and Z. Y. Zhu, *J. Phys. Chem. C* **111**, 13000 (2007).
- [18] H. Nishimura, N. Minami, and R. Shimano, *Appl. Phys. Lett.* **91**, 011108 (2007).
- [19] K. R. Mavani, M. Nagai, D. S. Rana, H. Yada, I. Kawayama, M. Tonouchi, and K. Tanaka, *Appl. Phys. Lett.* **93**, 231908 (2008).
- [20] C. Kadlec, V. Skoromets, F. Kadlec, H. Nemecek, J. Hlinka, J. Schubert, G. Panaitov, and P. Kužel, *Phys. Rev. B* **80**, 174116 (2009).
- [21] M. C. Beard, G. M. Turner, and C. A. Schmuttenmaer, *J. Phys. Chem. B* **106**, 7146 (2002).
- [22] P. Parkinson, H. J. Joyce, Q. Gao, H. H. Tan, X. Zhang, J. Zou, C. Jagadish, L. M. Herz, and M. B. Johnston, *Nano Lett.* **9**, 3349 (2009).
- [23] R. Ulbricht, R. Kurstjens, and M. Bonn, *Nano Lett.* **12**, 3821 (2012).
- [24] C. S. Yang, C. H. Chang, M. H. Lin, P. C. Yu, O. Wada, and C. L. Pan, *Opt. Express* **20**, A441 (2012).
- [25] D. V. Seletskiy, M. P. Hasselbeck, J. G. Cederberg, A. Katzenmeyer, M. E. Toimil-Molares, F. Leonard, A. A. Talin, and M. Sheik-Bahae, *Phys. Rev. B* **84**, 115421 (2011).
- [26] H. J. Joyce, Q. Gao, H. H. Tan, C. Jagadish, Y. Kim, J. Zou, L. M. Smith, H. E.

- Jackson, J. M. Yarrison-Rice, P. Parkinson, and M. B. Johnston, *Prog. Quantum Electron.* **35**, 23 (2011).
- [27] C. S. Jung, H. S. Kim, G. B. Jung, K. J. Gong, Y. J. Cho, S. Y. Jang, C. H. Kim, C. W. Lee, and J. Park, *J. Phys. Chem. C* **115**, 7843 (2011).
- [28] P. Parkinson, J. Lloyd-Hughes, Q. Gao, H. H. Tan, C. Jagadish, M. B. Johnston, and L. M. Herz, *Nano Lett.* **7**, 2162 (2007).
- [29] C. W. Cheng, B. Liu, H. Y. Yang, W. W. Zhou, L. Sun, R. Chen, S. F. Yu, J. X. Zhang, H. Gong, H. D. Sun, and H. J. Fan, *ACS Nano* **3**, 3069 (2009).
- [30] C. Kadlec, F. Kadlec, H. Němec, P. Kužel, J. Schubert, and G. Panaitov, *J. Phys. Condens. Matter* **21**, 115902 (2009).
- [31] C. Kang, I. H. Maeng, S. J. Oh, S. C. Lim, K. H. An, Y. H. Lee, and J.-H. Son, *Phys. Rev. B* **75**, 085410 (2007).
- [32] J. G. Han, Z. Y. Zhu, S. Ray, A. K. Azad, W. L. Zhang, M. X. He, S. H. Li, and Y. P. Zhao, *Appl. Phys. Lett.* **89**, 031107 (2006).
- [33] M. Batzill, and U. Diebold, *Prog. Surf. Sci.* **79**, 47 (2005).
- [34] X. Zou, M. He, D. Springer, D. Lee, S. K. Nair, S. A. Cheong, T. Wu, C. Panagopoulos, D. Talbayev, and E. E. M. Chia, *AIP Advances* **2**, 012120 (2012).
- [35] N. V. Smith, *Phys. Rev. B* **64**, 155106 (2001).
- [36] G. Sanon, R. Rup, and A. Mansingh, *Phys. Rev. B* **44**, 5672 (1991).
- [37] G. M. Turner, M. C. Beard, and C. A. Schmittenmaer, *J. Phys. Chem. B* **106**, 11716 (2002).
- [38] T. I. Jeon, K. J. Kim, C. Kang, I. H. Maeng, J. H. Son, K. H. An, J. Y. Lee, and Y. H. Lee, *J. Appl. Phys.* **95**, 5736 (2004).
- [39] H. Němec, P. Kužel, and V. Sundström, *Phys. Rev. B* **79**, 115309 (2009).
- [40] D. Tsokkou, A. Othonos, and M. Zervos, *Appl. Phys. Lett.* **100**, 133101 (2012).
- [41] J. Lloyd-Hughes, *Appl. Phys. Lett.* **100**, 122103 (2012).
- [42] H. K. Nienhuys, and V. Sundstrom, *Appl. Phys. Lett.* **87**, 012101 (2005).
- [43] Y. J. Lin, C. T. Lee, and H. C. Chang, *Semicond. Sci. Technol.* **21**, 1167 (2006).
- [44] S. C. Chang, *J. Vac. Sci. Technol.* **17**, 366 (1980).
- [45] Z. M. Jarzebski, and J. P. Marton, *J. Electrochem. Soc.* **123**, 299C (1976).
- [46] P. Tiwana, P. Docampo, M. B. Johnston, H. J. Snaith, and L. M. Herz, *ACS Nano* **5**, 5158 (2011).

Chapter 7. Conclusions and future work

In conclusion, we investigated the carrier dynamics in two-dimensional graphene and one-dimensional SnO₂ nanowires by means of ultrafast pump-probe technique and THz-TDS. Also, bulk material z-cut quartz and LAO substrate are characterized by THz-TDS, and the complex refractive index is obtained. These two materials are commonly used substrates for nanomaterials, thin films and functional materials, and so the accurate determination of their complex refractive index is essential for the THz study for the materials grown on these substrates.

7.1 Z-cut quartz and LAO single crystal: THz-TDS

Z-cut quartz and LAO are commonly-used substrates for growing nanomaterials, thin films and functional materials. It is very important to obtain accurate complex refractive indices of these substrates, since sample parameters greatly depend on the substrate complex refractive index. We want to know whether the substrate's complex refractive index is temperature and/or frequency dependent, and whether the annealing treatment will affect its dielectric properties. We have measured z-cut quartz and LAO single crystal with vacuum as reference, and obtained accurate values of their complex refractive index.

Z-cut quartz (CrysTec GmbH) is a very good transparent substrate for THz wave, as it has a temperature-independent and almost frequency-independent refractive index of $n = 2.10 + 0.002i$.

The refractive index $n(\omega)$ of LAO (CrysTec GmbH) is temperature-dependent and

increases monotonically with frequency. The values of $k(\omega)$ are very small, and no obvious absorption peaks appeared in the frequency range 0.2 — 3 THz. After the LAO is annealed, $n(\omega)$ shows sudden changes at certain frequencies where absorption peaks appear in $k(\omega)$. Also, the crystal orientation can affect the complex refractive index. Hence we suggest that, for optical measurements of thin films grown on LAO substrate (eg. THz-TDS), the reference substrate should undergo the same annealing conditions as the sample growing process. The orientation, temperature and frequency dependences of the complex refractive index should be taken into account when extracting the sample's optical parameters.

7.2 BLG and FeCl₃-G: Optical pump-probe technique

The photoexcited carriers in BLG exhibit two relaxation processes, the fast relaxation time less than 200 ps is attribute to coupling between hot electrons and optical phonons. Optical phonon emission is the most effective way of hot electron relaxation. The following relaxation is a few ps which is assigned to the decay of optical phonons. This slow relaxation time levels off at high pump power and serves as a bottleneck for the hot electrons relaxation. After the FeCl₃ intercalated in the BLG, the sample becomes hole-doped, the Dirac point is now located at ~1 eV. Also, there are many horizontal bands in the electronic band structure calculated by DFT (density functional theory). These additional bands originate from the d orbitals of iron. The presence of these additional bands cause three effects in our pump-probe results:

1. These additional electronic states facilitate photoexcited electron transition between lower and higher energy levels with the assistance of optical phonons. Optical phonons

can be emitted and *reabsorbed* by the carriers in the higher energy states, thus slowing down the energy relaxation of the photoexcited electrons.

2. Optical phonon emission and reabsorption causes the number of photoexcited electrons to be built up slowly, resulting in a longer rise time, and causes the disappearance of the initial fast relaxation process observed in BLG.
3. The signal $\Delta R/R$ changes sign, from negative (BLG) to positive ($\text{FeCl}_3\text{-G}$). Opposite signs of the signals from the two samples is due to state-filling effects (in BLG) and induced probe absorption (in $\text{FeCl}_3\text{-G}$) dominating the absorption of the probe pulse.

7.3 Twisted BLG: THz-TDS study

The conductivity spectrum of Bernal BLG depends on the impurity concentration, chemical potential, temperature and bias voltage, but is nonetheless almost Drude-like at the lowest frequencies. In twisted BLG, van-Hove singularities develop near the Fermi energy, which results in an enhanced density of states (DOS). Strongly coupled stacking order BLG is investigated by THz-TDS at different temperatures. The complex refractive index is obtained without the using the Kramers-Kronig relations, both n and k are found to decrease with increasing frequency. In the frequency dependence of the real conductivity, superposed on top of a Drude-like response, we observed a strong peak centered at ~ 2.7 THz. The overall Drude shape was analyzed using a disorder dependent model, while conductivity peak at 2.7 THz was attributed to an enhanced DOS at that energy, that is caused by the presence of low energy van-Hove singularities arising from a commensurate twisting of the top graphene layer relative to the bottom layer.

7.4 SnO₂ nanowires: THz-TDS

SnO₂ nanowires, as a wide band gap one-dimensional semiconductor, have triggered great interest due to their potential application in optics and electronics. However, the property in THz range is still absence, especially evolve with temperature. In chapter 6, the SnO₂ nanowires are investigated by THz-TDS as a function of temperature. Our results show that SnO₂ nanowires are not only transparent in visible range, but also in terahertz range 0.5 THz to 2.4 THz. Simple effective medium approximation is used to obtain the dielectric function of SnO₂ nanowires, and parameters are extracted by using Drude-Smith model to fit the complex conductivity. The carrier density increases and scattering time decreases with increasing temperature. The reduction in carrier mobility compared with bulk material indicates the presence of carrier backscattering and localization in the nanowires.

7.5 Future work

Elements that can effectively control and manipulate THz electromagnetic waves are highly desired to develop future sophisticated THz systems. Graphene is a promising material for the fabrication of the THz modulator, since the optical absorption comprises two components — One originates from the carrier intraband transitions and dominates in the THz range, while the other comes from interband transitions in the infrared and visible range (as long as photon energy greater than twice the Fermi energy of graphene: $h\nu > 2E_F$). In the THz range, the optical conductivity of graphene behaves like a conductive thin film material follow the Drude model $\tilde{\sigma}(\omega) = \tilde{\sigma}_{DC}(E_F) / (1 + \omega^2 \tau^2)$. $\tilde{\sigma}_{DC}(E_F)$ is the DC electrical conductivity which is strongly dependent on the Femi level.

It is well known that the graphene Fermi level can be turned by an external electric field [1, 2]. Hence, by applying an electric field, we can achieve an increased or decreased graphene conductivity and THz transmission. According to some theoretical calculations, the THz transmission for single-layer graphene can be achieved between ~ 0 and ~ 1 by tuning the graphene Fermi level [3, 4]. When the Fermi level is located to be exactly at the Dirac point, where the carrier density of states is a minimum, the THz transmission is maximum. However, in actual electric gating experiments, the efficiency of the transmission modulation is very low (less than 10%). There are two possible ways to improve the modulation efficiency:

1). **Graphene doping.** CVD-grown graphene usually shows hole doping effect, where the Fermi level is below the Dirac point. This *p*-doped effect causes the graphene Fermi level to be not sensitive to the gating voltage. Doping graphene with some nanoparticles or other dopants can make the Fermi level to be located approximately at the Dirac point, and thus enhances the tunable range of the Fermi level, and consequently, the efficiency of the device modulation.

2). **Graphene on metamaterial.** Split-ring resonator (SRR) based planar THz metamaterials possess the ability to sense a thin dielectric layer. This sensing capability is based on changes in the capacitance of the SRRs. When a thin film is added on a SRR, it will change the capacitance of the SRR and shift the resonant frequency. This shift of the resonant frequency can be utilized in a graphene THz modulator device. Since, in the THz range, the graphene conductivity is strongly dependent on the Fermi level, and can then be tuned by an external electric field, the dielectric constant can then be varied continually, thus effectively controlling the capacitance of the SRRs. The shift of the

resonant frequency of the SRRs can be used to realize the function of the THz modulator.

References

- [1] K. S. Novoselov, A. K. Geim, S. V. Morozov, D. Jiang, Y. Zhang, S. V. Dubonos, I. V. Grigorieva, and A. A. Firsov, *Science* **306**, 666 (2004).
- [2] J. B. Oostinga, H. B. Heersche, X. L. Liu, A. F. Morpurgo, and L. M. K. Vandersypen, *Nat. Mater.* **7**, 151 (2008).
- [3] B. Sensale-Rodriguez, T. Fang, R. S. Yan, M. M. Kelly, D. Jena, L. Liu, and H. L. Xing, *Appl. Phys. Lett.* **99**, 113104 (2011).
- [4] B. Sensale-Rodriguez, R. Yan, M. M. Kelly, T. Fang, K. Tahy, W. S. Hwang, D. Jena, L. Liu, and H. G. Xing, *Nat. Commun.* **3**, 780 (2012).